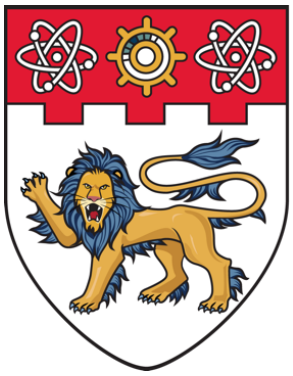

NANYANG TECHNOLOGICAL UNIVERSITY
SINGAPORE

Spin-Torque Ferromagnetic Resonance Investigation for Enhancement of Spin-Orbit Torque Efficiency

WONG DAO HWEE GRAYSON

SCHOOL OF PHYSICAL AND MATHEMATICAL SCIENCES

2021

Spin-Torque Ferromagnetic Resonance Investigation for Enhancement of Spin-Orbit Torque Efficiency

WONG DAO HWEE GRAYSON

SCHOOL OF PHYSICAL AND MATHEMATICAL SCIENCES

A thesis submitted to the Nanyang Technological University in partial fulfilment of the requirement for the degree of Doctor of Philosophy

2021

Statement of Originality

I hereby certify that the work embodied in this thesis is the result of original research done by me except where otherwise stated in this thesis. The thesis work has not been submitted for a degree or professional qualification to any other university or institution. I declare that this thesis is written by myself and is free of plagiarism and of sufficient grammatical clarity to be examined. I confirm that the investigations were conducted in accord with the ethics policies and integrity standards of Nanyang Technological University and that the research data are presented honestly and without prejudice.

5 Aug 2021

Date

Wong Dao Hwee Grayson

Supervisor Declaration Statement

I have reviewed the content and presentation style of this thesis and declare it of sufficient grammatical clarity to be examined. To the best of my knowledge, the thesis is free of plagiarism and the research and writing are those of the candidate's except as acknowledged in the Author Attribution Statement. I confirm that the investigations were conducted in accord with the ethics policies and integrity standards of Nanyang Technological University and that the research data are presented honestly and without prejudice.

5 Aug 2021
. . . . . .
Date

. . . . . .
Lew Wen Siang

Authorship Attribution Statement

This thesis contains material from 2 papers published and 1 paper under review in the following peer-reviewed journal(s) in which I am listed as an author.

Chapter 4 is published as G.D.H. Wong, W.C. Law, F.N. Tan, W.L. Gan, C.C.I. Ang, Z. Xu, C.S. Seet and W.S. Lew, "Thermal Behavior of Spin-Current Generation in Pt_xCu_{1-x} Devices Characterized through Spin-Torque Ferromagnetic Resonance", *Scientific Reports*. **2020**, 10, 1-8. DOI: 10.1038/s41598-020-66762-8.

The contributions of the co-authors are as follows:

- G.D.H. Wong conceived the idea, designed the work, and drafted the manuscript.
- W.C. Law, F.N. Tan and W.L. Gan assisted in the development of the experimental setup.
- Z. Xu assisted with the EDX characterization of the thin films.
- W.C. Law, C.C.I. Ang and Z. Xu made scientific comments on the result.
- W.S. Lew and C.S. Seet coordinated and supervised the entire work.
- All authors contributed to the discussion and manuscript writing.

Chapter 5 is published as G.D.H. Wong, Z. Xu, W.L. Gan, C.C.I. Ang, W.C. Law, J. Tang, W. Zhang, P.K.J. Wong, X. Yu, F. Xu, A.T.S. Wee, C.S. Seet, and W.S. Lew. "*Strain-Mediated Spin–Orbit Torque Enhancement in Pt/Co on Flexible Substrate*", ACS Nano. **2021,** 15, 8319-8327. DOI: 10.1021/acsnano.0c09404

The contributions of the co-authors are as follows:

- G.D.H. Wong conceived the idea, designed the work, and drafted the manuscript.
- G.D.H. Wong and Z. Xu fabricated the devices and collected the data.
- W.C. Law and W.L. Gan assisted in the development of the experimental setup.
- W.L. Gan, C.C.I. Ang, and Z. Xu made scientific comments on the results.
- J. Tang and X. Yu performed the XRD and XAS measurements.
- W. Zhang and P.K.J. Wong analyzed the XAS/XMCD data.
- W.S. Lew, C.S. Seet, A.T.S. Wee, and F. Xu coordinated and supervised the entire work.
- All authors contributed to the discussions and the revision of the final manuscript.

Chapter 6 is published as G.D.H. Wong, C.C.I. Ang, W.L. Gan, W.C. Law, Z. Xu, X. Yu, F. Xu, C.S. Seet, and W.S. Lew. "*Reversible Strain-Induced Spin-Orbit Torque on Flexible Substrate*", *Applied Physics Letters*, **2021**, 119, 042402. DOI: 10.1063/5.0056995

The contributions of the co-authors are as follows:

- G.D.H. Wong conceived the idea, designed the work, and drafted the manuscript.
- G.D.H. Wong and Z. Xu fabricated the devices and collected the data.
- W.C. Law and W.L. Gan assisted in the development of the experimental setup.
- W.L. Gan, C.C.I. Ang, and Z. Xu made scientific comments on the results.
- Z. Xu performed the XRD and XAS measurements.
- W.S. Lew, C.S. Seet, and F. Xu coordinated and supervised the entire work.
- All authors contributed to the discussions and the revision of the final manuscript.

5 Aug 2021
. . . . . .
Date

. . . . . .
Wong Dao Hwee Grayson

Abstract

Current-induced magnetization switching by spin-orbit torque generated through heavy metals offers an enticing realm for energy-efficient memory and logic devices. The spin Hall effect, namely the charge to spin current conversion *via* the spin-orbit coupling is the phenomenon that facilitates these spin-orbit torques (SOT) devices and the figure of merit to quantify the conversion efficiency is known as the spin Hall efficiency. Since the first demonstration of the spin Hall effect, many research revolves about understanding and enhancing its efficiency. However, even with the accumulated development over the past decades, the techniques to enhance the spin current generation are limited while the manipulation of current-induced spin-orbit torques remains elusive and challenging.

Thermal behavioral studies of the spin Hall effect have often been overlooked despite their profound significance in a real-world application. In this thesis, the temperature dependence of spin Hall efficiency and Gilbert damping of Pt_xCu_{1-x} are investigated to study the thermal robustness of the alloy at elevated temperatures. By tunning the alloy composition, the spin Hall efficiency could be manipulated, and it was found that the spin Hall efficiency of Pt_xCu_{1-x} alloys with greater Pt content is temperature insensitive. The spin pumping contribution to the Gilbert damping can also be controlled by adjusting the alloy composition. As such, the alloy becomes thermal stable when the intrinsic and spin pumping damping contribution counteracts one another. The critical switching current density was also calculated. At the optimal alloy composition of x=47%, the spin transparency of the alloy is at its highest. Therefore, alloying not only enhances the spin Hall efficiency but also improves the thermal robustness for device operation at elevated temperatures.

For the development of flexible energy-efficient SOT application, the spin Hall efficiency of bilayer Pt/Co under varying mechanical strain is extensively studied. As tensile strain is applied, strain-mediated SOT enhancement is observed and even after removing the applied strain, 78% of the enhancement is preserved. The strain-treated samples also have lower Gilbert damping as the spin pumping damping contribution decreases. These improvements in Pt/Co bilayer suggest that the switching current density can be reduced through strain application. With the aid of the X-ray magnetic circular dichroism and spin transparency measurement, the SOT enhancement is attributed to a bulk effect in the Pt layer with an increased extrinsic spin Hall effect. To further embellish the appeal of strain, a unique technique comprising of a combination of mechanical strain and mild annealing treatment is

adopted such that the strain-mediated SOT enhancement is reversible. The mild annealing can alleviate the residual strain from the strain treatment and is verified using X-ray diffraction. Besides SOT application, the strained Pt/Co bilayer can function as a microwave detector as the application of strain alters its resonance field. The tunable detector remains stable and robust even after 10^4 cycles of bending and unbending. These findings shed light on the origin and use of strain-mediated SOT enhancement and are promising in shaping future utilization of mechanical strain for energy-efficient devices.

Acknowledgements

This thesis is the fruit of my four-year journey and it could not have been achieved without the help and support of my many colleagues, supervisors, friends, and family members. My supervisor Prof. Lew Wen Siang and Dr. Seet Chim Seng have played an important role in guiding me throughout my Ph.D. journey. Prof. Lew has been an awesome supervisor who has provided me with not only support in my academic journey but also countless pieces of advice on career development and words of wisdom to shape my life. Under his guidance, I developed more confidence and the life skills needed to continue my career journey. Dr. Seet has been a caring supervisor that has always kept a lookout for my well-being and lent me a listening ear to my problems. I truly appreciate his support at work and the opportunity to be part of his team. Overall, it has been a wonderful four years which I truly never forget.

Wai Cheung, Funan, and Shawn are cheerful seniors that have supported me numerous times during the early stages of my Ph.D. journey. This trio has brought fun, joy, and laughter to the laboratory and made it a more enjoyable place. Calvin is an expert in Skyrmions and has also been a wonderful batchmate, who has been constantly pushing me to work harder in order to keep up. Xu Zhan is a pleasant visiting student that has heavily influenced my research direction. Through interacting with him, I have learned many valuable things and it has helped broaden my scope of research. Although Andhita's area of research is not in spintronics, he has aided me with his critical thinking and analytical skill providing me with a different perspective on my problems. Weiliang and Gerard are the pillars of the Spintronics laboratory. Weiliang, with his immense knowledge of magnetism and experience with setting up tools, has always been giving scientific inputs and brainstorming for new and exciting ideas to try. Being one of the most experienced people in the lab, Gerard is the go-to guy when faced with any issues. Together, there is no problem these two pillars of our lab cannot resolve. Matthew, my undergraduate batchmate whom I have traveled together with during my Uppsala University exchange, is my journey to the west buddy. It was pleasant to commute while bringing up nostalgic epic moments during our exchange and discussing random topics that helped lighten up our work problems. Having spent four years of my life in the Spintronics lab, it is my friends and colleagues who had made the environment an enjoyable one. Thank you, everyone!

Here, I would like to give special thanks to Wai Cheung and Weiliang. They are the biggest reason behind the establishment of the ST-FMR and without them, I could not have set it up. Despite their busy schedule, they have always given me a helping hand when I needed advice or assistance during the construction of the setup.

To my collaborators, Prof. Andrew Wee, Prof. Xu Feng, Prof. Wen Zhang, Prof. Johnny Wong, Jiaxuan, and members at NUS and NJUST. I would like to thank you for making my research experience a fruitful and fulfilling one. I am grateful for the time and effect taken to review and provide constructive feedback. I would also like to thank all my colleagues at GlobalFoundries Singapore whom I have worked with. They have assisted me through this journey and provided me with their continual support in times of need. I deeply appreciate the guidance and patience they have for me while I learn the ropes.

It has been an arduous journey and I would like to take this opportunity to thank my family members. My parents have been caring and understanding in their unique ways and it is with their support that I made it this far. I am truly grateful for their unconditional love and support.

Table of Contents

List of Tables

List of Figures

List of Acronyms

AC	Alternating Current
AHE	Anomalous Hall Effect
AFM	Anti-Ferromagnet
AMR	Anisotropic Magnetoresistance
CMOS	Complementary Metal-Oxide-Semiconductor
CIP	Current-in-Plane
CPP	Current Perpendicular to Plane
CPU	Central Processing Unit
DC	Direct Current
DOS	Density of States
DW	Domain Wall
DRAM	Dynamic Random Access Memory
EBL	Electron Beam Lithography
EDX	Energy-Dispersive X-Ray Spectroscopy
FL	Free Layer
FM	Ferromagnet
FMR	Ferromagnetic Resonance
GF	Gauge Factor
GMR	Giant Magnetoresistance
HDD	Hard Disk Drive
HM	Heavy Metal
IBE	Ion Beam Etching
IL	Insulator Layer
IMA	In-Plane Magnetic Anisotropy

LLG	Landau-Lifshitz-Gilbert
MRAM	Magnetoresistive Random Access Memory
MTJ	Magnetic Tunnel Junction
NM	Non-Magnetic/Normal Metal
PHE	Planar Hall Effect
PMA	Perpendicular Magnetic Anisotropy
PMMA	Poly(Methyl Methacrylate)
pMTJ	Perpendicular Magnetic Anisotropy MTJ
PVD	Physical Vapour Deposition
RAM	Random Access Memory
RE	Rare Earth
RF	Radio Frequency
SHE	Spin Hall Effect
SMR	Spin Hall Magnetoresistance
SOC	Spin-Orbit Coupling
SOT	Spin-Orbit Torque
SRAM	Static Random Access Memory
SSD	Solid State Drive
ST-FMR	Spin-Torque Ferromagnetic Resonance
STT	Spin-Transfer Torque
TMR	Tunnelling Magnetoresistance
UV	Ultraviolet
UVL	Ultraviolet Lithography
VSM	Vibrating Sample Magnetometer
XAS	X-Ray Absorption Spectra

XRD	X-Ray Diffraction
XMCD	X-Ray Magnetic Circular Dichroism
XRR	X-Ray Reflectometry

Chapter 1 Introduction

The use of modern electronics has become an irreplaceable component for most of our daily lives in the 21st century and our reliance on them will only continue to grow with more advancement in technology. One of the driving forces behind these electronics is the ever-improving memory system that they operate on. Greater memory density, lower latency, and lower cost per bit are a few of the qualities the industry has been seeking out for and that led to the development of the current memory storage hierarchy as shown in Figure 1-1. This memory storage hierarchy is a comparison of the different memory technologies used today and their implemented roles. At the peak of the pyramid, the CPU registers and cache represent the fastest memory. Located closest to the processing core, they typically occupy between 512 bytes to a few kilobytes (kB) of memory and their high speed is mainly achieved through the support of high-speed random-access memory (RAM). There are two main variants of the RAM, and they are the dynamic random-access memory (DRAM) and the static random-access memory (SRAM). With the aid of their multi- and demultiplexing circuitry, they are able to operate at high speed and are usually used to store a large amount of data for a short period of time. One of the greatest drawbacks of the volatile memory is the constant need for power in order to store the binary data them as the electric charge in capacitors slowly leak over time.

On the other hand, non-volatile memory on the lower portion of the pyramid has high-capacity storage and does not require constant power for storage. SSD utilizes solid-state memory in the form of NAND Flash providing for high storage capacity and non-mechanical operation along with much higher speed compared to their counterpart, the HDD. Cost efficiency is one of the key advantages that give the HDD an edge over the SSD. Although the hierarchy system has been adequate in providing memory solutions for the many different computational operations, advancement in memory technology will bring about new obstacles.[1,2] Electrical current leakage and high-power consumption are a few of the issues that chip makers will face as our electronics scale smaller. Data computing-intensive task, such as cryptography, physical simulation, and weather forecasting, has driven the need for more powerful computational performance. Modern computer architecture has changed and adapted by introducing more cores to processors, having multi-threading and other technologies to reduce the latency and increase the throughput. This growing demand for energy efficiency yet small and powerful computational performance has resulted in the need for more transistors on

every electronic chip and the packing density of transistors has since doubled almost every two years. This rapid growth trend was described by Gordon Moore and is commonly referred to as Moore's law.[3] Despite the ever-growing demand for powerful computational performance, the predicted trend by Moore's law began to deviate. The International Technology Roadmap for Semiconductors (ITRS) in 2014 declared for a reorganization and in its subsequent meet at the International Roadmap for Devices and Systems (IRDS), potential emerging technology to tackle the declining trend of Moore's law in the semiconductor industry was addressed. The IRDS coordinated experts from many various fields and backgrounds to come together and overcome the potential challenges foresighted by the semiconductor industry. These experts included highly experienced engineers from the industries, research bodies, academia, and even equipment suppliers. Among the many candidates under the category of "Beyond CMOS", spintronics devices shine as a promising technology that can resolve the scalability problem that the CMOS is facing.[4]

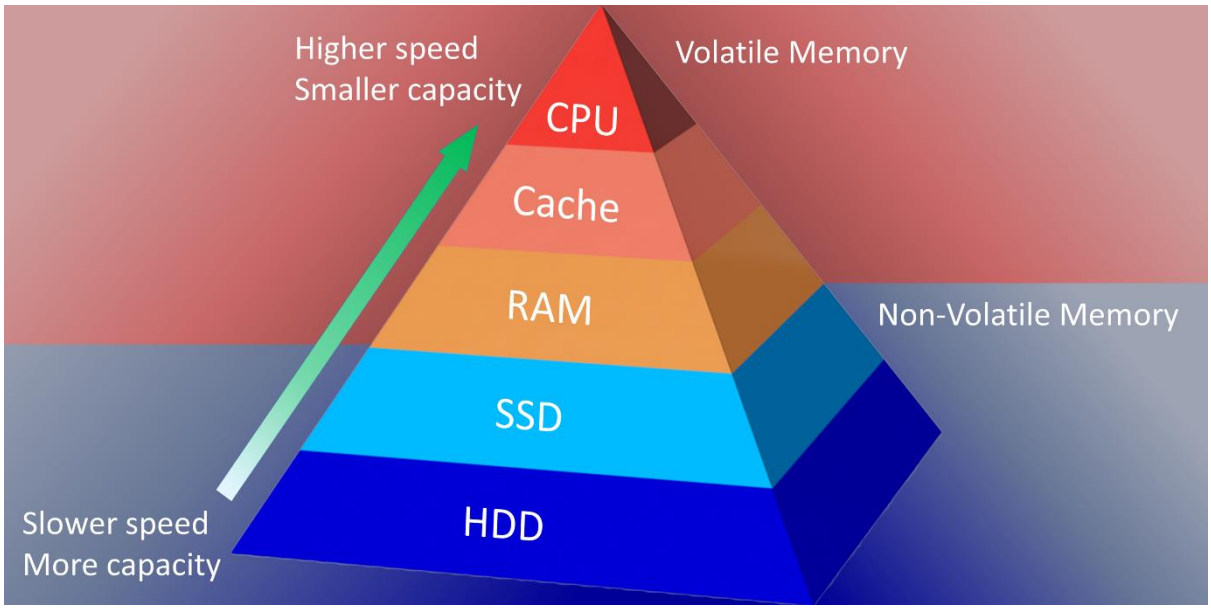

Figure 1-1 Memory-storage hierarchy showing the different memory tiers based on their read and write speed, capacity, and complexity.

Table 1 shows a comparison of the performance parameter between conventional and emerging solid-state memories. In the table, being non-volatile, having a small cell size, short read and write time, low power consumption, and high endurance are some of the desirable characteristics of ideal memory technology.[5-8] The unit to measure the cell size is F^2 and it is currently defined by the technology node as the advancement of CMOS technology such as the

FinFET, the previously used definition of gate length as a measure of cell size has become invalid.

Data centers are the foundation of the world increasingly digitalized world. The demand for their services increasing ever so rapidly, new technology such as Internet of things (IOT), Artificial Intelligence (AI), distributed manufacturing systems, and autonomous vehicles promise to raise demand even further. Energy consumption of data centers take up an estimated total of 1% of the global electricity use.[114] With such significant energy impact, it is only critical that their consumptions are monitored carefully and energy efficient alterative are constantly pursued. Therefore, the demand for fast and energy efficient data storage alterative is constantly on the rise, which makes emerging memory technology very attractive.

Table 1-1 Memory specification compilation comparing conventional and emerging memory technologies. The blue and green highlighted boxes represent desirable performance by the conventional and emerging memory technologies respectively and the red boxes highlight areas that are still lacking performance.

Parameters	Conventional Memory Technology			Emerging Memory Technology	
	SRAM	DRAM	NAND Flash	STT-MRAM	SOT-MRAM
Volatility	No	No	Yes	Yes	Yes
Cell Size (F^2)	50 – 120	6 – 10	5	6 – 20	6 – 20
Read Time (ns)	≤ 2	30	10^3	1 – 20	≤ 10
Write Time (ns)	≤ 2	50	10^6	~ 10	≤ 10
Write Power	Low	Low	High	Low	Low
Endurance (Cycle)	> 10^{15}	> 10^{15}	10^5	> 10^{15}	> 10^{15}

1.1 Motivation

Spin transport electronics, or Spintronics, in short, is a field of research that capitalizes on the spin of the electron to control and manipulate magnetic moment. The intertwining of the electron spin and charge provides an additional degree to further improve the scalability of device application. There have been many devices such as the spin transistor,[9-11] spin logic devices,[12-15] spin-torque nano-oscillators,[16-20] racetrack memory,[21-25] and magnetoelectric memory[26-28] that have been proposed since the emergence of the field. Two key scientific

breakthroughs that helped realize these application devices were spurred out by the discovery of giant magnetoresistance (GMR)[29,30] and tunneling magnetoresistance (TMR).[31,32] Today, these two phenomena form the operation basis of most ultra-sensitive magnetic field sensors in the read-and-write head of magnetic hard disk drive (HDD).

Hard disk drives are great memory storage devices that have been serving our storage needs for many decades and with all the improvements and advances in HDD technology, hard disk drives will continue to stay relevant for many years to come due to their large storage capacity. That said, one main flaw to the drive is that its operation involves the use of the mechanical movement of the read-and-white head. This cripples the hard disk drive and causes significant delays in locating the individual storage address. To overcome this obstacle, researchers have proposed the use of magnetic tunnel junctions (MTJs) as storage cells. These

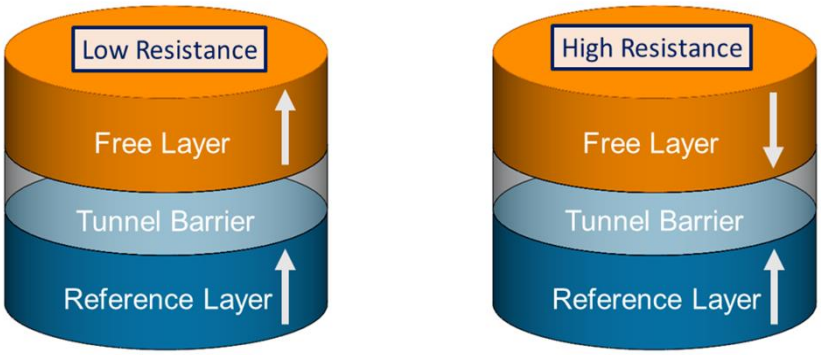

Figure 1-2 Illustration showing the parallel and antiparallel state of a magnetic tunnel junction. The magnetization orientation between the free and reference layer determines the resistance state of the junction.

MTJs are arranged in an array and are read using the random-access method. Due to the architecture of the device, this new type of non-volatile memory is known as magnetic random-access memory (MRAM). An MTJ is a junction that consists of two ferromagnet layers sandwiched by an insulating layer as shown in Figure 1-2. Each of the ferromagnet layers has a special name and serves a specific task in the heterostructure of the MTJ. The free layer is the switching layer which is able to change its magnetization orientation while the reference layer has a fixed magnetization. The insulating layer also known as the tunnel barrier allows for the tunneling of electrons between the two ferromagnet layers.

The MTJ has a parallel and antiparallel state depending on the orientation of the magnetization of the two ferromagnet layers. When the magnetization of the two ferromagnet layers are in the same direction, the MTJ is in its parallel state and when they are opposite with

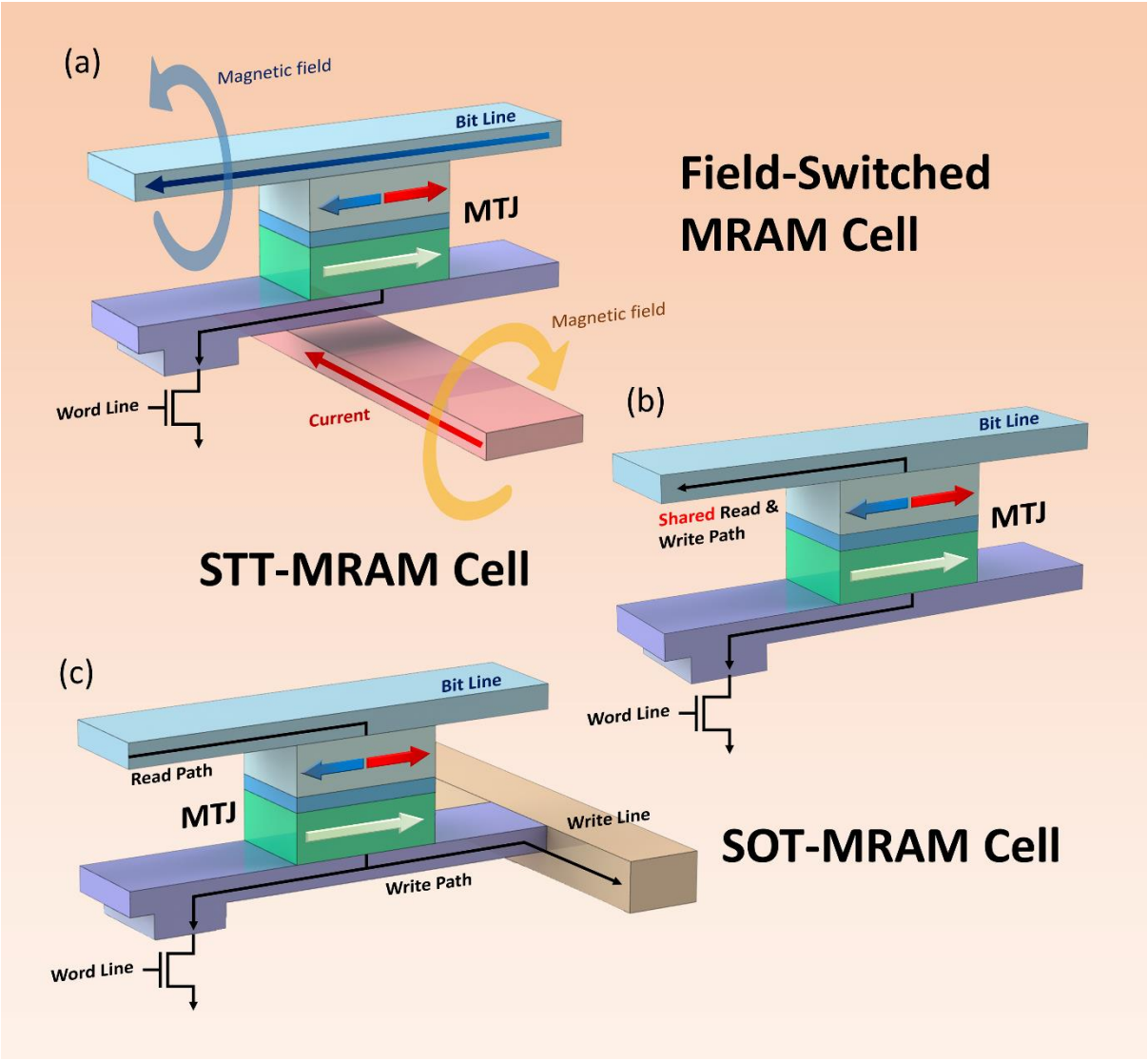

Figure 1-3 Types of MTJs. (a) Field-switched MTJ cell. (b) STT-MRAM cell. (c) SOT-MRAM cell. Resistance states of the MTJ cells are probed by the read line and switched using the write line. The red and blue arrow indicate the possible direction of the free layer magnetization. It could either be in the parallel or anti-parallel state with respect to the reference layer.

one another, it is in an antiparallel state. While in the parallel state, electrons can tunnel through the tunnel barrier due to the similar quantum state on both sides of the barrier resulting in lower resistance. In order to keep fix the magnetization orientation of the reference layer, an exchange bias with an adjacent antiferromagnetic layer is used. This allows the free layer to switch freely to achieve the parallel and antiparallel state to store binary data as "1" and "0" respectively.[33]

Throughout the development of the MRAM technology, the reading mechanism employed has remained relatively the same even though there has been extensive research in the field while the writing mechanism has been constantly changing and evolving. The pioneer

generation of MRAM devices capitalized on the local magnetic field generated by passing a current through orthogonal write lines to switch the magnetization orientation of specific MTJ cells as shown in Figure 1-3(a).[34] Despite the simplicity of the technique, it soon stumbled upon various issues. Scalability was one of its limitations as it required sufficient space between cells to avoid stray fields from write lines from accidentally switching the unwanted cell. Furthermore, the demagnetization field increases with smaller junctions resulting in a larger localized magnetic field required for switching. This snowballs and creates a thermal issue for the device as higher current density through write lines is needed in order to generate the larger magnetic field.

Subsequently, thermally-assisted switching MRAM (TAS-MRAM) was introduced as the coercivity of the MTJ free layer can be reduced by the generation of localized joule heating to assist with magnetization switching.[35,36] However, this technique also faced scalability issues as the localized heat generated becomes difficult to control with decreasing cell size and this led to the development of the next generation of MRAM known as the spin-transfer torque MRAM (STT-MRAM). This switching technique utilizes the spin-polarized current to manipulate the magnetization of the free layer through the spin-transfer torque (STT) effect. To do so, these spins are injected by either injecting charge current directly to the free layer or through the reflected charge current from the fixed layer. More details regarding the working principles will be discussed in Chapter 2.4. On-going research to commercialize the STT-MRAM by companies such as Everspin Technologies, Grandees, Avalanche technology, and Spin Transfer Technologies have helped speed up and mature the technology. In August 2016, Everspin began shipping their first STT-RAM chips with 256 Mb memory.

Despite the many advantages of the STT switching technique, some of the drawbacks include the requirement of an extra FM layer to create a spin-polarized current for STT and the need for the charge current to pass through the MTJ during application which will breakdown the tunnel barrier over time.[37,38] To tackle the breakdown issue, a different approach to generating the spin current was proposed. These memories are known as spin-orbit torque-driven MRAM (SOT-MRAM) and they preserve the lifespan of the tunnel barrier by separating the read and write current paths by including additional transistors as shown in Figure 1-3(c).[39-45] The spin current used for switching the free layer is generated by exploiting the spin Hall effect (SHE) when a charge current passes through a material of strong spin-orbit coupling (SOC). A commonly used figure of merit to examining the charge-to-spin current conversion

is described by the spin Hall angle. In recent years, there have been many experiments revolving around understanding its origin and more importantly, development to improve the spin Hall angle. A wide variety of quantification techniques have been developed in the last decades which include spin pumping, nonlocal spin-value (NLSV) and harmonic Hall measurement techniques. Among the many techniques, the spin-torque ferromagnetic resonance (ST-FMR) technique will be the main focus of this thesis. Since its first SOT quantification experiment by *Liu* in 2011, the ST-FMR has grown in popularity due to its ease of use and self-calibrating mechanism.[39,46,47] Furthermore, besides SOT measurements, the ST-FMR is also capable of characterizing other parameters such as Gilbert damping and spin mixing conductance.

In the first demonstration of ST-FMR, *Liu* evaluated Pt (6 nm)/Py (4 nm) bilayer structure microstrip at room temperature.[46] He evaluated the SOT efficiency of Pt using both the line-shape method and the modulation of damping method, which will be discussed in detail in Chapter 3.8, and determined it to be ~0.056. Capitalizing on the large SOT efficiency of Pt, *Liu* went on to demonstrate SOT-driven magnetization switching in Pt/Co/Al_2O_3 trilayer structures.[48] During this period, the SOT efficiency of Pt has been quantified using several other measurement techniques by different research groups and the result showed a large variation in the SOT efficiency of Pt ranging from ~0.012 to ~0.12.[49-57] This difference in SOT efficiency was puzzling and a reason to explain the discrepancy needed. For ST-FMR measurements, the calculated SOT efficiency can be broken down into three different sections. The first two sections for consideration are the spin diffusion length of the FM and HM layer, which are characteristics often overlooked. The effects of spin diffusion lengths were studied and demonstrated by *Wang* where he performed thickness dependence for Pt/Py bilayers measured using ST-FMR.[49] In his work, they discovered that the SOT efficiency increases with Py thickness and by considering the spin diffusion length, he determined the SOT efficiency to be ~0.068 and the spin diffusion length of Pt to be 1.5 nm. Lastly, the interfacial transparency between the FM and the HM, also known as spin transparency, is the spin current transmission coefficient between the layer interfaces.

Spin loss at the interface between the FM and HM interface occurs and it is important to characterize the spin transparency of the interface in order to better estimate the SOT efficiency of a material.[58,59] *Zhang* extensively explored the spin transparency of Pt/Py and Pt/Co using ST-FMR.[60] From his findings, Pt/Co bilayer had a much larger SOT efficiency of ~0.11 than

Pt/Py bilayer, which was measured at ~0.05. He attributed the difference in magnitude to the difference in spin transparency between the FM and HM, which was related to the effective spin mixing conductance at the interface. This was coherent with his findings as the measured effective spin mixing conductance of Pt/Co bilayer was more than double of Pt/Py bilayer and his calculated spin transparency for Pt/Co and Pt/Py bilayer were ~0.65 and ~0.25, respectively. Taking the spin transparency into account, the intrinsic SOT efficiency of Pt/Co and Pt/Py are ~0.17 and ~0.20 respectively. This result suggests that the Pt/Co interface allows for spin current to transmit more easily as compared to Pt/Py due to better electronic band matching in Pt and Co. To avoid confusion in the thesis, the spin Hall angle (or intrinsic SOT efficiency) of a material is independent of the interface between the FM and HM. Typically the measured spin Hall efficiency (or SOT efficiency) is smaller than the spin Hall angle as it takes into account the spin transparency.

Another spin transparency study conducted by Pai on Pt/Co and Pt/CoFe bilayers found that SOT efficiency can be tuned using different FM/HM interface conditions.[61] By doing so, he was able to yield a large SOT efficiency of ~0.3 using Pt, which was a much larger value compared to the measured value of ~0.06. This implies that the spin Hall efficiency is greatly affected by the spin memory loss at the interface. Therefore, the measured value using ST-FMR is typically smaller than the intrinsic spin Hall efficiency due to the spin transparency of the FM/HM interface. Since the demonstration of the importance of spin transparency, there have been many works trying to engineer the interface transparency such as by inserting a spacer layer between the HM and FM,[62-66] having a dusting layer at the interface[67-70] and manipulating the crystal structures of the thin film.[71]

Apart from Pt, many other promising spin Hall generator materials were explored. Ta and W are two materials that exhibit large spin Hall efficiency in their beta phase. Shortly after quantifying the spin Hall efficiency of Pt, *Liu* reported a giant spin Hall effect in Ta using Ta/CoFeB bilayer at room temperature.[39] Furthermore, in the same work, he demonstrated an efficient SOT-driven magnetization switching in a three-terminal MTJ device. The MTJ used was an in-plane magnetization MTJ with a stack structure of Ta/CoFeB/MgO/CoFeB. With his demonstration, SOT-based devices began gaining attention as a potential candidate for power-efficient and high-speed memory and logic devices. Here, the spin Hall efficiency of Ta reported was ~0.15 using the line-shape method and it has a negative sign, unlike Pt. This implied that the spin accumulation direction of Ta is opposite that of Pt and by engineering the

structure of the device, a much larger spin Hall efficiency can be achieved if the spin accumulation direction of both HM layers is the same. This method of engineering the stack structure was demonstrated using both harmonic[72] and ST-FMR[73,74] measurements. Similar to Pt, Ta also has varying spin Hall efficiencies ranging between 0.0037 and 0.26 measured using different techniques and thicknesses.[57,75-83] However, for Ta, the spin Hall efficiency and spin diffusion length relationship are not as clear as in the case of Pt due to the multi-phases of Ta which can exist in the α-, β-phases or amorphous state. This ambiguity is also seen in W as it has a multi-phases characteristic as well.

Among the pure HM, one of the largest spin Hall efficiency of ~0.3 was observed in W/CoFeB bilayer by Pai[47] using ST-FMR measurement at room temperature. This was much larger than the previously observed spin Hall efficiency in Ta and in his work, he demonstrated SOT-driven magnetization switching using a three-terminal MTJ using β-phase W as the spin current generation material. The critical switching current density required was determined in W/CoFeB/MgO was one order of magnitude smaller than its counterpart Pt. Despite the large spin Hall efficiency of β-phase W, its fabrication process remains challenging and unstable. This resulted in a large variation in the spin Hall efficiency of W reported ranging from 0.0043 to 0.95 by many different research groups using different techniques.[47,79-81,83-88]

Venturing beyond pure HM, a widely adopted technique to enhance the spin Hall efficiency is through alloying. To date, there have been many combinations of alloyed materials investigated, and some examples of such work include Pt_xCu_{1-x},[74,89-92] $Au_{1-x}Pt_x$,[93-95] $Cu_{1-x}W_x$,[96] AuW,[97-99] and Au_xTa_{1-x}[100]. One common trend among the many alloyed materials studied is the use of light conductive metals and HM with strong spin-orbit coupling as their alloy composition.[101-103] In a systematic study conducted by *Ramaswamy*[89], he demonstrated the ability to tune the spin Hall efficiency by tuning the alloy compositing, and with only 28% Pt, his $Pt_{28}Cu_{72}$/Py bilayer was able to perform similarly to a pure Pt/Py bilayer device. Apart from his spin Hall efficiency analysis, he also discovered that the skew scattering contribution was played an important role in lower Pt concentration alloys while side-jump scattering aided the enhancement of spin Hall efficiency at higher Pt concentration. The different contribution of the extrinsic scattering contribution was a result of different electrical resistivity of the alloy as Pt concentration changes. Skew scattering is independent of the increased resistivity due to alloying whereas the side jump-contribution scales with the change in resistivity.[104,105] *Ramaswamy*'s findings were coherent with earlier experimental and theoretical studies, and

this aided the understanding of how the extrinsic spin Hall effect can be manipulated by tuning the alloy composition.[106,107]

Over the years, there have been many innovative techniques to enhance the spin Hall efficiency of materials. Techniques such as having a dusting layer or insertion at the HM/FM interface, [62-70] multilayered HM/NM,[108] strain,[109-111] and ionic liquid gating[112,113] are just some examples from the tip of the iceberg as new techniques are constantly developed and researched. In this thesis, we will be discussing about some techniques to enhance and control the spin Hall efficiency, in particular alloying and strain, which brings us to the objective of this thesis.

1.2 Objective of the thesis

The main aim of this thesis is to enable the realization of high-performance SOT-drive memory and logic devices. As such, the objectives listed below are conceived with specific roles to improve and aid the development of the key performance parameters of the SOT-drive memory architecture such as spin Hall efficiency, spin transparency and thermal robustness, and the reduction in magnetic damping and switching current density. The objectives of this thesis are as follows:

i) Alloying has become an increasingly attractive method to further enhance the spin Hall efficiency of materials with strong spin-orbit coupling. Here, we explore the thermal behavior of Pt_xCu_{1-x} and demonstrate that alloying can not only improve the spin Hall efficiency of Pt_xCu_{1-x} but also enhance its thermal robustness and spin transparency of the HM/FM interface.

ii) The understanding behind the origin of the strain-induced spin-orbit torque enhancement remains unclear despite several works demonstrating it. To shed light on the origin of the enhancement, the spin transparency, and X-ray magnetic circular dichroism of Pt/Co bilayer were studied.

iii) Strain-induced spin-orbit torque enhancement is a promising candidate to achieve significantly larger spin Hall efficiency however its reversibility remains elusive. Here, we demonstrate that the enhancement can be reversibly tuned using a combination of mild annealing and mechanical strain.

1.3 Thesis structure

Chapter 2 delivers the background theory relevant to this thesis beginning with the magnetic dynamics in a system along with the different components experienced by the magnetization. After which, spin-orbit coupling is introduced to explain how spin current generation occurs through the phenomenon spin Hall effect. The intrinsic and extrinsic contribution of the spin Hall effect is also discussed. Next, details of the spin-transfer torque are examined to understand how STT-MRAM is switched. Different types of magnetoresistances are also presented.

Chapter 3 describes the experimental techniques used in this thesis. Details regarding the device fabrication which include thin film deposition to lithography are discussed. Brief descriptions of material characterization techniques employed are also introduced.

Subsequently, in Chapter 4, our finding presents the thermal behavior study of Pt_xCu_{1-x} as a spin current generator. Improvement in thermal robustness of the spin current generation is demonstrated. Furthermore, the spin transparency of the heterostructure was studied to account for the enhancement in spin Hall efficiency.

In Chapter 5, the strain-mediated spin-orbit torque enhancement is studied and from the findings, the enhancement remains even after the applied strain is removed. Spin transparency and X-ray absorption spectroscopy/X-ray magnetic circular dichroism (XAS/XMCD) measurements were performed to determine the source of the enhancement.

Next in Chapter 6, using a combination of mechanical strain and mild annealing, reversible strain-induced spin-orbit torque is demonstrated. Apart from controlling the spin current generation, the resonance field was also tunable and is robust even after 10^4 cycles.

Lastly, in Chapter 7, the works presented in this thesis are summarized and future works to pursue the enhancement and control of the spin current generation are proposed.

Reference

1 J. Åkerman. Toward a universal memory. *Science* **308**, 508-510 (2005).

2 H.-S.P. Wong & S. Salahuddin. Memory leads the way to better computing. *Nature Nanotechnology* **10**, 191-194 (2015).

3 G.E. Moore. Cramming more components onto integrated circuits, Reprinted from Electronics, volume 38, number 8, April 19, 1965, pp. 114 ff. *IEEE Solid-State Circuits Society Newsletter* **11**, 33-35 (2006).

4 D.E. Nikonov & I.A. Young. Overview of beyond-CMOS devices and a uniform methodology for their benchmarking. *Proceedings of the IEEE* **101**, 2498-2533 (2013).

5 R. Sbiaa, H. Meng & S. Piramanayagam. Materials with perpendicular magnetic anisotropy for magnetic random access memory. *Physica Status Solidi (RRL)–Rapid Research Letters* **5**, 413-419 (2011).

6 E. Chen, D. Apalkov, Z. Diao, A. Driskill-Smith, D. Druist, D. Lottis, V. Nikitin, X. Tang, S. Watts & S. Wang. Advances and future prospects of spin-transfer torque random access memory. *IEEE Transactions on Magnetics* **46**, 1873-1878 (2010).

7 J. Slaughter, R. Dave, M. DeHerrera, M. Durlam, B. Engel, J. Janesky, N. Rizzo & S. Tehrani. Fundamentals of MRAM technology. *Journal of Superconductivity* **15**, 19-25 (2002).

8 S. Bhatti, R. Sbiaa, A. Hirohata, H. Ohno, S. Fukami & S. Piramanayagam. Spintronics based random access memory: a review. *Materials Today* **20**, 530-548 (2017).

9 S. Datta & B. Das. Electronic analog of the electro-optic modulator. *Applied Physics Letters* **56**, 665-667 (1990).

10 S. Sugahara & J. Nitta. Spin-transistor electronics: An overview and outlook. *Proceedings of the IEEE* **98**, 2124-2154 (2010).

11 R. Vincent, S. Klyatskaya, M. Ruben, W. Wernsdorfer & F. Balestro. Electronic read-out of a single nuclear spin using a molecular spin transistor. *Nature* **488**, 357-360 (2012).

12 G.J. Lim, D. Chua, W.L. Gan, C. Murapaka & W.S. Lew. Programmable Spin–Orbit-Torque Logic Device with Integrated Bipolar Bias Field for Chirality Control. *Advanced Electronic Materials* **6**, 1901090 (2020).

13 C. Murapaka, P. Sethi, S. Goolaup & W.S. Lew. Reconfigurable logic via gate controlled domain wall trajectory in magnetic network structure. *Scientific Reports* **6**, 1-11 (2016).

14 D.E. Nikonov & I.A. Young. Benchmarking spintronic logic devices based on magnetoelectric oxides. *Journal of Materials Research* **29**, 2109-2115 (2014).

15 B. Rana & Y. Otani. Voltage-controlled reconfigurable spin-wave nanochannels and logic devices. *Physical Review Applied* **9**, 014033 (2018).

16 V.E. Demidov, S. Urazhdin, H. Ulrichs, V. Tiberkevich, A. Slavin, D. Baither, G. Schmitz & S.O. Demokritov. Magnetic nano-oscillator driven by pure spin current. *Nature Materials* **11**, 1028-1031 (2012).

17 V.E. Demidov, S. Urazhdin & S.O. Demokritov. Direct observation and mapping of spin waves emitted by spin-torque nano-oscillators. *Nature Materials* **9**, 984-988 (2010).

18 S. Kaka, M.R. Pufall, W.H. Rippard, T.J. Silva, S.E. Russek & J.A. Katine. Mutual phase-locking of microwave spin torque nano-oscillators. *Nature* **437**, 389-392 (2005).

19 T. Chen, R.K. Dumas, A. Eklund, P.K. Muduli, A. Houshang, A.A. Awad, P. Dürrenfeld, B.G. Malm, A. Rusu & J. Åkerman. Spin-torque and spin-Hall nano-oscillators. *Proceedings of the IEEE* **104**, 1919-1945 (2016).

20 W.H. Rippard, M.R. Pufall, S. Kaka, T.J. Silva, S.E. Russek & J.A. Katine. Injection locking and phase control of spin transfer nano-oscillators. *Physical Review Letters* **95**, 067203 (2005).

21 S.S. Parkin, M. Hayashi & L. Thomas. Magnetic domain-wall racetrack memory. *Science* **320**, 190-194 (2008).

22 C.C.I. Ang, W.L. Gan & W.S. Lew. Bilayer skyrmion dynamics on a magnetic anisotropy gradient. *New Journal of Physics* **21**, 043006 (2019).

23 S. Parkin & S.-H. Yang. Memory on the racetrack. *Nature Nanotechnology* **10**, 195-198 (2015).

24 Y. Zhang, W. Zhao, D. Ravelosona, J.-O. Klein, J. Kim & C. Chappert. Perpendicular-magnetic-anisotropy CoFeB racetrack memory. *Journal of Applied Physics* **111**, 093925 (2012).

25 X. Zhang, G. Zhao, H. Fangohr, J.P. Liu, W. Xia, J. Xia & F. Morvan. Skyrmion-skyrmion and skyrmion-edge repulsions in skyrmion-based racetrack memory. *Scientific Reports* **5**, 1-6 (2015).

26 M. Bibes & A. Barthélémy. Towards a magnetoelectric memory. *Nature Materials* **7**, 425-426 (2008).

27 T. Wu, A. Bur, K. Wong, P. Zhao, C.S. Lynch, P.K. Amiri, K.L. Wang & G.P. Carman. Electrical control of reversible and permanent magnetization reorientation for magnetoelectric memory devices. *Applied Physics Letters* **98**, 262504 (2011).

28 N. Tiercelin, Y. Dusch, V. Preobrazhensky & P. Pernod. Magnetoelectric memory using orthogonal magnetization states and magnetoelastic switching. *Journal of Applied Physics* **109**, 07D726 (2011).

29 G. Binasch, P. Grünberg, F. Saurenbach & W. Zinn. Enhanced magnetoresistance in layered magnetic structures with antiferromagnetic interlayer exchange. *Physical Review B* **39**, 4828 (1989).

30 M.N. Baibich, J.M. Broto, A. Fert, F.N. Van Dau, F. Petroff, P. Etienne, G. Creuzet, A. Friederich & J. Chazelas. Giant magnetoresistance of (001)Fe/(001)Cr magnetic superlattices. *Physical Review Letters* **61**, 2472 (1988).

31 T. Miyazaki & N. Tezuka. Giant magnetic tunneling effect in Fe/Al_2O_3/Fe junction. *Journal of Magnetism and Magnetic Materials* **139**, L231-L234 (1995).

32 J.S. Moodera, L.R. Kinder, T.M. Wong & R. Meservey. Large magnetoresistance at room temperature in ferromagnetic thin film tunnel junctions. *Physical Review Letters* **74**, 3273 (1995).

33 X. Fong, Y. Kim, R. Venkatesan, S.H. Choday, A. Raghunathan & K. Roy. Spin-transfer torque memories: Devices, circuits, and systems. *Proceedings of the IEEE* **104**, 1449-1488 (2016).

34 S. Tehrani, J. Slaughter, E. Chen, M. Durlam, J. Shi & M. DeHerren. Progress and outlook for MRAM technology. *IEEE Transactions on Magnetics* **35**, 2814-2819 (1999).

35 I. Prejbeanu, M. Kerekes, R.C. Sousa, H. Sibuet, O. Redon, B. Dieny & J. Nozières. Thermally assisted MRAM. *Journal of Physics: Condensed Matter* **19**, 165218 (2007).

36 I.L. Prejbeanu, S. Bandiera, J. Alvarez-Hérault, R.C. Sousa, B. Dieny & J.-P. Nozières. Thermally assisted MRAMs: ultimate scalability and logic functionalities. *Journal of Physics D: Applied Physics* **46**, 074002 (2013).

37 A. Khvalkovskiy, D. Apalkov, S. Watts, R. Chepulskii, R. Beach, A. Ong, X. Tang, A. Driskill-Smith, W. Butler & P. Visscher. Basic principles of STT-MRAM cell operation in memory arrays. *Journal of Physics D: Applied Physics* **46**, 074001 (2013).

38 D. Apalkov, A. Khvalkovskiy, S. Watts, V. Nikitin, X. Tang, D. Lottis, K. Moon, X. Luo, E. Chen & A. Ong. Spin-transfer torque magnetic random access memory (STT-MRAM). *ACM Journal on Emerging Technologies in Computing Systems (JETC)* **9**, 1-35 (2013).

39 L. Liu, C.-F. Pai, Y. Li, H. Tseng, D. Ralph & R. Buhrman. Spin-torque switching with the giant spin Hall effect of tantalum. *Science* **336**, 555-558 (2012).

40 G. Yu, P. Upadhyaya, Y. Fan, J.G. Alzate, W. Jiang, K.L. Wong, S. Takei, S.A. Bender, L.-T. Chang & Y. Jiang. Switching of perpendicular magnetization by spin–orbit torques in the absence of external magnetic fields. *Nature Nanotechnology* **9**, 548-554 (2014).

41 A. Brataas & K.M. Hals. Spin–orbit torques in action. *Nature Nanotechnology* **9**, 86-88 (2014).

42 I.M. Miron, K. Garello, G. Gaudin, P.-J. Zermatten, M.V. Costache, S. Auffret, S. Bandiera, B. Rodmacq, A. Schuhl & P. Gambardella. Perpendicular switching of a single ferromagnetic layer induced by in-plane current injection. *Nature* **476**, 189-193 (2011).

43 F. Oboril, R. Bishnoi, M. Ebrahimi & M.B. Tahoori. Evaluation of hybrid memory technologies using SOT-MRAM for on-chip cache hierarchy. *IEEE Transactions on Computer-Aided Design of Integrated Circuits and Systems* **34**, 367-380 (2015).

44 G. Prenat, K. Jabeur, P. Vanhauwaert, G. Di Pendina, F. Oboril, R. Bishnoi, M. Ebrahimi, N. Lamard, O. Boulle & K. Garello. Ultra-fast and high-reliability SOT-MRAM: From cache replacement to normally-off computing. *IEEE Transactions on Multi-Scale Computing Systems* **2**, 49-60 (2015).

45 Y. Seo, K.-W. Kwon & K. Roy. Area-efficient SOT-MRAM with a Schottky diode. *IEEE Electron Device Letters* **37**, 982-985 (2016).

46 L. Liu, T. Moriyama, D. Ralph & R. Buhrman. Spin-torque ferromagnetic resonance induced by the spin Hall effect. *Physical Review Letters* **106**, 036601 (2011).

47 C.-F. Pai, L. Liu, Y. Li, H. Tseng, D. Ralph & R. Buhrman. Spin transfer torque devices utilizing the giant spin Hall effect of tungsten. *Applied Physics Letters* **101**, 122404 (2012).

48 L. Liu, O. Lee, T. Gudmundsen, D. Ralph & R. Buhrman. Current-induced switching of perpendicularly magnetized magnetic layers using spin torque from the spin Hall effect. *Physical Review Letters* **109**, 096602 (2012).

49 Y. Wang, P. Deorani, X. Qiu, J.H. Kwon & H. Yang. Determination of intrinsic spin Hall angle in Pt. *Applied Physics Letters* **105**, 152412 (2014).

50 J. Sinova, S.O. Valenzuela, J. Wunderlich, C. Back & T. Jungwirth. Spin hall effects. *Reviews of Modern Physics* **87**, 1213 (2015).

51 A. Hoffmann. Spin Hall effects in metals. *IEEE Transactions on Magnetics* **49**, 5172-5193 (2013).

52 T. Kimura, Y. Otani, T. Sato, S. Takahashi & S. Maekawa. Room-temperature reversible spin Hall effect. *Physical Review Letters* **98**, 156601 (2007).

53 Z. Feng, J. Hu, L. Sun, B. You, D. Wu, J. Du, W. Zhang, A. Hu, Y. Yang & D. Tang. Spin Hall angle quantification from spin pumping and microwave photoresistance. *Physical Review B* **85**, 214423 (2012).

54 H. Nakayama, K. Ando, K. Harii, T. Yoshino, R. Takahashi, Y. Kajiwara, K.-i. Uchida, Y. Fujikawa & E. Saitoh. Geometry dependence on inverse spin Hall effect induced by spin pumping in $Ni_{81}Fe_{19}$/Pt films. *Physical Review B* **85**, 144408 (2012).

55 K. Ando, S. Takahashi, K. Harii, K. Sasage, J. Ieda, S. Maekawa & E. Saitoh. Electric manipulation of spin relaxation using the spin Hall effect. *Physical Review Letters* **101**, 036601 (2008).

56 M. Althammer, S. Meyer, H. Nakayama, M. Schreier, S. Altmannshofer, M. Weiler, H. Huebl, S. Geprägs, M. Opel & R. Gross. Quantitative study of the spin Hall magnetoresistance in ferromagnetic insulator/normal metal hybrids. *Physical Review B* **87**, 224401 (2013).

57 C. Hahn, G. De Loubens, O. Klein, M. Viret, V.V. Naletov & J.B. Youssef. Comparative measurements of inverse spin Hall effects and magnetoresistance in YIG/Pt and YIG/Ta. *Physical Review B* **87**, 174417 (2013).

58 J. Bass & W.P. Pratt. Spin-diffusion lengths in metals and alloys, and spin-flipping at metal/metal interfaces: an experimentalist's critical review. *Journal of Physics: Condensed Matter* **19**, 183201 (2007).

59 J.-C. Rojas-Sánchez, N. Reyren, P. Laczkowski, W. Savero, J.-P. Attané, C. Deranlot, M. Jamet, J.-M. George, L. Vila & H. Jaffrès. Spin pumping and inverse spin Hall effect in platinum: the essential role of spin-memory loss at metallic interfaces. *Physical Review Letters* **112**, 106602 (2014).

60 W. Zhang, W. Han, X. Jiang, S.-H. Yang & S.S. Parkin. Role of transparency of platinum–ferromagnet interfaces in determining the intrinsic magnitude of the spin Hall effect. *Nature Physics* **11**, 496-502 (2015).

61 C.-F. Pai, Y. Ou, L.H. Vilela-Leão, D. Ralph & R. Buhrman. Dependence of the efficiency of spin Hall torque on the transparency of Pt/ferromagnetic layer interfaces. *Physical Review B* **92**, 064426 (2015).

62 S. Emori, A. Matyushov, H.-M. Jeon, C.J. Babroski, T. Nan, A.M. Belkessam, J.G. Jones, M.E. McConney, G.J. Brown & B.M. Howe. Spin-orbit torque and spin pumping in YIG/Pt with interfacial insertion layers. *Applied Physics Letters* **112**, 182406 (2018).

63 D. Lee, J. Kim, H. Park, K.-J. Lee, B.-K. Ju, H.C. Koo, B.-C. Min & O. Lee. Spin-orbit torque and magnetic damping in tailored ferromagnetic bilayers. *Physical Review Applied* **10**, 024029 (2018).

64 X. Fan, H. Celik, J. Wu, C. Ni, K.-J. Lee, V.O. Lorenz & J.Q. Xiao. Quantifying interface and bulk contributions to spin–orbit torque in magnetic bilayers. *Nature Communications* **5**, 1-8 (2014).

65 L. Zhu, L. Zhu, S. Shi, M. Sui, D. Ralph & R. Buhrman. Enhancing spin-orbit torque by strong interfacial scattering from ultrathin insertion layers. *Physical Review Applied* **11**, 061004 (2019).

66 L. Zhu, D.C. Ralph & R.A. Buhrman. Enhancement of spin transparency by interfacial alloying. *Physical Review B* **99**, 180404 (2019).

67 H. Mazraati, M. Zahedinejad & J. Åkerman. Improving the magnetodynamical properties of NiFe/Pt bilayers through Hf dusting. *Applied Physics Letters* **113**, 092401 (2018).

68 S. Dutta, A. Bose, A. Tulapurkar, R. Buhrman & D. Ralph. Interfacial and bulk spin Hall contributions to fieldlike spin-orbit torque generated by iridium. *Physical Review B* **103**, 184416 (2021).

69 T.-Y. Chen, C.-T. Wu, H.-W. Yen & C.-F. Pai. Tunable spin-orbit torque in Cu-Ta binary alloy heterostructures. *Physical Review B* **96**, 104434 (2017).

70 A. Razavi, H. Wu, B. Dai, H. He, D. Wu, K. Wong, G. Yu & K.L. Wang. Spin–orbit torques in structures with asymmetric dusting layers. *Applied Physics Letters* **117**, 182403 (2020).

71 M. Tokaç, S. Bunyaev, G. Kakazei, D. Schmool, D. Atkinson & A. Hindmarch. Interfacial structure dependent spin mixing conductance in cobalt thin films. *Physical Review Letters* **115**, 056601 (2015).

72 S. Woo, M. Mann, A.J. Tan, L. Caretta & G.S. Beach. Enhanced spin-orbit torques in Pt/Co/Ta heterostructures. *Applied Physics Letters* **105**, 212404 (2014).

73 L. Huang, S. He, Q.J. Yap & S.T. Lim. Engineering magnetic heterostructures to obtain large spin Hall efficiency for spin-orbit torque devices. *Applied Physics Letters* **113**, 022402 (2018).

74 G.D.H. Wong, W.C. Law, F.N Tan, W.L. Gan, C.C.I. Ang, Z. Xu, C.S. Seet & W.S. Lew. Thermal behavior of spin-current generation in Pt_xCu_{1-x} devices characterized through spin-torque ferromagnetic resonance. *Scientific Reports* **10**, 1-8 (2020).

75 M. Morota, Y. Niimi, K. Ohnishi, D. Wei, T. Tanaka, H. Kontani, T. Kimura & Y. Otani. Indication of intrinsic spin Hall effect in 4d and 5d transition metals. *Physical Review B* **83**, 174405 (2011).

76 X. Qiu, P. Deorani, K. Narayanapillai, K.-S. Lee, K.-J. Lee, H.-W. Lee & H. Yang. Angular and temperature dependence of current induced spin-orbit effective fields in Ta/CoFeB/MgO nanowires. *Scientific Reports* **4**, 4491, doi:10.1038/srep04491 (2014).

77 P. Deorani & H. Yang. Role of spin mixing conductance in spin pumping: Enhancement of spin pumping efficiency in Ta/Cu/Py structures. *Applied Physics Letters* **103**, 232408 (2013).

78 C. Zhang, M. Yamanouchi, H. Sato, S. Fukami, S. Ikeda, F. Matsukura & H. Ohno. Magnetotransport measurements of current induced effective fields in Ta/CoFeB/MgO. *Applied Physics Letters* **103**, 262407 (2013).

79 H. Wang, C. Du, Y. Pu, R. Adur, P.C. Hammel & F. Yang. Scaling of spin Hall angle in 3d, 4d, and 5d metals from $Y_3Fe_5O_{12}$/metal spin pumping. *Physical review letters* **112**, 197201 (2014).

80 D. Qu, S. Huang, B. Miao, S. Huang & C. Chien. Self-consistent determination of spin Hall angles in selected 5d metals by thermal spin injection. *Physical Review B* **89**, 140407 (2014).

81 J. Liu, T. Ohkubo, S. Mitani, K. Hono & M. Hayashi. Correlation between the spin Hall angle and the structural phases of early 5d transition metals. *Applied Physics Letters* **107**, 232408 (2015).

82 K. Kondou, H. Sukegawa, S. Kasai, S. Mitani, Y. Niimi & Y. Otani. Influence of inverse spin Hall effect in spin-torque ferromagnetic resonance measurements. *Applied Physics Express* **9**, 023002 (2016).

83 J. Kim, P. Sheng, S. Takahashi, S. Mitani & M. Hayashi. Spin Hall magnetoresistance in metallic bilayers. *Physical Review Letters* **116**, 097201 (2016).

84 Q. Hao & G. Xiao. Giant spin Hall effect and switching induced by spin-transfer torque in a $W/Co_{40}Fe_{40}B_{20}/MgO$ structure with perpendicular magnetic anisotropy. *Physical Review Applied* **3**, 034009 (2015).

85 Q. Hao, W. Chen & G. Xiao. Beta (β) tungsten thin films: Structure, electron transport, and giant spin Hall effect. *Applied Physics Letters* **106**, 182403 (2015).

86 S. Cho, S.-h.C. Baek, K.-D. Lee, Y. Jo & B.-G. Park. Large spin Hall magnetoresistance and its correlation to the spin-orbit torque in W/CoFeB/MgO structures. *Scientific Reports* **5**, 1-9 (2015).

87 J. Yu, X. Qiu, W. Legrand & H. Yang. Large spin-orbit torques in Pt/Co-Ni/W heterostructures. *Applied Physics Letters* **109**, 042403 (2016).

88 M. Gabor, T. Petrisor Jr, R. Mos, A. Mesaros, M. Nasui, M. Belmeguenai, F. Zighem & C. Tiusan. Spin–orbit torques and magnetization switching in W/Co_2FeAl/MgO structures. *Journal of Physics D: Applied Physics* **49**, 365003 (2016).

89 R. Ramaswamy, Y. Wang, M. Elyasi, M. Motapothula, T. Venkatesan, X. Qiu & H. Yang. Extrinsic spin Hall effect in $Cu_{1-x}Pt_x$. *Physical Review Applied* **8**, 024034 (2017).

90 H. Bouloussa, R. Ramaswamy, Y. Roussigné, A. Stashkevich, H. Yang, M. Belmeguenai & S. Chérif. Pt concentration dependence of the interfacial Dzyaloshinskii–Moriya interaction, the Gilbert damping parameter and the magnetic anisotropy in Py/$Cu_{1-x}Pt_x$ systems. *Journal of Physics D: Applied Physics* **52**, 055001 (2018).

91 L. Zhu, D.C. Ralph & R.A. Buhrman. Maximizing Spin-Orbit Torque Generated by the Spin Hall Effect of Pt. *arXiv Preprint arXiv:2106.04992* (2021).

92 C.Y. Hu & C.F. Pai. Benchmarking of Spin–Orbit Torque Switching Efficiency in Pt Alloys. *Advanced Quantum Technologies* **3**, 2000024 (2020).

93 L. Zhu, D.C. Ralph & R.A. Buhrman. Highly efficient spin-current generation by the spin Hall effect in $Au_{1-x}Pt_x$. *Physical Review Applied* **10**, 031001 (2018).

94 Y. Xu, Y. Yang, H. Xie & Y. Wu. Spin Hall magnetoresistance sensor using Au_xPt_{1-x} as the spin-orbit torque biasing layer. *Applied Physics Letters* **115**, 182406 (2019).

95 L. Zhu, D. Ralph & R. Buhrman. Spin-orbit torques in heavy-metal–ferromagnet bilayers with varying strengths of interfacial spin-orbit coupling. *Physical Review Letters* **122**, 077201 (2019).

96 B. Coester, G.D.H. Wong, Z. Xu, J. Tang, W.L. Gan & W.S. Lew. Enhanced spin Hall conductivity in tungsten-copper alloys. *Journal of Magnetism and Magnetic Materials* **523**, 167545 (2021).

97 P. Laczkowski, J.-C. Rojas-Sánchez, W. Savero-Torres, H. Jaffrès, N. Reyren, C. Deranlot, L. Notin, C. Beigné, A. Marty & J.-P. Attané. Experimental evidences of a large extrinsic spin Hall effect in AuW alloy. *Applied Physics Letters* **104**, 142403 (2014).

98 T.Y. Chen, T.-C. Chuang, S.-Y. Huang, H.-W. Yen & C.-F. Pai. Spin-orbit torque from a magnetic heterostructure of high-entropy alloy. *Physical Review Applied* **8**, 044005 (2017).

99 P. Laczkowski, H. Jaffrès, W. Savero-Torres, J.C. Rojas-Sánchez, Y. Fu, N. Reyren, C. Deranlot, L. Notin, C. Beigné & J.-P. Attané. Evaluation of spin diffusion length of AuW alloys using spin absorption experiments in the limit of large spin-orbit interactions. *Physical Review B* **92**, 214405 (2015).

100 D. Qu, S. Huang, G. Guo & C. Chien. Inverse spin Hall effect in Au_xTa_{1-x} alloy films. *Physical Review B* **97**, 024402 (2018).

101 Y. Niimi, M. Morota, D. Wei, C. Deranlot, M. Basletic, A. Hamzic, A. Fert & Y. Otani. Extrinsic spin Hall effect induced by iridium impurities in copper. *Physical Review Letters* **106**, 126601 (2011).

102 Y. Niimi, Y. Kawanishi, D. Wei, C. Deranlot, H. Yang, M. Chshiev, T. Valet, A. Fert & Y. Otani. Giant spin Hall effect induced by skew scattering from bismuth impurities inside thin film CuBi alloys. *Physical Review Letters* **109**, 156602 (2012).

103 Y. Niimi, H. Suzuki, Y. Kawanishi, Y. Omori, T. Valet, A. Fert & Y. Otani. Extrinsic spin Hall effects measured with lateral spin valve structures. *Physical Review B* **89**, 054401 (2014).

104 Y. Niimi & Y. Otani. Reciprocal spin Hall effects in conductors with strong spin–orbit coupling: a review. *Reports on Progress in Physics* **78**, 124501 (2015).

105 Y. Tian, L. Ye & X. Jin. Proper scaling of the anomalous Hall effect. *Physical Review Letters* **103**, 087206 (2009).

106 R. Asomoza, A. Fert & R. Reich. Gadolinium-heavy rare earth alloys: preparation, metallographic study and extraordinary hall effect. *Journal of the Less Common Metals* **90**, 177-201 (1983).

107 A. Fert & P.M. Levy. Spin Hall effect induced by resonant scattering on impurities in metals. *Physical Review Letters* **106**, 157208 (2011).

108 L. Zhu & R. Buhrman. Maximizing Spin-Orbit-Torque Efficiency of Pt/Ti Multilayers: Trade-Off Between Intrinsic Spin Hall Conductivity and Carrier Lifetime. *Physical Review Applied* **12**, 051002 (2019).

109 E. Liu, T. Fache, D. Cespedes-Berrocal, Z. Zhang, S. Petit-Watelot, S. Mangin, F. Xu & J.-C. Rojas-Sánchez. Strain-Enhanced Charge-to-Spin Conversion in Ta/Fe/Pt Multilayers Grown on Flexible Mica Substrate. *Physical Review Applied* **12**, 044074 (2019).

110 M. Filianina, J.-P. Hanke, K. Lee, D.S. Han, S. Jaiswal, A. Rajan, G. Jakob, Y. Mokrousov & M. Kläui. Electric-field control of spin-orbit torques in perpendicularly magnetized W/CoFeB/MgO films. *Physical Review Letters* **124**, 217701 (2020).

111 T. Nan, J.M. Hu, M. Dai, S. Emori, X. Wang, Z. Hu, A. Matyushov, L.Q. Chen & N. Sun. A Strain-Mediated Magnetoelectric-Spin-Torque Hybrid Structure. *Advanced Functional Materials* **29**, 1806371 (2019).

112 H. An, S. Haku, Y. Kanno, H. Nakayama, H. Maki, J. Shi & K. Ando. Manipulation of Spin-Torque Generation Using Ultrathin Au. *Physical Review Applied* **9**, 064016 (2018).

113 R. Suzuki, S. Haku, H. Hayashi & K. Ando. Spin-torque ferromagnetic resonance in electrochemically etched metallic device. *Applied Physics Express* **13**, 043007 (2020).

114 E. Masanet, A. Shehabi, N. Lei, S. Smith & J. Koomey. Recalibrating global data center energy-use estimates. Science 367, 984-986 (2020).

Chapter 2 Background

In this chapter, we will be discussing the fundamentals and theoretical background of the phenomena used in this thesis. We begin with the description of the magnetization dynamics to help understand the different components acting on the magnetization of a ferromagnet. Next, we discuss about spin current generation *via* spin-orbit coupling through a phenomenon known as the spin Hall effect. Subsequently, we examine the spin-transfer torque and magnetoresistance which gives the MRAM its characteristics to function as a memory device.

2.1 Magnetic Dynamics

In 1935, Landau and Lifshitz proposed the LL model to describe the dynamics of local magnetization $\vec{M}$,

$$\frac{\mathrm{d}\vec{M}}{\mathrm{d}t} = -\gamma\mu_0\vec{M}\times\vec{H}_{\mathrm{eff}} \tag{2.1.1}$$

where $\gamma = \frac{ge}{2m_e}$ is the gyromagnetic ratio, g is the g-factor, e is the electron charge, m_e is the electron mass, μ_0 is the permeability of free space and $\vec{H}_{\mathrm{eff}}$ is the effective field.[1-3] The $\vec{H}_{\mathrm{eff}}$ comprises contributions such as the external magnetic field H_{ext}, anisotropy field H_{ani} and demagnetization field H_{demag}. For an electron, the g-factor of its spin is approximately 2 and 1 for its orbital angular momentum. According to the LL model, the magnetic moment is set in a precessional motion when it experiences $\vec{H}_{\mathrm{eff}}$ and the axis of the precession is about the direction of the $\vec{H}_{\mathrm{eff}}$. Equation 2.1.1 predicts that the precession is undamped, and a constant precessional cone angle is anticipated. However, in reality, when the magnetization is misaligned with the $\vec{H}_{\mathrm{eff}}$, a finite time is required for the magnetization to change its precession trajectory to the direction of minimal energy. An amendment was required for the LL model and in 1955, Gilbert came up with a dissipation term and that was the birth of the Landau-Lifshitz-Gilbert (LLG) equation.[4] The LLG equation is given by:

(2.1.2)

$$\frac{\mathrm{d}\vec{M}}{\mathrm{d}t} = -\gamma\mu_0\vec{M}\times\vec{H}_{\mathrm{eff}} + \alpha\vec{M}\times\frac{\mathrm{d}\vec{M}}{\mathrm{d}t}$$

where α is a dimensionless parameter known as the Gilbert damping. The first and second term in the LLG equation corresponds to the precession and damping term respectively as shown in Figure 2-1.

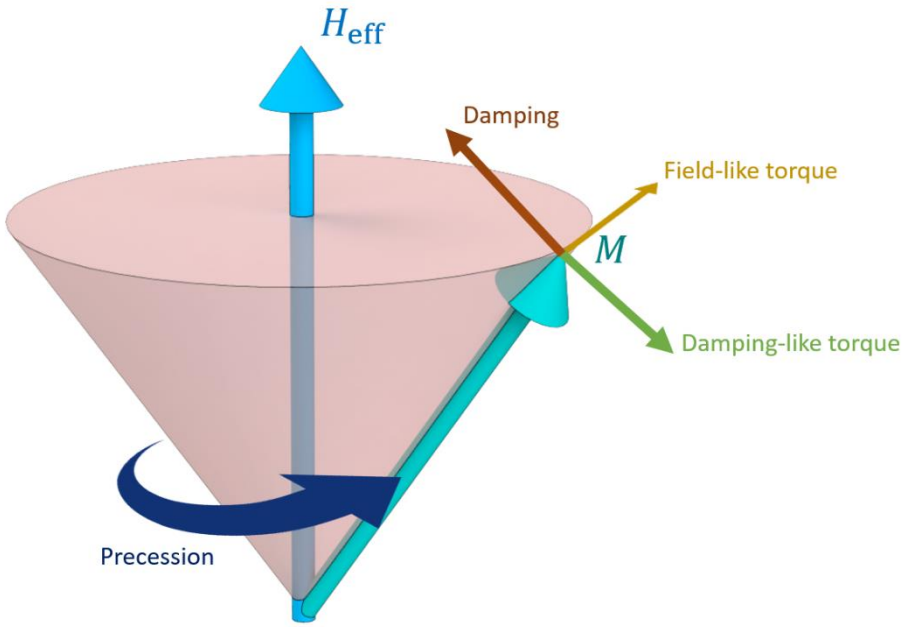

Figure 2-1 Illustration of the magnetization dynamics described by the Landau-Lifshitz-Gilbert (LLG) equation. The green arrow represents the magnetization m precessing about the light blue arrow representing the effective field H_{eff}. The precession and damping of the magnetization are depicted as the navy blue and maroon arrow shown above. The lime-green and yellow arrows represent the current-induced damping-like and field-like torque direction.

When polarized electrons are injected into a ferromagnet, the magnetization of the ferromagnet experiences a torque that can lead to (i) an increase in damping, (ii) a sustained precession, or (iii) magnetization reversal. depending on the current direction. Incorporating this current-induced torque into the magnetic dynamics equation will lead us to a modified equation known as the Landau–Lifshitz–Gilbert–Slonczewski (LLGS) equation given by:[5,6]

$$\frac{\mathrm{d}\vec{M}}{\mathrm{d}t} = -\gamma\mu_0\vec{M}\times\vec{H}_{\mathrm{eff}} + \alpha\vec{M}\times\frac{\mathrm{d}\vec{M}}{\mathrm{d}t} + \tau_{\mathrm{DL}}\vec{M}\times\left(\vec{\sigma}\times\vec{M}\right) + \tau_{\mathrm{FL}}\vec{\sigma}\times\vec{M} \qquad (2.1.3)$$

where τ_{DL} represents the damping-like torque, τ_{FL} is the field-like torque and $\vec{\sigma}$ is the injected spin polarization orientation.

2.2 Magnetoresistance

Magnetoresistance is the change in electrical resistance of a material corresponding to an externally applied magnetic field. First discovered in 1856, William Thomson[58] observed an increase in electrical resistance when he passes current through pieces of iron in the same direction as the applied magnetic field and a decrease when he passes current through the orthogonal direction. This phenomenon was later known as anisotropic magnetoresistance (AMR) and it is one of the many types of magnetoresistance.

The AMR of a ferromagnet describes the resistance dependence of the ferromagnet on the relative angle φ between its magnetization $\vec{M}$ and the charge current J_C. As such AMR can be expressed as the following[59,60]:

$$\rho_{xx} = \rho_{\perp} + \left(\rho_{\parallel} - \rho_{\perp}\right)\cos^2\varphi \tag{2.2.4}$$

where $\rho_{\parallel}$ is the longitudinal resistivity of the ferromagnet when $\vec{M}$ is parallel to J_C and $\rho_{\perp}$ is when $\vec{M}$ and J_C are orthogonal with each other. Therefore, from Equation 2.2.4, the AMR strength is maximum when J_C is aligned with $\vec{M}$. Experimentally, the $\vec{M}$ is controlled and changed by applying an external magnetic field. Here, the key figure of merit used to define the effect of the AMR is $\frac{\rho_{\parallel} - \rho_{\perp}}{\rho} = \frac{\Delta\rho}{\rho}$. On a microscopic level, the origin of the AMR is due to the anisotropic scattering of the electrons in the ferromagnet with respect to the magnetization direction. Besides a change in electrical resistance in the longitudinal direction, the AMR can cause a resistance change in the transverse direction. This transverse anisotropic resistance effect is known as the planar Hall effect and its effects can be described by[61]:

$$\rho_{xy}^{P} = \left(\rho_{\parallel} - \rho_{\perp}\right)\sin\varphi\cos\varphi. \tag{2.2.5}$$

With the discovery of the spin Hall effect, a new type of magnetoresistance called the spin Hall magnetoresistance (SMR) was proposed.[62] The SMR describes the behaviors of longitudinal and transverse magnetoresistance in SHE-based NM/FM systems.[63,64] The strength of the SMR is typically the same as the AMR and PHE, however, its origin is due to

the inverse spin Hall effect (ISHE) from the spin accumulation at the NM/FM interface instead of the spin-dependent scattering.

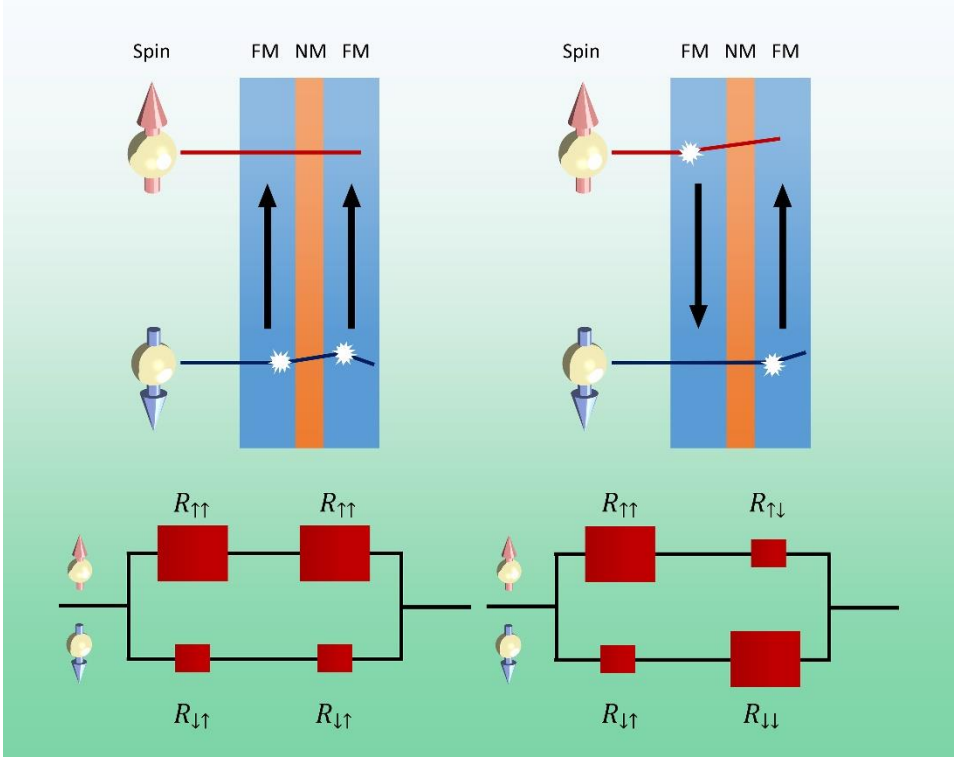

Figure 2-2 (Top) Illustration of the scattering effect experienced by the junction in the CPP configuration. (Bottom) Circuit diagram explaining the two-current model.

In 1988, a large magnetoresistance effect was observed by Fert and Grünberg in a multilayer structure consisting of two ferromagnets sandwiching a thin layer of normal metal. This phenomenon is named giant magnetoresistance (GMR) and with its discovery, it sparked the beginning of modern spintronics research and applications.[65,66] The GMR effect occurs in a multilayer structure consisting of two FM layer sandwiching a thin NM layer as shown in Figure 2-2. When a charge current is injected perpendicularly though the heterostructure in the current-perpendicular-to-plane (CCP) configuration, the total resistance of the structure is dependent on the relative magnetization orientation of the two FM layers allowing for structure to behave like a "spin valve". Typically, when the magnetizations of the two FM layers are parallel, the resistance (R_{P}) is smaller and when they are antiparallel, the resistance (R_{AP}) is larger. Although in a smaller magnitude, this GMR effect can also take place when a charge current passes through the multilayer structure in plane and this configuration is known as current-in-plane (CIP).[67]

The GMR effect originates from the spin-dependent scattering in the multilayer structure and this scattering can be described by the two-current model.[68] When the spin polarization is parallel to the magnetization, the majority spin will experience weaker scattering and thus result in lower resistance $\left(R_{\uparrow\uparrow} = R_{\downarrow\downarrow}\right)$ across the multilayer. However, if the spin polarization is antiparallel to the magnetization, the minority spin will tend to scatter more and hence give rise to higher resistance $\left(R_{\uparrow\downarrow} = R_{\downarrow\uparrow}\right)$. The GMR ratio can be described as:

$$\mathrm{GMR} = \frac{R_{\mathrm{AP}} - R_{\mathrm{P}}}{R_{\mathrm{P}}} = \frac{1}{4}\frac{R_{\uparrow\uparrow} - R_{\uparrow\downarrow}}{R_{\uparrow\uparrow} R_{\uparrow\downarrow}}. \tag{2.2.6}$$

On top of the GMR, another observation that largely influenced the spintronics community was the discovery of tunnel magnetoresistance (TMR). However, here, instead of using a NM layer between the two FM layer, an insulating layer is used. As discussed in the previous section, due to the majority and minority spin in the ferromagnet having different density of states (DOS), the tunnel resistance changes depending on whether the majority spin on one side tunnels to the majority or minority band on the other side of the insulator when a current is applied across the MTJ as shown in Figure 2-3.

To describe the magnetoresistance change of junctions with amorphous tunnel barriers such as AlO_x or MgO, the Jullière model can be used, where the TMR ratio is expressed as:[69]

$$\mathrm{TMR} = \frac{R_{\mathrm{AP}} - R_{\mathrm{P}}}{R_{\mathrm{P}}} = \frac{G_P - G_{\mathrm{AP}}}{G_{\mathrm{AP}}} = \frac{2P_1P_2}{1 - P_1P_2}. \tag{2.2.7}$$

Here, P_1 and P_2 refers to the spin polarization of the ferromagnets and they can be calculated from the majority and minority spin DOS at the Fermi level using the following expression:

$$P = \frac{N_{\uparrow}(\mathrm{E}_F) - N_{\downarrow}(\mathrm{E}_F)}{N_{\uparrow}(\mathrm{E}_F) + N_{\downarrow}(\mathrm{E}_F)} \tag{2.2.8}$$

where $N_{\uparrow}(\mathrm{E}_F)$ and $N_{\downarrow}(\mathrm{E}_F)$ are the DOS for the majority and minority spin at the Fermi level, respectively. By the two-current model, with the assumption that spin-flipping does not occur during tunneling, the conductance in each channel is dependent on the Fermi's golden rule and is proportional to the tunneling probability. This implies that the conductance when the

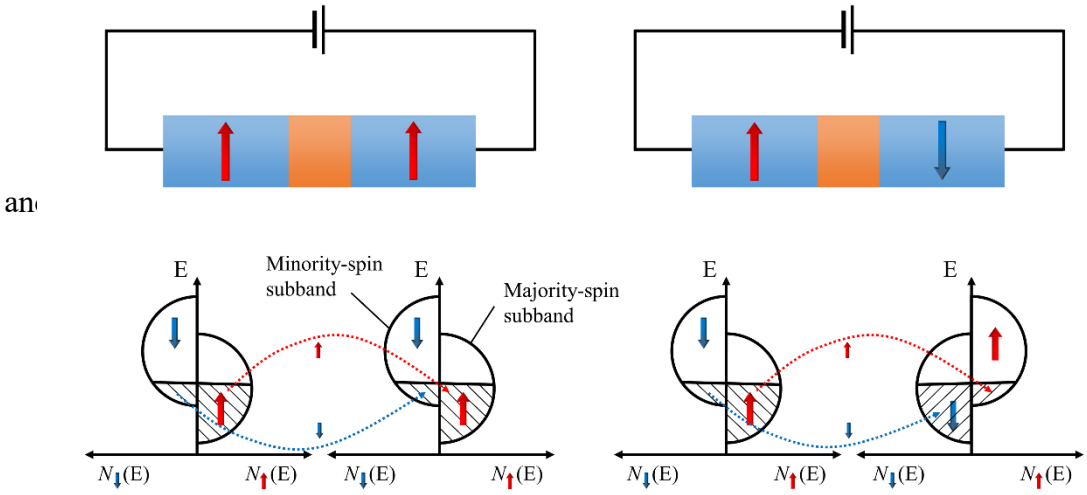

Figure 2-3 Band diagram illustrating the spin-dependent tunneling phenomena. (Left) Parallel to antiparallel state. (Right) Antiparallel to parallel state.

magnetization of the two ferromagnets are parallel (G_P) and antiparallel (G_{AP}) can be written as,

After the discovery of TMR, the race to achieve high TMR ratio began with the first significant milestone being the observed in AlO_x junctions.[70,71] Not long after in 2004, another breakthrough with the use of MgO at room temperature observed a TMR ratio of over 200% in Fe/MgO/Fe and CoFe/MgO/CoFe junctions were made.[72,73] This demonstration shed light on the feasibility of using the MTJs as memory cells for high storage density MRAM applications.

2.3 Spin-Orbit Coupling

The spin-orbit coupling (SOC), also known as spin-orbit interaction between the spin of the electron and its orbital motion around its nucleus.[7-10] When an electron with a velocity $\vec{v}$ travels through a magnetic field $\vec{B}$, it experiences a Lorentz force in the direction orthogonal to its direction of motion. The force can be described by $F = -e\vec{v} \times \vec{B}$ and the Zeeman energy it has is $F = \mu_B \vec{\sigma} \cdot \vec{B}$, where $\vec{\sigma}$ is the vector of the Pauli spin matrices, μ_B is the Bohr magnetron, e and m are the charge and mass of an electron, respectively.

By this analogy, in the rest frame S of the nucleus, when the same electron orbits through the electric field of its nucleus, the spin-orbit coupling causes the atomic energy level of the electrons to shift due to the electromagnetic interaction between the spin of the electron and the electric field. In the rest frame of the electron S', a magnetic field is induced by the interaction of the angular momentum of the electron and the electric field of the nucleus. The electric and magnetic fields can be expressed in their respective frame of reference by the following Lorentz transformation:

$$\begin{aligned} \vec{E}_{\parallel}' &= \vec{E}_{\parallel} \\ \vec{B}_{\parallel}' &= \vec{B}_{\parallel} \\ \vec{E}_{\perp}' &= \gamma(\vec{E}_{\perp} + \vec{v} \times \vec{B}) \\ \vec{B}_{\perp}' &= \gamma(\vec{B}_{\perp} + \frac{\vec{v}}{c^2} \times \vec{E}) \end{aligned} \tag{2.3.10}$$

where $\gamma = \frac{1}{\sqrt{1 - v^2/c^2}}$ is the Lorentz factor and c is the speed of light. From equation 2.3.10, the magnetic field $\vec{B}$ can be expressed as $\vec{B}' = \frac{1}{2c^2}\vec{E} \times \vec{v}$ and $\frac{1}{2}$ is the relativistic Thomas factor due to the non-inertial frame of reference.[11] The H_{SO} field that arise from the spin-orbit coupling can then be described as[12]

$$H_{\mathrm{SOC}} = \frac{\mu_{\mathrm{B}}}{2c^2}\vec{\sigma} \cdot \left(\vec{E} \times \vec{v}\right) = \mu_{\mathrm{B}}\vec{\sigma} \cdot \vec{B}. \tag{2.3.11}$$

Spin-orbit coupling can lead to an enhancement of the external magnetic field, and this can affect the perpendicular magnetic anisotropy, magnetostriction, g-factor and fine structure of the material. Another effect is the creation of spin polarization by an electrical current, which results in various phenomena such as the spin Hall effect, inverse spin Hall effect and spin relaxation. In the next section, we will discuss more about the spin Hall effect.

2.4 Spin Hall effect

The ability to generate, manipulate and detect spin currents is one of the crucial aspects of realizing SOT device application. Among the different methods, the spin Hall effect (SHE) has gained much attention from the spintronics community since its first observation more than a decade ago. Exploiting the spin-orbit coupling in bulk NM, the SHE is a phenomenon that generates a transverse pure spin current from passing a longitudinal charge current through the material without any external magnetic field.[13-15] The reverse effect, the inverse SHE (ISHE) works in the opposite matter where a pure spin current passing through the material generates a transverse charge current.[16-18] Both the SHE and ISHE occurs in material that possesses spin-orbit coupling.

The bulk SOC in the NM is attributed to the band structure of the material (intrinsic) and/or by the addition of impurities with high SOC into the material (extrinsic). The spin polarization of the accumulated spin as a result of SHE is perpendicular to both the transverse spin current and longitudinal charge current as shown in Figure 2-4. The spin current generated through SHE can be expressed using the equation $J_C = \theta_{SH}(J_C \times \hat{\sigma})$, where θ_{SH} is the spin Hall angle and $\hat{\sigma}$ is the spin current polarization. The spin Hall angle $\theta_{SH} = J_S/J_C$ of a material is the measure of the charge to spin current conversion efficiency due to SHE. Over the years, there have been many works to obtain higher spin current generation efficiency and most of them involve the exploitation of the three contributing factors to the SHE: intrinsic scattering, skew-scattering and side-jump scattering.[19-24]

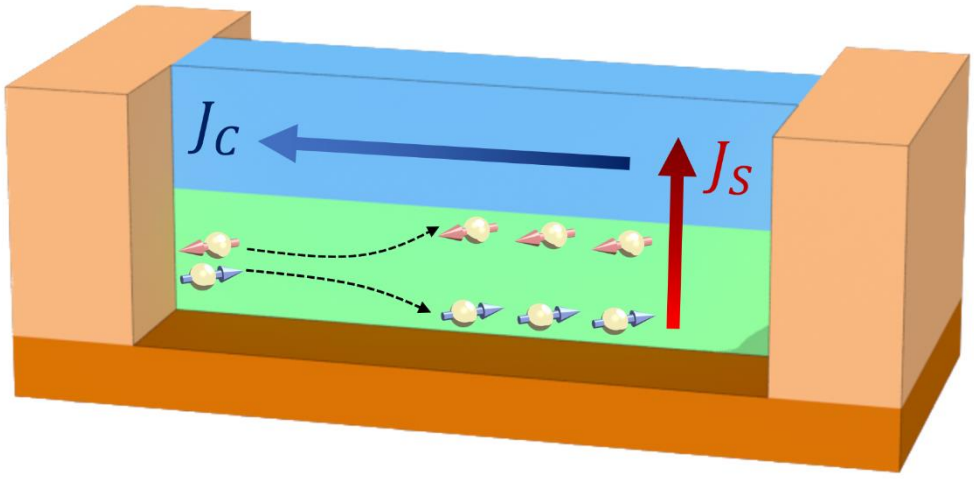

Figure 2-4 Schematic of the spin Hall effect in a bilayer ferromagnet (top blue) and normal metal (bottom green) heterostructure.

The SHE adopted its model from the widely recognized anomalous Hall effect (AHE), where the relativistic spin-orbit coupling generates an asymmetric deflection of the charge carrier depending on their spin orientation.[25] The presence of AHE can be electrically detected in a ferromagnet by applying a transverse current as a result of the population difference between the majority and minority carriers. In the 1950s, the intrinsic contribution of the AHE was first proposed by Karplus and Luttinger[26] and until recently the theory was modified with the Berry phases and Berry curvature language.[27,28] Experimentally, the intrinsic SHE was first observed in a two-dimensional semiconductor system.[29]

The intrinsic SHE can be described using the two-dimensional Rashba Hamiltonian in systems with spatial inversion asymmetry given by,

$$H_{\text{Rashba}} = \frac{p^2}{2m} - \frac{\lambda}{\hbar}\sigma \cdot (\hat{z} \times \mathbf{p}), \tag{2.4.12}$$

where $p = \hbar k$ is the 2D electron momentum, λ is the Rashba coupling constant, σ is the Pauli matrices, m is the effective mass of the electron and $\hat{z}$ is the unit vector perpendicular to the 2DEG plane.[30] However, a more general approach in the case of no inversion asymmetry, the intrinsic spin Hall conductivity can be more accurately calculated using the Berry phase and Berry curvature in the momentum space give by,

$$\sigma_{xy}^{SH-\text{int}} = \frac{e^2}{\hbar}\sum_{\boldsymbol{k}} \Omega_n^z(\boldsymbol{k}) = \frac{e^2}{\hbar}\sum_{\boldsymbol{k}}\sum_{n} f_{\boldsymbol{k}n}\, \Omega_n^z(\boldsymbol{k}), \tag{2.4.13}$$

where

$$\Omega_n^z(\boldsymbol{k}) = \sum_{n\prime \neq n} \frac{2\text{Im}\left[\langle n'k|\hat{j}^z_{\text{spin}\,x}|nk\rangle\langle nk|v_y|n'k\rangle\right]}{(E_{nk} - E_{n\prime k})(E_{nk} - E_{n'k} - \hbar\omega - i\eta)} \tag{2.4.14}$$

where n and n' are the band indices, $\hat{j}^z_{\text{spin}\,x} = \frac{\hbar}{4}\{\sigma_z, \mathbf{v}\}$ is the spin current operator, ω and η are set to zero in the dc clean limit, and the velocity operator at $\mathbf{p}$ are given by $\hbar v_i = \hbar\partial H(\mathbf{p})/\partial p_i$.[31] $\Omega_n^z(\boldsymbol{k})$ represents the Berry curvature that describes the geometric property of the Bloch wavefunction in the n th band and $f_{\boldsymbol{k}n}$ is the Fermi distribution function. Within the Berry curvature model, the intrinsic SHE can be interpreted from the perspective of the topological properties of the Bloch state near the Fermi level in a band structure and it is proportional to the integration over the Fermi Sea of the Berry's curvature of each occupied band. *ab initio* calculation such as density function and microscopic tight-binding calculation

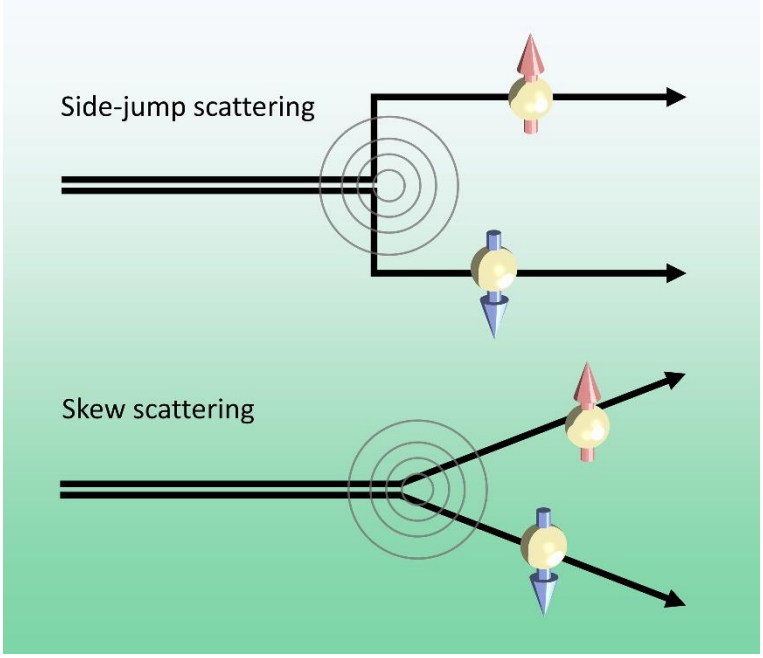

Figure 2-5 Illustration of the two main extrinsic scattering mechanisms: side-jump and skew-scattering.

has been used to quantitively predict the intrinsic spin Hall conductivity of 4d and 5d metals.[31,32]

As for the extrinsic SHE, the theoretical discovery was proposed by *Dyakonov* and *Perel*[33] back in 1971 and it was based on the asymmetric scattering model by Mott.[34] However, it took nearly three decades until the observations by *Hirsch*[35] and *Zhang*[36] helped realize the application potential of the SHE. Thereafter the first experimental observation of the extrinsic SHE was performed in a semiconductor system in 2004.[14] The extrinsic contribution of the SHE can be divided into two main scattering mechanisms: the skew-scattering and the side jump contribution as shown in Figure 2-5. Due to the presence of the spin-orbit coupling, skew-scattering causes discrete electron wave packets to scatter asymmetrically with respect to the spin polarization. The scattered spins that are polarized in opposite directions will then generate a flow of spin current in the opposite direction resulting in a nonequilibrium spin polarization. The skew-scattering contribution to the Hall conductivity is proportional to the Bloch state transport lifetime τ, and by this relation the spin Hall resistivity $\rho_{xy}^{SH-\mathrm{skew}}$ can be expressed as,

$$\rho_{xy}^{SH-\mathrm{skew}} \approx \sigma_{xy}^{SH-\mathrm{skew}} \rho_{xx}^{2} \sim \rho_{xx}. \tag{2.4.15}$$

In order to accurately predict the skew-scattering contribution to the SHE, the disorderliness of the material needs to be characterization with accuracy. In a simplified model, this contribution

arises only from the spin-orbit coupling in the disorder potential and is valid only when the disorder broadening is larger than the splitting of the bands. These constraints are to avoid inaccurate estimation of the skew-scattering contribution as a strong contribution to the skew-scattering also arises from the scattering of the spin-orbit-coupled quasiparticle from the scalar potential. Furthermore, the spin-orbit coupling of the disorder potential is also strongly renormalized by the other nearby subbands. As such, the effect of the multiband character should be neglected in these materials. First principle calculations have been performed to investigate the skew-scattering contribution in systems with impurities.[37-40]

The side-jump scattering contribution is a result of electron wave packets with an incident wave vector **k** being displaced in the transverse direction to its propagation to **k** after it scatters off an impurity with spin-orbit interaction. The scattering mechanism was first proposed by *Smit*[41,42] back in 1955 but his idea was discarded until 1964, where *Berger*[43] reintroduced it and argued that the side-jump scattering played an important role in the spin-dependent Hall effects. Breaking down the side-jump contribution further, the mechanism can be separated into two categories: (a) the extrinsic side-jump where there is an additional contribution from the impurity that has spin-orbit interaction with the conductive electrons and (b) the intrinsic side-jump where the contribution is attributed solely from the spin-orbit coupling of the discrete wave packet. Unlike the skew-scattering, the side-jump contribution to the spin Hall conductivity is scattering independent and thus the spin Hall resistivity can be expressed as

$$\rho_{xy}^{SH} = a\rho_{xx} + b\rho_{xx}^2, \tag{2.4.16}$$

where a is the side-jump contribution while b is the skew-scattering contribution.

2.5 Spin Transfer Torque

Introduced in 1996, the concept of the spin-transfer torque (STT) was first predicted by Slonczewski and Berger independently.[5,6] The mechanism made controlling the local magnetic moments using the transfer of the spin angular momentum possible without the need of using a magnetic field generated using a field line, which was previously used in field-switched MRAM cells. This discovery paved a new route for spintronics community and aided the development of high-speed and energy efficient spintronics devices such as binary memory devices,[44-46] STT nano-oscillators[47,48] and spin-wave emitters[49,50] to scale down to the sub-micrometer or even nanoscale size.[51,52]

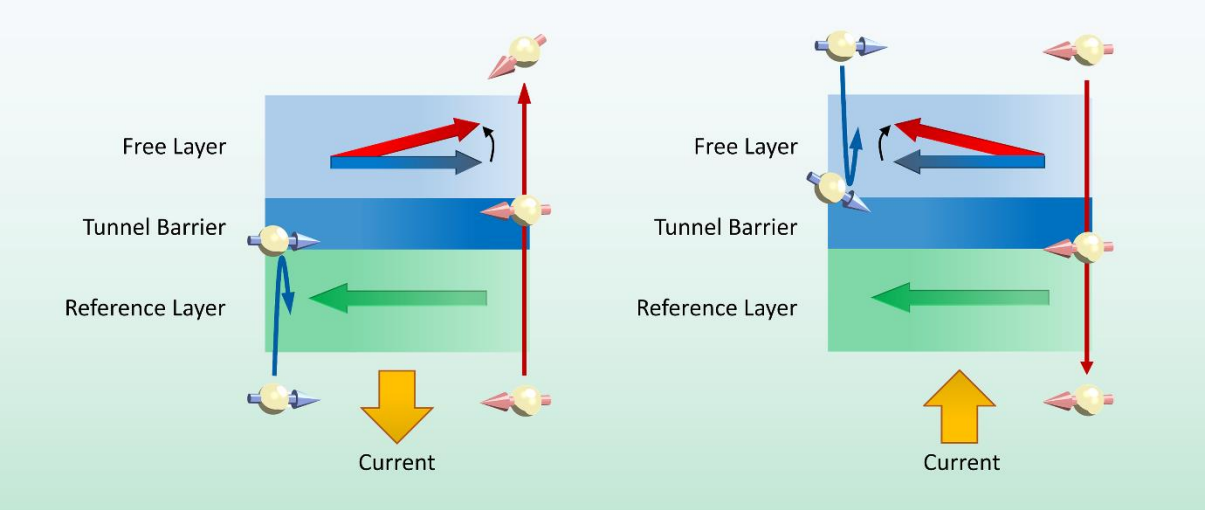

Figure 2-6 Illustration explaining how STT switches the magnetization of the MTJ. (Left) Antiparallel to parallel state. (Right) Parallel to antiparallel state.

Depending on the magnetization orientation of the free layers within the MTJ, the MTJ can either be in the antiparallel (AP) and parallel (P) configuration. To switch the magnetization of the free layer of the MTJ, a charge current is passed through it and the direction of the switching current is determined by the existing state of the MTJ. For the case of switching the MTJ state from AP to P, a charge current is injected through the MTJ from the reference layer as shown in Figure 2-6. Due to the spin filter effect, the electron spin becomes partially polarized as it passes through the reference layer. The spin polarization direction will be in the same direction as the magnetization of the reference layer. Since the free layer is adequately close, the partially polarized spin current is injected into the free layer before spin relaxation. As the spin polarization of the injected spin current is different from the magnetization direction of the free layer, the transmission of the electron flow exerts a torque on the

magnetization of the free layer via conservation of momentum. After a sufficient amount of current has passed through the MTJ, the free layer configuration is then switched to the P state by the transferred torque. On the other hand, in order to switch from the P to AP state, the charge current is passed through the opposite direction into the free layer. Again, due to the spin filter effect, the spins are partially polarized. Upon entering the reference layer, the difference in spin polarization and magnetization result in the spins reflected into the free layer exerting a torque on free layer magnetization. This process of angular momentum transfer from a spin current to the magnetization of a ferromagnet in an MTJ is known as spin-transfer torque (STT).

Besides the use of the spin filter effect, the spin-orbit coupling of a material can also generate a spin current. When a ferromagnet is placed adjacent to material of high spin-orbit coupling, the injected spin current from the material exerts a spin torque on the ferromagnet. The spin torque generated in this matter is often referred to as spin-orbit torque (SOT) to differentiate their source. The charge current required to generate the SOT is typically applied in-plane within the heterostructures as opposed to the STT. Initial experimental observations of the SOT phenomena were made in the early 2010s using NM/FM bilayer structures.[53-57] SOT can be categories into two main components: the damping-like and the field-like torque, which are described by the magnetization dynamics in Equation 2.1.3.

Reference

1 L. Landau & E. Lifshitz. On the theory of magnetic permeability dispersion in ferromagnetic solids. *Sov. Phys* **8**, 153-166 (1935).

2 A. Visintin. On Landau-Lifshitz'equations for ferromagnetism. *Japan Journal of Applied Mathematics* **2**, 69-84 (1985).

3 M. Lakshmanan. The fascinating world of the Landau–Lifshitz–Gilbert equation: an overview. *Philosophical Transactions of the Royal Society A: Mathematical, Physical and Engineering Sciences* **369**, 1280-1300 (2011).

4 T.L. Gilbert. A phenomenological theory of damping in ferromagnetic materials. *IEEE Transactions on Magnetics* **40**, 3443-3449 (2004).

5 J.C. Slonczewski. Current-driven excitation of magnetic multilayers. *Journal of Magnetism and Magnetic Materials* **159**, L1-L7 (1996).

6 L. Berger. Emission of spin waves by a magnetic multilayer traversed by a current. *Physical Review B* **54**, 9353 (1996).

7 M. Blume & R. Watson. Theory of spin-orbit coupling in atoms I. Derivation of the spin-orbit coupling constant. *Proceedings of the Royal Society of London. Series A. Mathematical and Physical Sciences* **270**, 127-143 (1962).

8 T. Dunn. Spin-orbit coupling in the first and second transition series. *Transactions of the Faraday Society* **57**, 1441-1444 (1961).

9 V. Galitski & I.B. Spielman. Spin–orbit coupling in quantum gases. *Nature* **494**, 49-54 (2013).

10 P.M. Haney, H.-W. Lee, K.-J. Lee, A. Manchon & M.D. Stiles. Current induced torques and interfacial spin-orbit coupling: Semiclassical modeling. *Physical Review B* **87**, 174411 (2013).

11 S. Blundell. (American Association of Physics Teachers, 2003).

12 A. Manchon, H.C. Koo, J. Nitta, S. Frolov & R. Duine. New perspectives for Rashba spin–orbit coupling. *Nature Materials* **14**, 871-882 (2015).

13 J. Sinova, S.O. Valenzuela, J. Wunderlich, C. Back & T. Jungwirth. Spin hall effects. *Reviews of Modern Physics* **87**, 1213 (2015).

14 Y.K. Kato, R.C. Myers, A.C. Gossard & D.D. Awschalom. Observation of the spin Hall effect in semiconductors. *Science* **306**, 1910-1913 (2004).

15 S.O. Valenzuela & M. Tinkham. Direct electronic measurement of the spin Hall effect. *Nature* **442**, 176-179 (2006).

16 T. Kimura, Y. Otani, T. Sato, S. Takahashi & S. Maekawa. Room-temperature reversible spin Hall effect. *Physical Review Letters* **98**, 156601 (2007).

17 E. Saitoh, M. Ueda, H. Miyajima & G. Tatara. Conversion of spin current into charge current at room temperature: Inverse spin-Hall effect. *Applied Physics Letters* **88**, 182509 (2006).

18 K. Ando, S. Takahashi, J. Ieda, Y. Kajiwara, H. Nakayama, T. Yoshino, K. Harii, Y. Fujikawa, M. Matsuo & S. Maekawa. Inverse spin-Hall effect induced by spin pumping in metallic system. *Journal of Applied Physics* **109**, 103913 (2011).

19 Z. Xu, G.D.H. Wong, J. Tang, E. Liu, W. Gan, F. Xu & W.S. Lew. Giant Spin Hall Effect in Cu-Tb Alloy Thin Films. *ACS Applied Materials & Interfaces* (2020).

20 Y. Niimi, Y. Kawanishi, D. Wei, C. Deranlot, H. Yang, M. Chshiev, T. Valet, A. Fert & Y. Otani. Giant spin Hall effect induced by skew scattering from bismuth impurities inside thin film CuBi alloys. *Physical Review Letters* **109**, 156602 (2012).

21 L. Berger. Side-jump mechanism for the Hall effect of ferromagnets. *Physical Review B* **2**, 4559 (1970).

22 R. Ramaswamy, Y. Wang, M. Elyasi, M. Motapothula, T. Venkatesan, X. Qiu & H. Yang. Extrinsic spin Hall effect in Cu 1− x Pt x. *Physical Review Applied* **8**, 024034 (2017).

23 Y. Niimi, M. Morota, D. Wei, C. Deranlot, M. Basletic, A. Hamzic, A. Fert & Y. Otani. Extrinsic spin Hall effect induced by iridium impurities in copper. *Physical Review Letters* **106**, 126601 (2011).

24 M. Gradhand, D.V. Fedorov, P. Zahn & I. Mertig. Extrinsic spin Hall effect from first principles. *Physical Review Letters* **104**, 186403 (2010).

25 N. Nagaosa, J. Sinova, S. Onoda, A.H. MacDonald & N.P. Ong. Anomalous hall effect. *Reviews of Modern Physics* **82**, 1539 (2010).

26 R. Karplus & J. Luttinger. Hall effect in ferromagnetics. *Physical Review* **95**, 1154 (1954).

27 T. Jungwirth, Q. Niu & A. MacDonald. Anomalous Hall effect in ferromagnetic semiconductors. *Physical Review Letters* **88**, 207208 (2002).

28 M. Onoda & N. Nagaosa. Topological nature of anomalous Hall effect in ferromagnets. *Journal of the Physical Society of Japan* **71**, 19-22 (2002).

29 J. Wunderlich, B. Kaestner, J. Sinova & T. Jungwirth. Experimental observation of the spin-Hall effect in a two-dimensional spin-orbit coupled semiconductor system. *Physical Review Letters* **94**, 047204 (2005).

30 J. Sinova, D. Culcer, Q. Niu, N. Sinitsyn, T. Jungwirth & A.H. MacDonald. Universal intrinsic spin Hall effect. *Physical Review Letters* **92**, 126603 (2004).

31 G.-Y. Guo, S. Murakami, T.-W. Chen & N. Nagaosa. Intrinsic spin Hall effect in platinum: First-principles calculations. *Physical Review Letters* **100**, 096401 (2008).

32 T. Tanaka, H. Kontani, M. Naito, T. Naito, D.S. Hirashima, K. Yamada & J. Inoue. Intrinsic spin hall effect and orbital Hall effect in 4 d and 5 d transition metals. *Physical Review B* **77**, 165117 (2008).

33 M.I. Dyakonov & V. Perel. Current-induced spin orientation of electrons in semiconductors. *Physics Letters A* **35**, 459-460 (1971).

34 N.F. Mott. The scattering of fast electrons by atomic nuclei. *Proceedings of the Royal Society of London. Series A, Containing Papers of a Mathematical and Physical Character* **124**, 425-442 (1929).

35 J. Hirsch. Spin hall effect. *Physical Review Letters* **83**, 1834 (1999).

36 S. Zhang. Spin Hall effect in the presence of spin diffusion. *Physical Review Letters* **85**, 393 (2000).

37 A. Fert & P.M. Levy. Spin Hall effect induced by resonant scattering on impurities in metals. *Physical Review Letters* **106**, 157208 (2011).

38 M. Gradhand, D.V. Fedorov, P. Zahn & I. Mertig. Spin Hall angle versus spin diffusion length: Tailored by impurities. *Physical Review B* **81**, 245109 (2010).

39 N.H. Long, P. Mavropoulos, B. Zimmermann, D.S. Bauer, S. Blügel & Y. Mokrousov. Spin relaxation and spin Hall transport in 5 d transition-metal ultrathin films. *Physical Review B* **90**, 064406 (2014).

40 W. Zhang, M.B. Jungfleisch, W. Jiang, J.E. Pearson, A. Hoffmann, F. Freimuth & Y. Mokrousov. Spin Hall effects in metallic antiferromagnets. *Physical Review Letters* **113**, 196602 (2014).

41 J. Smit. The spontaneous Hall effect in ferromagnetics I. *Physica* **21**, 877-887 (1955).

42 J. Smit. The spontaneous Hall effect in ferromagnetics II. *Physica* **24**, 39-51 (1958).

43 L. Berger. Influence of spin-orbit interaction on the transport processes in ferromagnetic nickel alloys, in the presence of a degeneracy of the 3d band. *Physica* **30**, 1141-1159 (1964).

44 E. Myers, D. Ralph, J. Katine, R. Louie & R. Buhrman. Current-induced switching of domains in magnetic multilayer devices. *Science* **285**, 867-870 (1999).

45 J. Katine, F. Albert, R. Buhrman, E. Myers & D. Ralph. Current-driven magnetization reversal and spin-wave excitations in Co/Cu/Co pillars. *Physical Review Letters* **84**, 3149 (2000).

46 S. Mangin, D. Ravelosona, J. Katine, M. Carey, B. Terris & E.E. Fullerton. Current-induced magnetization reversal in nanopillars with perpendicular anisotropy. *Nature Materials* **5**, 210-215 (2006).

47 S.I. Kiselev, J. Sankey, I. Krivorotov, N. Emley, R. Schoelkopf, R. Buhrman & D. Ralph. Microwave oscillations of a nanomagnet driven by a spin-polarized current. *Nature* **425**, 380-383 (2003).

48 W.H. Rippard, M.R. Pufall, S. Kaka, S.E. Russek & T.J. Silva. Direct-current induced dynamics in C o 90 F e 10/N i 80 F e 20 point contacts. *Physical Review Letters* **92**, 027201 (2004).

49 M. Tsoi, A. Jansen, J. Bass, W.-C. Chiang, M. Seck, V. Tsoi & P. Wyder. Excitation of a magnetic multilayer by an electric current. *Physical Review Letters* **80**, 4281 (1998).

50 M. Madami, S. Bonetti, G. Consolo, S. Tacchi, G. Carlotti, G. Gubbiotti, F. Mancoff, M.A. Yar & J. Åkerman. Direct observation of a propagating spin wave induced by spin-transfer torque. *Nature Nanotechnology* **6**, 635-638 (2011).

51 D.C. Ralph & M.D. Stiles. Spin transfer torques. *Journal of Magnetism and Magnetic Materials* **320**, 1190-1216 (2008).

52 A. Brataas, A.D. Kent & H. Ohno. Current-induced torques in magnetic materials. *Nature Materials* **11**, 372-381 (2012).

53 L. Liu, T. Moriyama, D. Ralph & R. Buhrman. Spin-torque ferromagnetic resonance induced by the spin Hall effect. *Physical Review Letters* **106**, 036601 (2011).

54 L. Liu, C.-F. Pai, Y. Li, H. Tseng, D. Ralph & R. Buhrman. Spin-torque switching with the giant spin Hall effect of tantalum. *Science* **336**, 555-558 (2012).

55 C.-F. Pai, L. Liu, Y. Li, H. Tseng, D. Ralph & R. Buhrman. Spin transfer torque devices utilizing the giant spin Hall effect of tungsten. *Applied Physics Letters* **101**, 122404 (2012).

56 I.M. Miron, G. Gaudin, S. Auffret, B. Rodmacq, A. Schuhl, S. Pizzini, J. Vogel & P. Gambardella. Current-driven spin torque induced by the Rashba effect in a ferromagnetic metal layer. *Nature Materials* **9**, 230-234 (2010).

57 I.M. Miron, K. Garello, G. Gaudin, P.-J. Zermatten, M.V. Costache, S. Auffret, S. Bandiera, B. Rodmacq, A. Schuhl & P. Gambardella. Perpendicular switching of a single ferromagnetic layer induced by in-plane current injection. *Nature* **476**, 189-193 (2011).

58 W. Thomson. XIX. On the electro-dynamic qualities of metals:—Effects of magnetization on the electric conductivity of nickel and of iron. *Proceedings of the Royal Society of London*, 546-550 (1857).

59 T. McGuire & R. Potter. Anisotropic magnetoresistance in ferromagnetic 3d alloys. *IEEE Transactions on Magnetics* **11**, 1018-1038 (1975).

60 S. Tumanski. Thin film magnetoresistive sensors. (2001).

61 D. Thompson, L. Romankiw & A. Mayadas. Thin film magnetoresistors in memory, storage, and related applications. *IEEE Transactions on Magnetics* **11**, 1039-1050 (1975).

62 Y.-T. Chen, S. Takahashi, H. Nakayama, M. Althammer, S.T. Goennenwein, E. Saitoh & G.E. Bauer. Theory of spin Hall magnetoresistance. *Physical Review B* **87**, 144411 (2013).

63 H. Nakayama, M. Althammer, Y.-T. Chen, K.-i. Uchida, Y. Kajiwara, D. Kikuchi, T. Ohtani, S. Geprägs, M. Opel & S. Takahashi. Spin Hall magnetoresistance induced by a nonequilibrium proximity effect. *Physical Review Letters* **110**, 206601 (2013).

64 J. Kim, P. Sheng, S. Takahashi, S. Mitani & M. Hayashi. Spin Hall magnetoresistance in metallic bilayers. *Physical Review Letters* **116**, 097201 (2016).

65 G. Binasch, P. Grünberg, F. Saurenbach & W. Zinn. Enhanced magnetoresistance in layered magnetic structures with antiferromagnetic interlayer exchange. *Physical Review B* **39**, 4828 (1989).

66 M.N. Baibich, J.M. Broto, A. Fert, F.N. Van Dau, F. Petroff, P. Etienne, G. Creuzet, A. Friederich & J. Chazelas. Giant magnetoresistance of (001) Fe/(001) Cr magnetic superlattices. *Physical Review Letters* **61**, 2472 (1988).

67 W. Pratt Jr, S.-F. Lee, J. Slaughter, R. Loloee, P. Schroeder & J. Bass. Perpendicular giant magnetoresistances of Ag/Co multilayers. *Physical Review Letters* **66**, 3060 (1991).

68 T. Valet & A. Fert. Theory of the perpendicular magnetoresistance in magnetic multilayers. *Physical Review B* **48**, 7099 (1993).

69 M. Julliere. Tunneling between ferromagnetic films. *Physics Letters A* **54**, 225-226 (1975).

70 T. Miyazaki & N. Tezuka. Giant magnetic tunneling effect in Fe/Al2O3/Fe junction. *Journal of Magnetism and Magnetic Materials* **139**, L231-L234 (1995).

71 J.S. Moodera, L.R. Kinder, T.M. Wong & R. Meservey. Large magnetoresistance at room temperature in ferromagnetic thin film tunnel junctions. *Physical Review Letters* **74**, 3273 (1995).

72 S. Yuasa, T. Nagahama, A. Fukushima, Y. Suzuki & K. Ando. Giant room-temperature magnetoresistance in single-crystal Fe/MgO/Fe magnetic tunnel junctions. *Nature Materials* **3**, 868-871 (2004).

73 S.S. Parkin, C. Kaiser, A. Panchula, P.M. Rice, B. Hughes, M. Samant & S.-H. Yang. Giant tunnelling magnetoresistance at room temperature with MgO (100) tunnel barriers. *Nature Materials* **3**, 862-867 (2004).

Chapter 3 Experimental Techniques

In this chapter, details of the fabrication and characterization techniques employed in this work to study the spin-orbit torque are presented. All thin films used were deposited using magnetron sputtering. Thereafter, lithography is used to pattern the device for electrical measurements. Material properties are characterized with various X-ray spectroscopy techniques to ensure that the film possesses the desired properties and to support our experimental claims. Finally, the ferromagnetic resonance techniques were performed to characterize the spin-orbit torque of the devices.

3.1 Thin Film Deposition

Magnetron sputtering is a physical vapor deposition (PVD) process widely adapted in many industrial processes for thin film growth, due to its reliable uniformity, ease of alloying desired compound and cost-efficiency. As for the working principle, it begins with a large amount of power is supplied between the target (cathode) and the substrate (anode) and the introduction of an inert gas such as Ar into the sputtering chamber. The power applied is typically in the form of negative voltage at the cathode as shown in Figure 3-1(a). Stray electrons at the cathode will then accelerate towards the anode colliding with a neutral gas atom converting it into a positively charged ion. This process will result in two electrons ($e^- + A \rightarrow 2\ e^- + A^+$), which will then collide with other gas atoms and ionizing them creating a cascading process until the gas within the chamber breaks down forming a plasma depicted by the purple glow in the illustration. To further improve the efficiency of the generation of ions, a strong magnetic field is used to confine the plasma near the target such that plasma is stable, and the target bombardment occurs reliably.[1]

The breakdown voltage is dependent on the pressure within the sputtering chamber and the distance between the target and the substrate. Too high a pressure will result in excessive collisions such that the electrons do not have enough time to gain energy from the collision to ionize gas atoms. While too low a pressure will make it difficult to sustain the plasma due to insufficient collision. As such, to maintain the optimal deposition pressure within the chamber, a cryogenic pump is often used. Highly energetic ions will accelerate towards the target and bombard its surface. The collision between the ions and target surface atoms is elastic and the

energy transfer between them knocks off atoms from the target material. These atoms then make their way onto the substrate through diffusion.

The deposition rate can be tuned by varying the power supplied to the target and the sputtering pressure. The magnetron sputtering system developed by AJA was used and an image of the system is as shown in Figure 3-1(b).[2] Since the chamber contains more than one target, it allows for sputtering of alloy material by co-sputtering by supplying power to two or more targets simultaneously. The Pt_xCu_{1-x} alloys used in Chapter 4 were obtained by co-sputtering both Pt and Cu and their atomic composition is varied by adjusting their sputtering power.

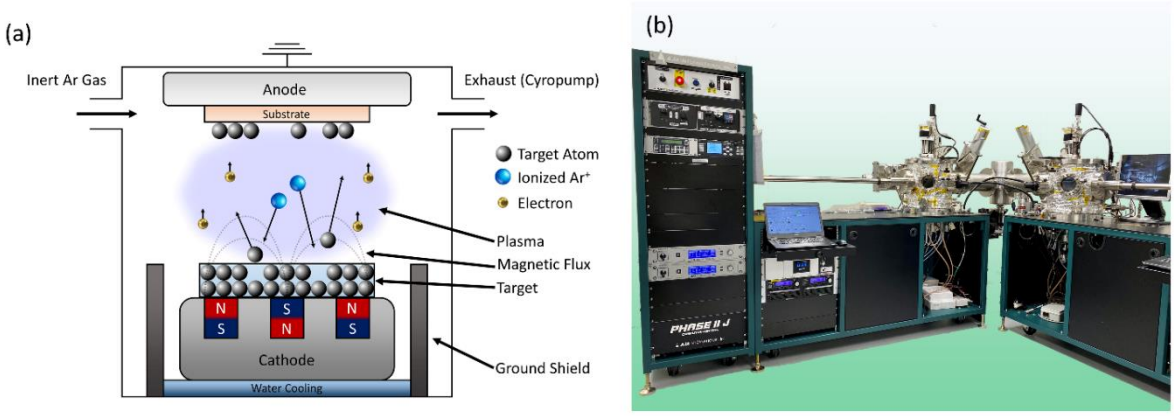

Figure 3-1 (a) Schematic of magnetron sputtering chamber during the deposition process. Ar ions accelerate towards the negatively charged target bombarding the target causing its atoms to be sputtered out and deposited onto the substrate. (b) Image of AJA magnetron sputter system in our Spintronics Laboratory.

3.2 Lithography

Lithography is a technique used to create nanometer range patterns on a thin film or substrate. Typically, it is used with a combination of deposition and etching to deliver high-resolution topography. There are several variants of lithography techniques, however, for this thesis, we will be focusing on the two techniques used which are electron beam lithography (EBL) and ultraviolet (UV) lithography.

Electron beam lithography (EBL) involves the use of an electron beam to react with the chemical resist spin-coated on the sample surface. Depending on the tone of resist used, the solubility of the electron beam exposed areas can either become more or less soluble. The positive and negative resist used in our laboratories is PMMA 950K and MaN 2401 respectively. In Figure 3-2(a), positive tone resist that is exposed to electron beam will become

more soluble and will dissolve when developed while negative tone resist hardens leaving them behind after development. Timing plays a crucial role in resist development to avoid over- or under-development. Development time is calibrated depending on the type of resist used, the thickness of resist, and exposure dose. The thickness of the resist is controlled by varying the ramp and speed of spin-coating the resist. To remove excess solvent from the resist, the samples are baked after spin-coating. After the post-lithography process, the resist is stripped using acetone and IPA before proceeding to the lithography step for the next layer. Exploiting this chemical property of the resist, device patterns can be easily fabricated onto samples by exposing electron beam in the shape of the device.

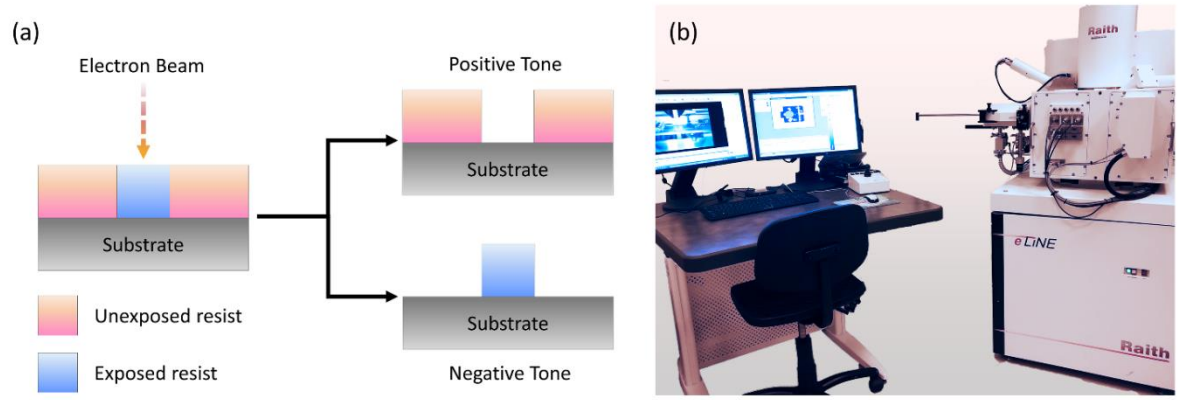

Figure 3-2 (a) Schematic showing the effects of electron beam exposure on positive and negative tone resist after development. (b) Image of Raith eLine EBL system in our Spintronics Laboratory.

The electron beam used is generated using a tungsten filament and accelerated down to the sample stage using an amplifier. These electrons are collimated and centered using an aperture lens and to beam different areas of the sample, the electron beam is deflected using a magnetic field generated by the deflector coil. However, there is a limit to how far the beam can be deflected, and the surface area at which the beam is able to strike is known as the write field of the electron beam. On top of aligning the pattern mask drawing to the substrate, the write field alignment of the beam is equally important as failure to do so will result in disconnected patterns as the region between the write fields is not exposed properly. Two major advantages of the EBL are the high-resolution point by point exposure as electron beams are affected by the diffraction limit of light and that it does not require a physical mask for the exposure. It can take place with just drawn patterns on the system computer and this helps save time during the initial designing phase of the samples. An image of the Raith eLine EBL system used in this thesis can be found in Figure 3-2(b).[3]

For the ease of lithography alignment on a transparent flexible substrate, devices fabricated in Chapters 5 and 6, UV lithography is used. UV lithography, also known as optical lithography, is the other type of lithography technique used in this thesis. Its working principle is similar to that of the EBL, except instead of using an electron beam, it uses UV light to change the solubility of the resist. The control of the area exposed to the UV light is controlled using a chrome mask. Since the UV light used for exposure comes from a UV lamp, UV lithography can expose the entire mask simultaneously. This leads to a much shorter exposure time for UV lithography is much shorter as compared to EBL. The positive and negative UV resist used in our laboratories are AZ5214E and SU-8 respectively. For all devices used in this thesis, a two-step positive tone lithography is used. The first step is used to create an opening to deposit the device structure and the second is for the deposition of the coplanar waveguide (CPW).

3.3 X-Ray Diffraction

X-ray Diffraction (XRD) is a method commonly used to determine the crystallinity of a material. In an XRD experiment, a sample is placed into the center of the instrument and illuminated with a beam of X-ray as shown in Figure 3-3(a). The X-ray beam used is typically generated using a W filament and in order to ensure that the X-ray beam is a single wavelength, the X-ray radiation is filtered through a Ge(220) 2 bounce monochromator which only allows $K\alpha_1$ radiation with a wavelength of 1.405 nm pass through.

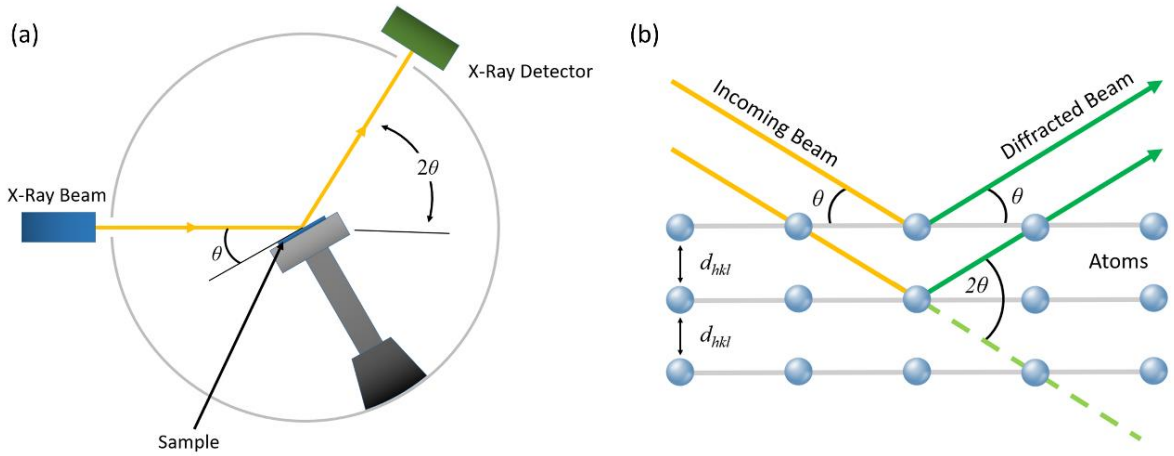

Figure 3-3 (a) Schematic of XRD setup with X-ray beam source and detector moving in a synchronized motion. (b) Illustration of X-ray beam reflecting off the sample creating a constructive interference.

During measurement, the X-ray beam and detector move in a synchronized motion. The signal coming from the sample is recorded and graphed. Since the X-ray beam used does not have enough energy to cause the electrons in the sample to be released, the energy is re-emitted in the form of a new x-ray with the same energy as the original through elastic scattering. Depending on the geometry of the incident X-ray interacting with the sample, constructive interference can be observed as an amplified peak on the XRD spectrum. The angles at which these constructive interferences occur are determined by Bragg's equation expressed by the following,

$$n\lambda = 2d\sin\theta \tag{3.3.1}$$

where θ is the angle between the diffraction plane and the X-ray beam, n is an integer representing the order of diffraction, and λ is the wavelength of the X-ray beam.[4-6] As shown in Figure 3-3(b), diffracted X-ray beams that are in-phase with one another result in constructive interferences and an amplified peak signal is detected. The position of these amplified peaks provides atomic structure information of the material.

3.4 X-Ray Reflectometry

X-ray reflectivity (XRR) is surface sensitive technique to analyze the surface and interfaces of thin films. The basic principle behind XRR is similar to that of the XRD with the exception of the incident angle of the X-ray beam. Typically, the grazing angle of the X-ray beam is set to 0° to 8°. A beam of X-ray is projected from an X-ray source and onto a flat

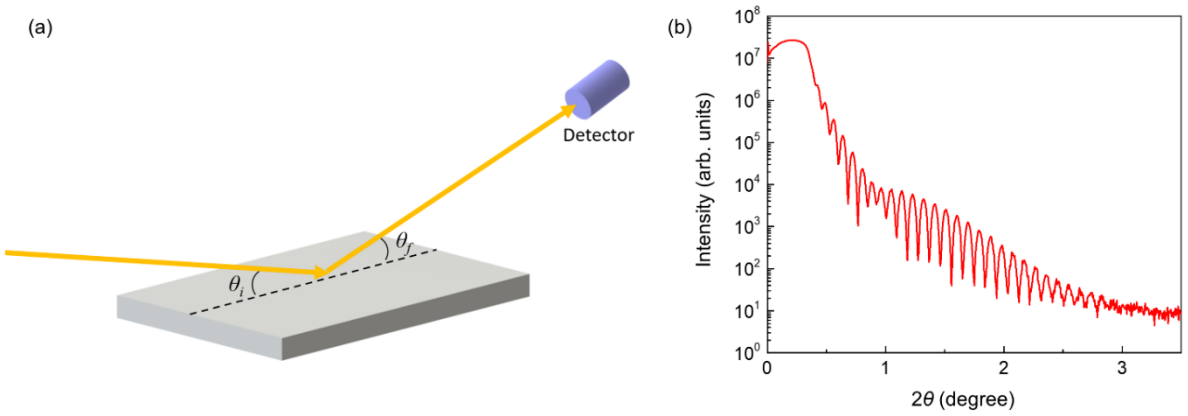

Figure 3-4 (a) Schematic of X-ray beam reflecting off a sample and into the detector. (b) XRR spectrum of CoFeB (50nm) thin film.

surface of the sample and the intensity of the reflected X-ray is measured as shown in Figure 3-4(a). The critical angle, θ_C, of the X-ray provides information about the density of the thin film and can be expressed by this relation, $\theta_C \sim \sqrt{\rho}$ where ρ is the density of the film. The thickness of the measured film can be obtained by fitting the oscillation spacing of the spectra and the roughness of the film is determined by the damping constant of the oscillation and the curvature of the spectra.[7-11] In Figure 3-4(b), since the alloy CoFeB film contains more than one element, multiple oscillations of different frequencies can be observed in the spectra.

3.5 Energy-Dispersive X-Ray Spectroscopy

Energy-dispersive X-ray spectroscopy (EDX) is an analytical technique used to determine the elemental compositions within a sample. It involves the use of an electron beam to excite the atoms within the sample. This interaction between the electron beam and the atom causes an electron from the inner orbitals to be ejected out leaving behind a void as shown in Figure 3-5. An X-ray radiation is emitted when an electron from a higher energy level fills this void. Using an X-ray detector, the energy of the X-ray radiation is converted into voltage and qualified. Moseley's law states that the electromagnetic emission spectrum of each element is different due to their unique atomic structure and using this relation, the emission peaks of the different elements can be predicted.

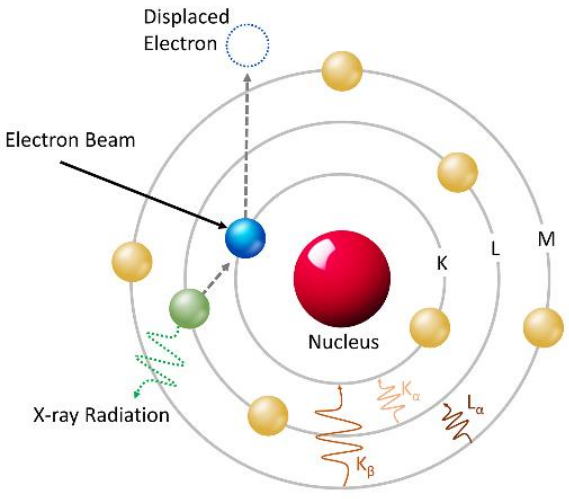

Figure 3-5 Schematic of interaction between an electron beam and the core electron of an atom resulting in an X-ray radiation emission.

3.6 X-Ray Magnetic Circular Dichroism

The term "dichroism", in the field of optics, refers to the change in absorption of polarized light when passing through the material in two different directions. Since materials usually absorb one color of white light, the material appears with two different colors for the two light directions. The origin of the dichroism effect can be attributed to the anisotropies in the charges or spin in the material and X-ray magnetic circular dichroism (XMCD) exploits the latter to study ferromagnetic thin films.

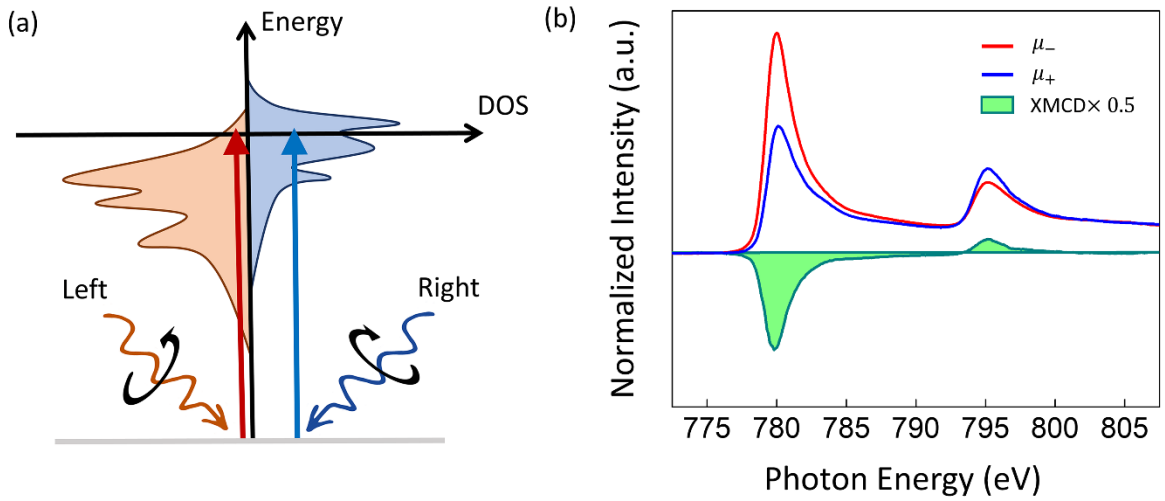

Figure 3-6 (a) Illustration of the working principle of XMCD. (b) Normalized XAS/XMCD spectra of Pt (5 nm)/Co (5 nm).

X-ray absorption spectroscopy (XAS) uses the energy dependence of X-ray absorption in materials to determine the elemental composition of the sample. Core electrons in the atom are excited in the absorption process onto valance states above the Fermi energy level and this allows information about the empty valence levels to be obtained. For magnetic 3*d* transition metal elements, such as Fe, Co, and Ni, their magnetic properties are largely attributed to the 3*d* valence electrons. Due to the dipole selection rules that determine the X-ray absorption spectra, the *d*-shell properties in these 3*d* transition metal elements are ideal for *L*-edge absorption studies. The *L*-edge X-ray absorption spectra of these metals have two distinct peaks as shown in Figure 3-6(b). The two peaks are derived from the spin-orbit interaction of the 2*p* core shell and the total intensity of the peaks is proportional to the number of empty 3*d* valence states.

The first X-ray absorption sum rule relates the total intensity of the L_3 and L_2 resonance with the number N of empty d states also known as "holes". Since the d valence shell is capable

of holding up to 10 electrons filled into the band states up to the Fermi level, the number of filled states is N-10. For a magnetic material, the *d* shell has a spin moment that gives rise to an imbalance of spin-up and spin-down electrons or holes. This provides an opportunity to utilize the spin-dependent characteristic of the X-ray absorption process to measure the difference in the number of *d* holes with the spin-up and spin-down. The spin dependence X-ray absorption process is achieved by polarizing emitted the X-ray in the right and left circular direction which then transfers their angular momentum to the excited photoelectron as shown in Figure 3-6(b).

The photoelectron carries the transferred angular momentum as a spin or an angular momentum, or both. If the photoelectron comes from a spin-orbit split level, the angular momentum of the photo can be transferred in part to the spin through the spin-orbit coupling. Both the right and left circular photons transfer momentum to the electrons in the opposite direction and this causes the two photoelectrons of a different spin to be generated. Since the L_3 and L_2 levels have opposite spin-orbit coupling, the spin polarization at the two edges will be opposite in direction. The direction of the spins in the absorption process is with respect to the photon helicity or photon spin.

The spin-up and spin-down photoelectrons from the *p* core shell can only be excited into the respective spin-up and spin-down *d* hole state as spin flipping are forbidden in the electric dipole transitions. Therefore, the spin split valence shell acts as a detector for the excited photoelectron and the intensity of the transition is proportional to the number of empty *d* states of a given spin. The magnetization direction determines the quantization axis of the valence shell "detector" and the magnitude of the dichroism effect can be adjusted by varying angle the between the photon spin and the magnetization direction. The intensity of L_3 and L_2, the differences in orientation of photon spin, and magnetization directions are quantitatively linked to the number of *d* holes and the size of the spin and orbital magnetic moments by sum rules. More details regarding the XMCD can be found in the discussion of Chapter 5 where it is applied and used to support the experiment.

3.7 Vibrating Sample Magnetometer

Vibrating Sample Magnetometer (VSM) is a characterization tool widely used in the spintronics community to probe the magnetization of a sample. The operation principle of the VSM capitalizes on Faraday's law of induction. When the magnetic sample vibrates, its magnetic flux changes. From Figure 3-7(a), the placement of the magnetic sample is at the center of the two electromagnet and pickup coils. The sample is mounted onto a non-magnetic rod, usually made of glass, and attached to the vibrating head that provides the vibration for the sample. The magnitude of the magnetic flux measured by the pickup coil can be described by the following expression,

$$\phi_B = \mu_0 A(H + M) \tag{3.7.2}$$

where μ_0 is the magnetic permeability, A is the surface area of the pickup coil, H is the applied magnetic field and M is the magnetization of the sample. Since there is a change in magnetic flux, an electromagnetic force (EMF) is induced and detected as a voltage by the pickup coil. This voltage can be expressed as

$$\varepsilon = -N\frac{d\Phi_B}{dt} \tag{3.7.3}$$

where N is the number of turns in the pickup coils and $\frac{d\Phi_B}{dt}$ is the change in magnetic flux. By measuring the induced voltage, the flux from the magnetization of the sample can be easily determined.

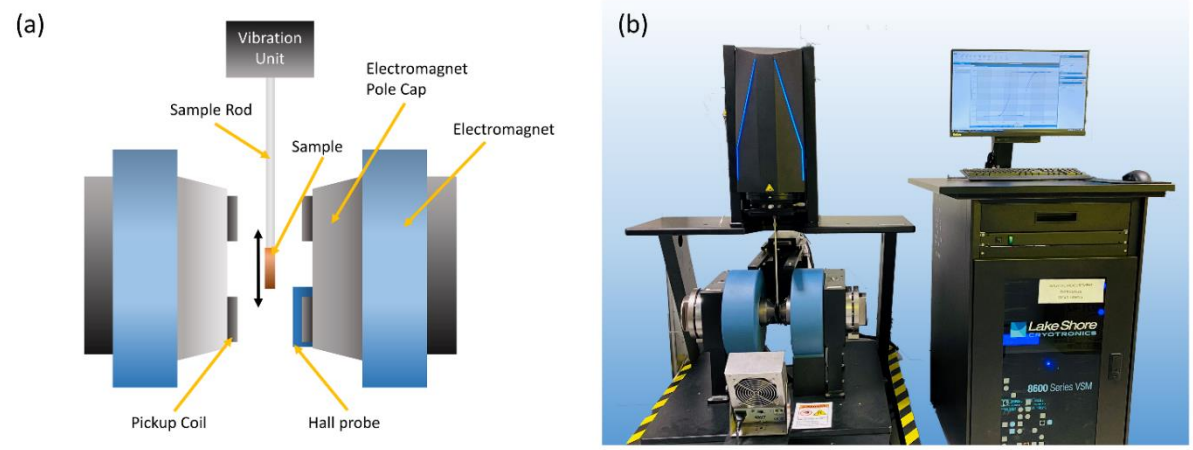

Figure 3-7 (a) Schematic diagram illustrating the setup of the VSM. (b) Image of Lakeshore 8600 VSM system.

The rate of the change in magnetic flux is determined by the frequency of the vibrating sample and is controlled by the vibration control unit of the VSM. The voltage from the pickup coil is usually detected by a lock-in amplifier using the frequency of the vibration as a reference. As such, the accuracy of the magnetic signal detected by the VSM can be as small as 10^{-9} emu. The VSM system used in this thesis is Lakeshore 8600 as shown in Figure 3-7(b).[12]

3.8 Spin-Torque Ferromagnetic Resonance

Developed by Liu et al. in 2011, the spin-torque ferromagnetic resonance (ST-FMR) technique has revolutionized the study of spin-orbit torque in materials.[13] Due to the ease of use and versatility, the technique has been widely implemented since its discovery.[14-23] Figure 3-8 shows the ST-FMR system that was set up and is currently utilized in our laboratory. This measurement system doubles up as both an ST-FMR and FMR characterization tool and can be toggled between the two configuration modes. Before we dive into the process of setting up the tool, let us look at the working principles.

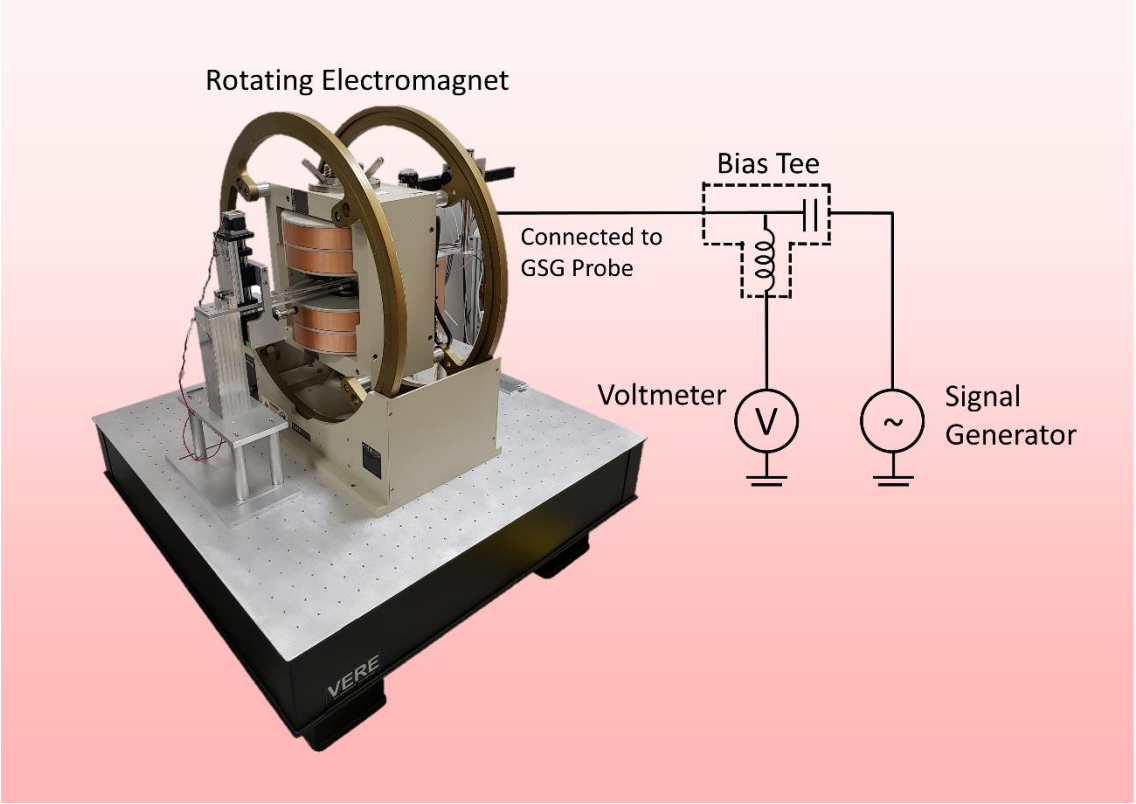

Figure 3-8 Photo of spin-torque ferromagnetic resonance (ST-FMR) setup in our spintronics laboratory.

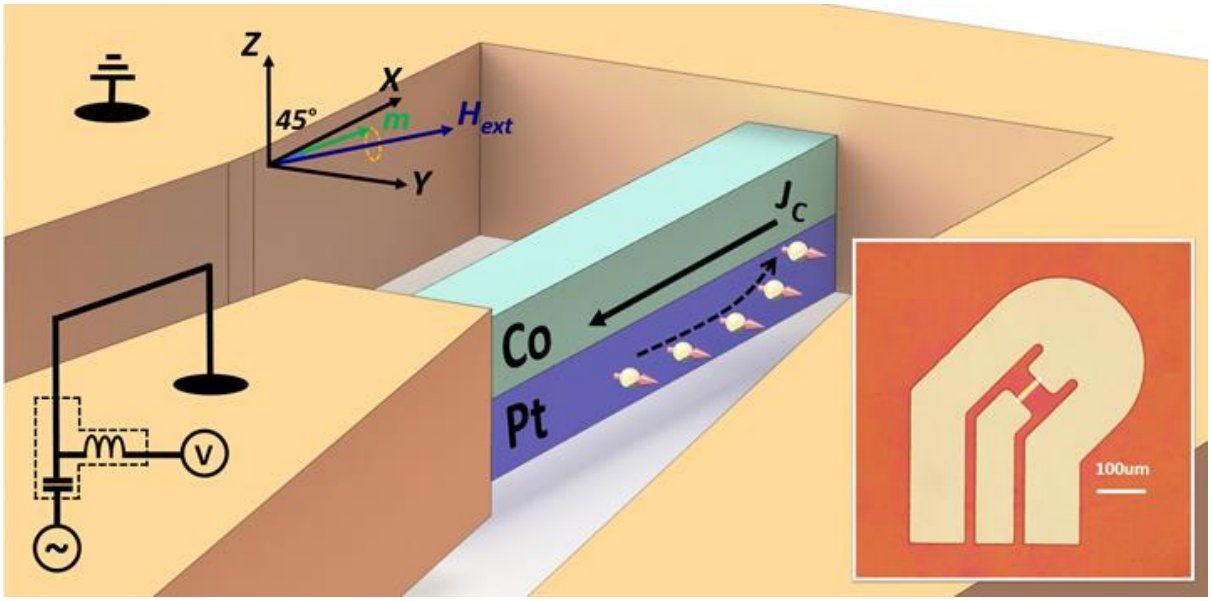

Figure 3-9 Photo of spin-torque ferromagnetic resonance (ST-FMR) setup in Spintronics laboratory. Schematic of a bilayer HM/FM heterostructure during ST-FMR measurement. Inset: Optical image of an ST-FMR device.

The ST-FMR measurement technique involves the application of an external magnetic field H_{ext} at an angle θ to the applied radio frequency (RF) current through the coplanar waveguide (CPW) and into microstrip device as shown in Figure 3-9.[16,24] By sweeping H_{ext} and varying the current frequency, the measured DC voltage response provides information about the spin Hall efficiency, Gilbert damping constant, and effective magnetization field.

The longitudinal RF current passing through the heavy metal layer (HM) generates an oscillating transverse spin current by spin Hall effect (SHE), which is then injected into the adjacent ferromagnetic layer (FM). The magnetization of the FM experiences three different torques induced by the RF current: Oersted-field torque as current passes through the FM, field-like and damping-like torque produced by the current-induced SOT from the HM. At the resonance field H_{res} when the microwave frequency matches the precessional frequency of the magnetization, the FMR condition is satisfied, and the oscillating torques will result in the oscillation of the device resistance due to anisotropic magnetoresistance in the FM. The mixing of the RF current and oscillating resistance results in a rectified DC voltage signal V_{mix} across the device as shown in Figure 3-10.[25] Using a bias tee, V_{mix} can be measured during the microwave current application.

The measured rectified voltage V_{mix} is then fitted to two Lorentzian which can be expressed as the following,

$$V_{\mathrm{mix}} = S\frac{(\Delta H/2)^2}{(H_{\mathrm{ext}}-H_{\mathrm{res}})^2+(\Delta H/2)^2} + A\frac{(H_{\mathrm{ext}}-H_{\mathrm{res}})(\Delta H/2)}{(H_{\mathrm{ext}}-H_{\mathrm{res}})^2+(\Delta H/2)^2}, \tag{3.8.4}$$

where ΔH is the linewidth and S and A are magnitude the symmetric and anti-symmetric components of the V_{mix} respectively.[13] The symmetric Lorentzian contribution is produced when the spin Hall torque from the generated spin current and the magnetization precession are in phase, while the antisymmetric is the result of the sum of the Oersted field and the field-like torque.

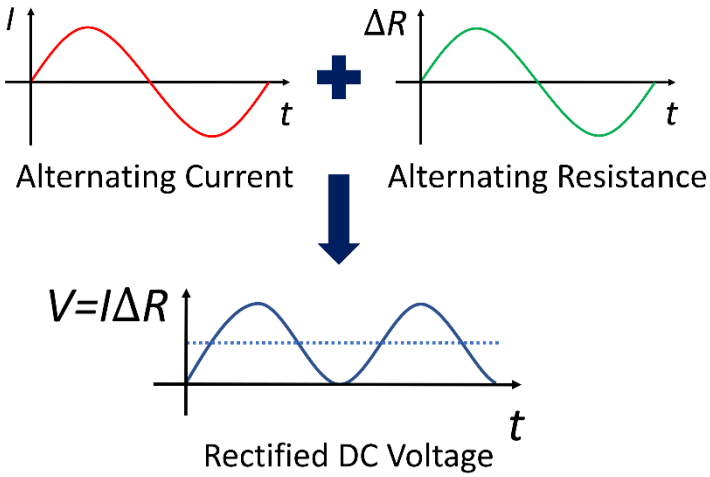

Figure 3-10 Illustration explaining the principle of the ST-FMR.

The Lorentzian contribution arises from the phase difference between the Oersted field and the field-like torque from the charge current passing through the HM and the magnetization precession. The S and A contribution is described by the following relation,

$$S = V_0\frac{\hbar J_{\mathrm{s}}}{2e\mu_0 M_{\mathrm{s}} t}, \qquad A = V_0(H_{\mathrm{rf}}+H_{\mathrm{FL}})\sqrt{1+\frac{4\pi M_{\mathrm{eff}}}{H_{\mathrm{ext}}}}. \tag{3.8.5}$$

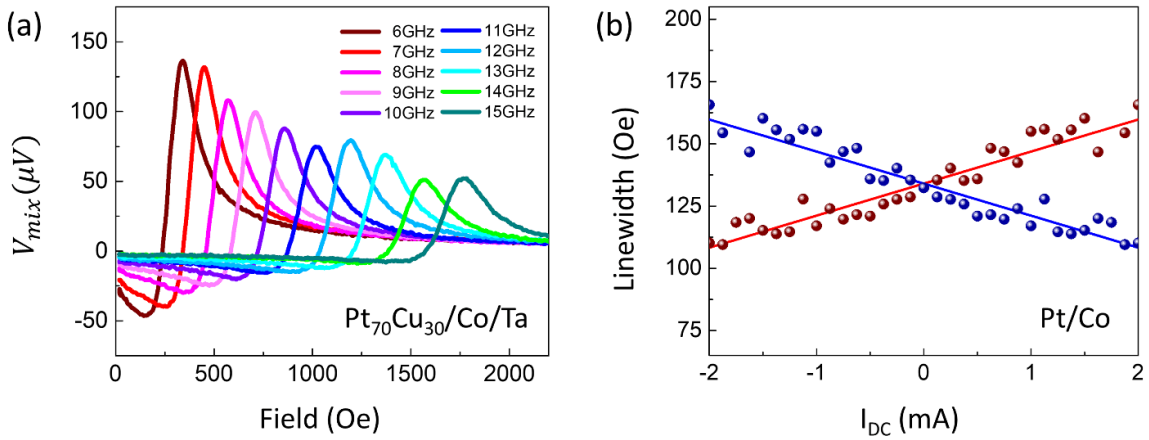

Figure 3-11 (a) Measured ST-FMR spectra of $Pt_{60}Cu_{40}$ (5 nm)/Co (5 nm)/Ta (5 nm) trilayer for frequency from 6 to 15 GHz with nominal input power of 18 dBm. (b) Linewidth dependence on the DC biased for Pt (5 nm)/Co (5 nm) at 12 GHz.

where V_0 is a constant, J_s is the spin current density, $\mu_0 = 4\pi \times 10^{-7}\ \mathrm{Hm}^{-1}$ is the magnetic permeability in free space, t is the thickness of the ferromagnetic (FM) layer, M_s is the saturation magnetization of the FM layer, M_{eff} is the effective magnetization, H_{Oe} is the Oersted field and H_{FL} is the effective field generated by field-like torque. An example of the V_{mix} spectra of $Pt_{60}Cu_{40}$ (5 nm)/Co (5 nm)/Ta (5 nm) measured between frequencies 6 to 15 GHz is as shown in Figure 3-11(a). The effective magnetization M_{eff} can be obtained by an in-plane magnetization Kittel equation fitting,

$$f = \gamma/2\pi \sqrt{\left(H_{\mathrm{res}} + H_{\mathrm{K}}\right)\left(4\pi M_{\mathrm{eff}} + H_{\mathrm{res}} + H_{\mathrm{K}}\right)}\,, \tag{3.8.6}$$

where γ is the gyromagnetic ratio and H_{K} is the total magnetic anisotropy field.[26] The Gilbert damping constant can be acquired by using a linear fitting of the linewidth dependence of microwave frequency given by,

$$\Delta H = \Delta H_0 + \frac{2\pi f \alpha_{\mathrm{eff}}}{\gamma}, \tag{3.8.7}$$

where ΔH_0 is the inhomogeneous broadening term originating from sample imperfections which are assumed to be frequency independent.[27,28] The existence of two-magnon scattering can be identified by the linear dependence of the FMR linewidth with frequency and is often

assumed to be absent if Equation 3.8.7 has a good linear fit.

One of the most used methods to determine the spin Hall efficiency of the measured sample is the use of the line-shape method.[13,29-37] Since the *S* component is proportional to the strength of the damping-like torque and *A* component is proportional to the Oersted field generated by the RF current, the spin Hall efficiency can be determined by taking the ratio between the *S* and *A* component using the following expression,

$$\theta_{\text{eff}} = \frac{S}{A}\frac{e\mu_0 M_S t_{\text{FM}} t_{\text{NM}}}{\hbar}\sqrt{1+\frac{4\pi M_{\text{eff}}}{H_{\text{res}}}}, \tag{3.8.8}$$

where t_{NM} is the thickness of HM.[18,38-44] The complexity of the ST-FMR devices is relatively easy to fabricate as compared to other SOT characterization methods such as nonlocal spin-value (NLSV).[45-49] ST-FMR is also a self-calibrated technique as most parameters required for the calculation of the spin Hall efficiency, except the M_S and thickness of the film, are obtained through the ST-FMR measurement itself. As such, the simplicity of the line-shape method has made this method a popular choice of technique to characterize the spin-orbit torque.

Not long after the breakthrough of the ST-FMR technique, a missing factor of the line-shape method was discovered. The field-like torque was not taken into account when determining the spin Hall efficiency giving rise to larger than expected values as now both the damping-like and the field-like torque contributes to the V_{mix}.[15,43,44,50-52] This crippled the line-shape method limiting its use to only materials with negligible field-like torque unless a correction was made. A correction was eventually made by varying the thickness of the HM or FM using the following expression,

$$\frac{1}{\theta_{\text{eff}}} = \frac{1}{\zeta_{\text{DL}}}\left(1+\frac{\hbar}{e}\frac{\zeta_{\text{FL}}}{4\pi M_S t_{\text{FM}} d_{\text{NM}}}\right) \tag{3.8.9}$$

where ζ_{DL} and ζ_{FL} are the damping-like and field-like torque respectively.[14,15,53-57] An ideal approach to avoid variation in multiple film growth is the use of wedge sputter deposition by not rotating the sample during deposition. This method allows for the fabrication of samples with multiple thicknesses easing the characterization process.

The next approach to determine the spin Hall efficiency of the sample is the use of the linewidth method.[40,58-63] This method uses an external DC bias to induce damping-like torque on the ST-FMR linewidth. Equation 3.8.7 can be modified to the following,

$$\Delta H = \Delta H_0 + \frac{2\pi f}{\gamma}\left(\alpha_{\text{eff}} + \zeta_{\text{DL}}\frac{\hbar}{e\mu_0 M_{\text{S}}}\frac{\sin\theta}{t_{\text{FM}}(2H_{\text{res}} + M_{\text{eff}})}J_{\text{SH,dc}}\right), \tag{3.8.10}$$

where $J_{\text{SH,dc}}$ is the current density of the DC bias through the HM. By performing a linear equation fit for the linewidth dependence of DC bias, the ζ_{DL} can be easily extracted as shown in Figure 3-11(b).[13,64] That said, the linewidth method is not without its drawbacks. Calculation of the $J_{\text{SH,dc}}$ requires additional experiment to correctly determine the thickness and electrical conductivity of both the FM and HM. The noise in V_{mix} can make it difficult to observe substantial change if the ST-FMR system is not microwave engineered properly limiting this method to only materials that exhibit large spin Hall efficiency. Therefore, to avoid the above obstacles, the line-shape method will be used throughout this thesis with correction and supporting evidence to show that field-like torque is negligible, and that the method used is appropriate for the material being characterized.

This ST-FMR measurement tool was built and pieced together using parts purchased separately for the purpose of being able to perform both ST-FMR and FMR characterization. Beginning from the base of the setup, the isolation platform is a custom-made passive isolation table pressurized by compressed air to counteract any potential vibration from the surrounding.[65] Special request was also made for the isolation platform to be sturdy enough to accommodate the 500 kg rotating magnet that will be placed on it. The electromagnet chose was a rotating magnet from GMW.[66] The magnet is able to rotate freely in the out-of-plane axis of the sample by turning the circular ring that encompasses the magnet with the aid of bearings at the pivot point of the base platform as shown in Figure 3-8. For safety, the rotating ring is equipped with a lock to secure the magnet at a specified angle. The purpose of this rotating magnet is so that a uniform field can be achieved when characterizing both in-plane and out-of-plane samples. An aluminum bridge in between the two magnet poles caps is used as a platform for the sample and the pillars of the bridge are secured down onto the breadboard of

the isolation base. The bridge was designed using Solidworks and sent for milling.

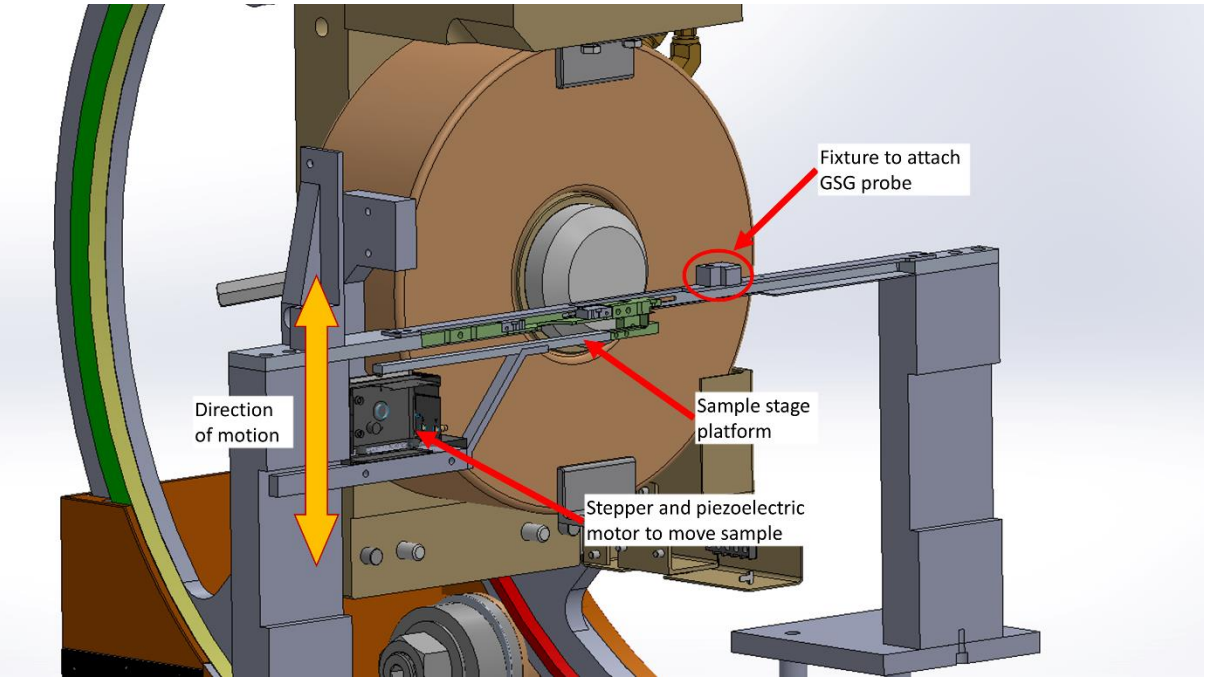

Figure 3-12 Cross-sectional view of prototype design of the ST-FMR measurement system with the initial idea of having a stepper motor to automate the loading and unloading of the sample.

The initial design of the ST-FMR system was for the sample loading and unloading process to be automated for the characterization system. Upon placing the sample onto the sample arm of the system, a coarse stepper motor will be used to bring the sample up and load it near the ground-signal-ground (GSG) probe. Thereafter a piezoelectric motor will do fine adjustments such that the desired device aligns and contacts the probe for measurement. A cross-sectional view of the prototype design can be seen in Figure 3-12. The yellow double arrow denotes the sample loading and unloading motion of the sample stage. The moment of the stage was programmed and controlled using LabVIEW. Besides convenience from the automated loading and unloading, this initial prototype design was planned to be able to run both ST-FMR and FMR measurement on the same stage without making any major change to the setup. The GSG probe was attached to a slider which allowed us to switch to the CPW needed for FMR measurement.

However, soon after assembling all the fixtures, we were faced with a cantilever effect at the sample stage platform. Even with the arm support below the stage platform, we notice that the vibration from the cantilever effect drowning the ST-FMR signal. In order to move forward with our research and avoid the problem, we decided to remove the automated loading and unloading feature and load the sample manually onto the bridge instead of the stage arm. This remedied the problem faced and next we were faced with another issue which was the space constraint above the sample stage for the microscope. There was not enough clearance between the magnet and the intended position of the microscope camera as most commercially available cameras could not fit. This led us to us customizing the microscope such that it fits. Several ideas came by but the idea that worked was the use of drawer runners. The microscope will be attached to a drawer runner and when it is needed, it can be easily slid to the sample for use as shown in Figure 3-13. The RF current is generated using Keysight N5183B analog signal generator and attached to a bias-tee from Picosecond Pulse Labs.[67,68] The GSG picoprobes are customized probes ordered from GGB Industries Inc and they have a standard pitch width of 100 µm with a P-style adaptor.[69] As for the detection of the ST-FMR rectified voltage, we initially used a Keithley 2000 Series voltmeter. However, over time the setup was improved and the voltmeter was swapped to a lock-in amplifier from Zurich Instruments.[70] The measurement is controlled using a LabVIEW program that sweeps the external magnetic field and iterating the RF frequency at the designated step size. As such, the ST-FMR characterization system is completed.

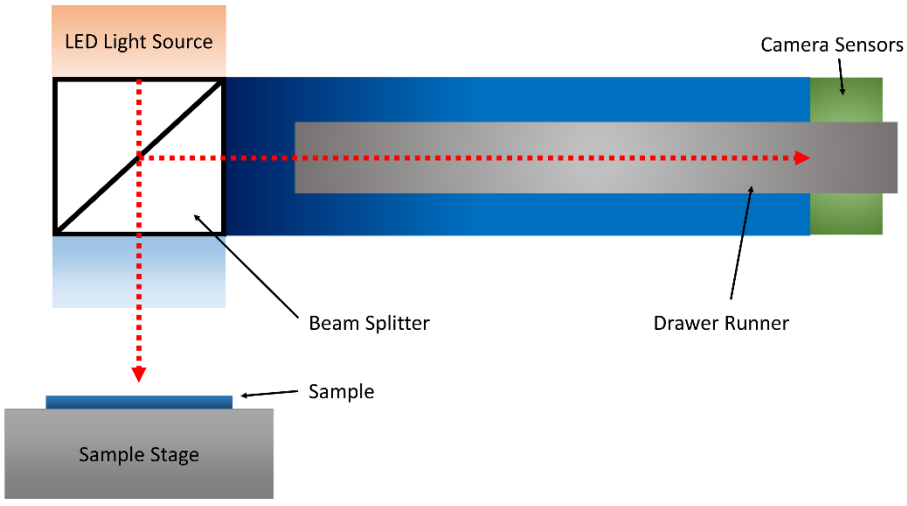

Figure 3-13 Cross-sectional view of the customized microscope. The drawer runner allows the microscope to slide in and out of the magnet such that it does not affect the measurement as the microscope contained magnetic parts.

3.9 Ferromagnetic Resonance Spectroscopy

Ferromagnetic resonance (FMR) is a measurement technique similar to that of the ST-FMR. Both techniques capitalize on the resonance phenomena of the magnetization to probe the magnetic properties.[26] However, several differences between the two techniques set them apart. One of which is the way the microwave current interacts with the sample. For the case of the FMR, RF current is injected through a coplanar waveguide (CPW) instead of directly into the sample.[71,72] The CPW then generates an alternating Oersted field to excite the magnetization of the sample to resonance as shown in Figure 3-14(a).

The next difference is in the way resonance is detected. For resonance to occur, the frequency of the alternating Oersted field from the CPW must match and couple with the precessional frequency of the magnetization of the sample. Once the FMR condition is met, an absorption peak, as shown in Figure 3-14(b), in the transmitted microwave current will be detected by the vector network analyzer. The phase difference between each magnetic moment is zero during FMR which means that FMR is a standing wave with a wavelength of infinity. Another obvious difference is that the sample need not be a patterned device as the FMR setup already has a CPW for the propagation of the microwave current. FMR is a quick way to probe the magnetization of the sample to determine its Gilbert damping and effective magnetization. However, since the current does not pass through the sample, SOT characterization like the ST-FMR is not possible using FMR.

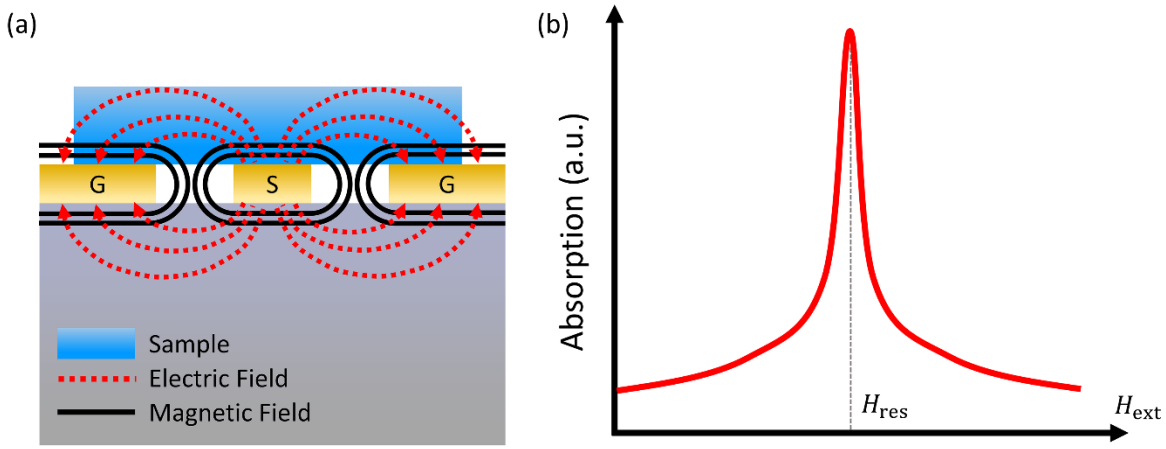

Figure 3-14 (a) Cross-sectional illustration of the coplanar waveguide (CPW) with the sample placed at the top facing downwards. (b) Absorption spectrum of the FMR during a field sweep measurement.

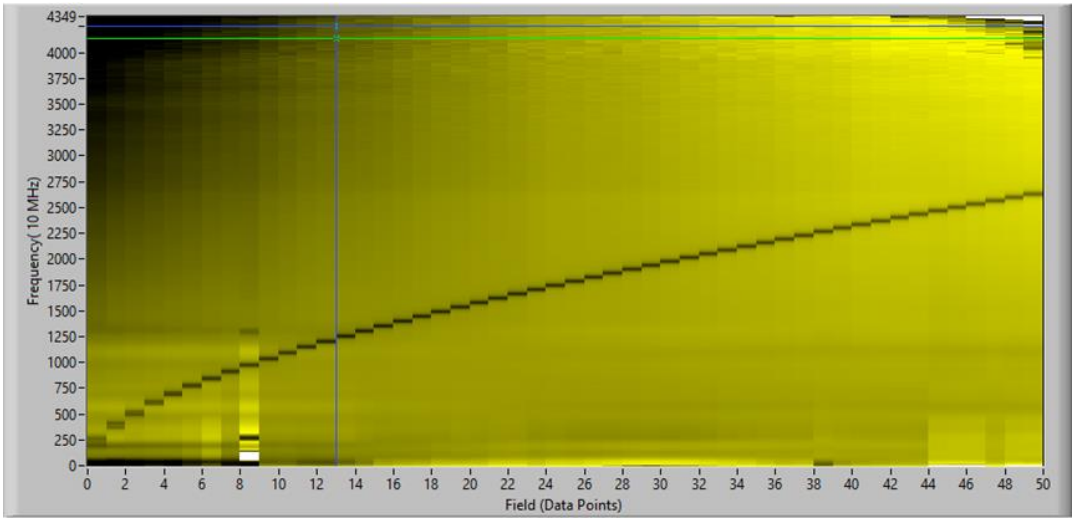

Figure 3-15 Contour plot using LabVIEW program to extract absorption peak. The *x*-axis represents the raw data measured at each iteration of the applied external magnetic field. The black line shows the absorption of the microwave. The blue and green lines denote the cursor to select specific field file and frequency region.

Without the automated loading and unloading design from the prototype setup, the FMR and ST-FMR measurement system require a slight change in the setup configuration before use. The most important change would be to remove the GSG probes and replacing them with an FMR CPW. The CPW is faced up as shown in Figure 3-14 and so the measured sample has to be place upside down. This alteration was surprisingly convenient as the user simply needs to land the sample onto the CPW. There was no need for any alignment as long as the sample makes contact with the CPW facing down. To extract the FMR absorption peaks, a LabVIEW program is used to do a contour plot and from there the resonance peaks can be visually spotted and identified as shown in Figure 3-15.

Reference

1 J.A. Thornton. Influence of apparatus geometry and deposition conditions on the structure and topography of thick sputtered coatings. *Journal of Vacuum Science and Technology* **11**, 666-670 (1974).

2 *AJA International ATC Orion Series Sputtering Systems*, https://www.ajaint.com/atc-orion-series-sputtering-systems.html.

3 *Raith eLine*, https://www.raith.com/product/eline-plus/.

4 G. Fujinawa, H. Toraya & J.-L. Staudenmann. Parallel-slit analyzer developed for the purpose of lowering tails of diffraction profiles. *Journal of Applied Crystallography* **32**, 1145-1151 (1999).

5 M. Roberts & C. Tang. Angular resolution of parallel foils on a synchrotron powder diffractometer. *Journal of Synchrotron Radiation* **5**, 1270-1274 (1998).

6 J.I. Langford & A. Wilson. Scherrer after sixty years: a survey and some new results in the determination of crystallite size. *Journal of Applied Crystallography* **11**, 102-113 (1978).

7 H. Kiessig. Interferenz von Röntgenstrahlen an dünnen Schichten. *Annalen der Physik* **402**, 769-788 (1931).

8 L. Nevot & P. Croce. Caractérisation des surfaces par réflexion rasante de rayons X. Application à l'étude du polissage de quelques verres silicates. *Revue de Physique Appliquée* **15**, 761-779 (1980).

9 S. Sinha, E. Sirota, Garoff & H. Stanley. X-ray and neutron scattering from rough surfaces. *Physical Review B* **38**, 2297 (1988).

10 A. Braslau, M. Deutsch, P.S. Pershan, A. Weiss, J. Als-Nielsen & J. Bohr. Surface roughness of water measured by x-ray reflectivity. *Physical Review Letters* **54**, 114 (1985).

11 L.G. Parratt. Surface studies of solids by total reflection of X-rays. *Physical Review* **95**, 359 (1954).

12 *Lake Shore 8600 Series VSM*, https://www.lakeshore.com/products/categories/overview/material-characterization-products/vsm-systems/8600-series-vsm.

13 L. Liu, T. Moriyama, D. Ralph & R. Buhrman. Spin-torque ferromagnetic resonance induced by the spin Hall effect. *Physical Review Letters* **106**, 036601 (2011).

14 H. An, S. Haku, Y. Kanno, H. Nakayama, H. Maki, J. Shi & K. Ando. Manipulation of Spin-Torque Generation Using Ultrathin Au. *Physical Review Applied* **9**, 064016 (2018).

15 S. Haku, A. Musha, T. Gao & K. Ando. Role of interfacial oxidation in the generation of spin-orbit torques. *Physical Review B* **102**, 024405 (2020).

16 Y. Wang, P. Deorani, X. Qiu, J.H. Kwon & H. Yang. Determination of intrinsic spin Hall angle in Pt. *Applied Physics Letters* **105**, 152412 (2014).

17 L. Liu, C.-F. Pai, Y. Li, H. Tseng, D. Ralph & R. Buhrman. Spin-torque switching with the giant spin Hall effect of tantalum. *Science* **336**, 555-558 (2012).

18 C.-F. Pai, Y. Ou, L.H. Vilela-Leão, D. Ralph & R. Buhrman. Dependence of the efficiency of spin Hall torque on the transparency of Pt/ferromagnetic layer interfaces. *Physical Review B* **92**, 064426 (2015).

19 Y. Wang, P. Deorani, K. Banerjee, N. Koirala, M. Brahlek, S. Oh & H. Yang. Topological surface states originated spin-orbit torques in Bi 2 Se 3. *Physical Review Letters* **114**, 257202 (2015).

20 Y. Wang, D. Zhu, Y. Wu, Y. Yang, J. Yu, R. Ramaswamy, R. Mishra, S. Shi, M. Elyasi & K.-L. Teo. Room temperature magnetization switching in topological insulator-ferromagnet heterostructures by spin-orbit torques. *Nature Communications* **8**, 1-6 (2017).

21 Y. Wang, R. Ramaswamy & H. Yang. FMR-related phenomena in spintronic devices. *Journal of Physics D: Applied Physics* **51**, 273002 (2018).

22 T. Nan, J.M. Hu, M. Dai, S. Emori, X. Wang, Z. Hu, A. Matyushov, L.Q. Chen & N. Sun. A strain-mediated magnetoelectric-spin-torque hybrid structure. *Advanced Functional Materials* **29**, 1806371 (2019).

23 N. Reynolds, P. Jadaun, J.T. Heron, C.L. Jermain, J. Gibbons, R. Collette, R. Buhrman, D. Schlom & D. Ralph. Spin Hall torques generated by rare-earth thin films. *Physical Review B* **95**, 064412 (2017).

24 A. Thiaville & Y. Nakatani. Electrical rectification effect in single domain magnetic microstrips: A micromagnetics-based analysis. *Journal of Applied Physics* **104**, 093701 (2008).

25 A. Tulapurkar, Y. Suzuki, A. Fukushima, H. Kubota, H. Maehara, K. Tsunekawa, D. Djayaprawira, N. Watanabe & S. Yuasa. Spin-torque diode effect in magnetic tunnel junctions. *Nature* **438**, 339-342 (2005).

26 C. Kittel. On the theory of ferromagnetic resonance absorption. *Physical Review* **73**, 155 (1948).

27 M.C. Hickey & J.S. Moodera. Origin of intrinsic Gilbert damping. *Physical Review Letters* **102**, 137601 (2009).

28 Y. Tserkovnyak, A. Brataas & G.E. Bauer. Enhanced Gilbert damping in thin ferromagnetic films. *Physical Review Letters* **88**, 117601 (2002).

29 J.C. Sankey, Y.-T. Cui, J.Z. Sun, J.C. Slonczewski, R.A. Buhrman & D.C. Ralph. Measurement of the spin-transfer-torque vector in magnetic tunnel junctions. *Nature Physics* **4**, 67-71 (2008).

30 H. Kubota, A. Fukushima, K. Yakushiji, T. Nagahama, S. Yuasa, K. Ando, H. Maehara, Y. Nagamine, K. Tsunekawa & D.D. Djayaprawira. Quantitative measurement of voltage dependence of spin-transfer torque in MgO-based magnetic tunnel junctions. *Nature Physics* **4**, 37-41 (2008).

31 R. Ramaswamy, Y. Wang, M. Elyasi, M. Motapothula, T. Venkatesan, X. Qiu & H. Yang. Extrinsic spin Hall effect in Cu 1− x Pt x. *Physical Review Applied* **8**, 024034 (2017).

32 G.D.H. Wong, C.C.I. Ang, W.L. Gan, W.C. Law, Z. Xu, F. Xu, C.S. Seet & W.S. Lew. Reversible strain-induced spin–orbit torque on flexible substrate. *Applied Physics Letters* **119**, 042402, doi:10.1063/5.0056995 (2021).

33 G.D.H. Wong, Z. Xu, W.L. Gan, C.C.I. Ang, W.C. Law, J. Tang, W. Zhang, P.K.J. Wong, X. Yu, F. Xu, A.T.S. Wee, C.S. Seet & W.S. Lew. Strain-mediated spin–orbit torque enhancement in Pt/Co on flexible substrate. *ACS Nano* **15**, 8319-8327, doi:10.1021/acsnano.0c09404 (2021).

34 K. Kondou, H. Sukegawa, S. Mitani, K. Tsukagoshi & S. Kasai. Evaluation of spin Hall angle and spin diffusion length by using spin current-induced ferromagnetic resonance. *Applied Physics Express* **5**, 073002 (2012).

35 X. Shu, J. Zhou, J. Deng, W. Lin, J. Yu, L. Liu, C. Zhou, P. Yang & J. Chen. Spin-orbit torque in chemically disordered and $L1_1$-ordered $Cu_{100-x}Pt_x$. *Physical Review Materials* **3**, 114410 (2019).

36 J. Zhou, X. Wang, Y. Liu, J. Yu, H. Fu, L. Liu, S. Chen, J. Deng, W. Lin & X. Shu. Large spin-orbit torque efficiency enhanced by magnetic structure of collinear antiferromagnet IrMn. *Science Advances* **5**, eaau6696 (2019).

37 E. Liu, T. Fache, D. Cespedes-Berrocal, Z. Zhang, S. Petit-Watelot, S. Mangin, F. Xu & J.-C. Rojas-Sánchez. Strain-enhanced charge-to-spin conversion in ta/fe/pt multilayers grown on flexible mica substrate. *Physical Review Applied* **12**, 044074 (2019).

38 Y. Ou, C.-F. Pai, S. Shi, D. Ralph & R. Buhrman. Origin of fieldlike spin-orbit torques in heavy metal/ferromagnet/oxide thin film heterostructures. *Physical Review B* **94**, 140414 (2016).

39 X. Fan, H. Celik, J. Wu, C. Ni, K.-J. Lee, V.O. Lorenz & J.Q. Xiao. Quantifying interface and bulk contributions to spin–orbit torque in magnetic bilayers. *Nature Communications* **5**, 1-8 (2014).

40 L. Huang, S. He, Q.J. Yap & S.T. Lim. Engineering magnetic heterostructures to obtain large spin Hall efficiency for spin-orbit torque devices. *Applied Physics Letters* **113**, 022402 (2018).

41 B. Coester, G.D.H. Wong, Z. Xu, J. Tang, W.L. Gan & W.S. Lew. Enhanced spin Hall conductivity in tungsten-copper alloys. *Journal of Magnetism and Magnetic Materials* **523**, 167545 (2021).

42 Z. Xu, G.D.H. Wong, J. Tang, E. Liu, W. Gan, F. Xu & W.S. Lew. Giant spin Hall effect in Cu-Tb alloy thin films. *ACS Applied Materials & Interfaces* (2020).

43 H. An, Y. Kageyama, Y. Kanno, N. Enishi & K. Ando. Spin–torque generator engineered by natural oxidation of Cu. *Nature Communications* **7**, 1-8 (2016).

44 K.-U. Demasius, T. Phung, W. Zhang, B.P. Hughes, S.-H. Yang, A. Kellock, W. Han, A. Pushp & S.S. Parkin. Enhanced spin–orbit torques by oxygen incorporation in tungsten films. *Nature Communications* **7**, 1-7 (2016).

45 Y. Niimi & Y. Otani. Reciprocal spin Hall effects in conductors with strong spin–orbit coupling: a review. *Reports on Progress in Physics* **78**, 124501 (2015).

46 S.O. Valenzuela & M. Tinkham. Direct electronic measurement of the spin Hall effect. *Nature* **442**, 176-179 (2006).

47 T. Kimura, J. Hamrle & Y. Otani. Estimation of spin-diffusion length from the magnitude of spin-current absorption: Multiterminal ferromagnetic/nonferromagnetic hybrid structures. *Physical Review B* **72**, 014461 (2005).

48 L. Vila, T. Kimura & Y. Otani. Evolution of the spin Hall effect in Pt nanowires: size and temperature effects. *Physical Review Letters* **99**, 226604 (2007).

49 T. Seki, Y. Hasegawa, S. Mitani, S. Takahashi, H. Imamura, S. Maekawa, J. Nitta & K. Takanashi. Giant spin Hall effect in perpendicularly spin-polarized FePt/Au devices. *Nature Materials* **7**, 125-129 (2008).

50 T. Skinner, M. Wang, A. Hindmarch, A. Rushforth, A. Irvine, D. Heiss, H. Kurebayashi & A. Ferguson. Spin-orbit torque opposing the Oersted torque in ultrathin Co/Pt bilayers. *Applied Physics Letters* **104**, 062401 (2014).

51 G. Allen, S. Manipatruni, D.E. Nikonov, M. Doczy & I.A. Young. Experimental demonstration of the coexistence of spin Hall and Rashba effects in β−tantalum/ferromagnet bilayers. *Physical Review B* **91**, 144412 (2015).

52 W. Skowroński, Ł. Karwacki, S. Ziętek, J. Kanak, S. Łazarski, K. Grochot, T. Stobiecki, P. Kuświk, F. Stobiecki & J. Barnaś. Determination of spin Hall angle in heavy-metal/Co−Fe−B-based heterostructures with interfacial spin-orbit fields. *Physical Review Applied* **11**, 024039 (2019).

53 H. An, Y. Kanno, A. Asami & K. Ando. Giant spin-torque generation by heavily oxidized Pt. *Physical Review B* **98**, 014401 (2018).

54 A. Musha, Y. Kanno & K. Ando. Extrinsic-intrinsic crossover of the spin Hall effect induced by alloying. *Physical Review Materials* **3**, 054411 (2019).

55 Y. Kageyama, Y. Tazaki, H. An, T. Harumoto, T. Gao, J. Shi & K. Ando. Spin-orbit torque manipulated by fine-tuning of oxygen-induced orbital hybridization. *Science Advances* **5**, eaax4278 (2019).

56 R. Suzuki, S. Haku, H. Hayashi & K. Ando. Spin-torque ferromagnetic resonance in electrochemically etched metallic device. *Applied Physics Express* **13**, 043007 (2020).

57 H. An, T. Ohno, Y. Kanno, Y. Kageyama, Y. Monnai, H. Maki, J. Shi & K. Ando. Current-induced magnetization switching using an electrically insulating spin-torque generator. *Science Advances* **4**, eaar2250 (2018).

58 C. Wang, Y.-T. Cui, J.A. Katine, R.A. Buhrman & D.C. Ralph. Time-resolved measurement of spin-transfer-driven ferromagnetic resonance and spin torque in magnetic tunnel junctions. *Nature Physics* **7**, 496-501 (2011).

59 S. Petit, C. Baraduc, C. Thirion, U. Ebels, Y. Liu, M. Li, P. Wang & B. Dieny. Spin-torque influence on the high-frequency magnetization fluctuations in magnetic tunnel junctions. *Physical Review Letters* **98**, 077203 (2007).

60 K. Ando, S. Takahashi, K. Harii, K. Sasage, J. Ieda, S. Maekawa & E. Saitoh. Electric manipulation of spin relaxation using the spin Hall effect. *Physical Review Letters* **101**, 036601 (2008).

61 S. Kasai, K. Kondou, H. Sukegawa, S. Mitani, K. Tsukagoshi & Y. Otani. Modulation of effective damping constant using spin Hall effect. *Applied Physics Letters* **104**, 092408 (2014).

62 A. Ganguly, K. Kondou, H. Sukegawa, S. Mitani, S. Kasai, Y. Niimi, Y. Otani & A. Barman. Thickness dependence of spin torque ferromagnetic resonance in Co75Fe25/Pt bilayer films. *Applied Physics Letters* **104**, 072405 (2014).

63 W. Zhang, M.B. Jungfleisch, F. Freimuth, W. Jiang, J. Sklenar, J.E. Pearson, J.B. Ketterson, Y. Mokrousov & A. Hoffmann. All-electrical manipulation of magnetization dynamics in a ferromagnet by antiferromagnets with anisotropic spin Hall effects. *Physical Review B* **92**, 144405 (2015).

64 T. Nan, S. Emori, C.T. Boone, X. Wang, T.M. Oxholm, J.G. Jones, B.M. Howe, G.J. Brown & N.X. Sun. Comparison of spin-orbit torques and spin pumping across NiFe/Pt and NiFe/Cu/Pt interfaces. *Physical Review B* **91**, 214416 (2015).

65 *VERE Isolation Platform*, https://www.vere.com/index.html.

66 *GMW Electromagnet*, https://gmw.com/.

67 *N5183B MXG X-Series Microwave Analog Signal Generator, 9 kHz to 40 GHz*, https://www.keysight.com/sg/en/support/N5183B/mxg-x-series-microwave-analog-signal-generator-9-khz-40-ghz.html.

68 *Picosecond Pulse Labs, Inc. Datasheets for Bias Tees*, https://datasheets.globalspec.com/ ds/3765/PicosecondPulseLabs.

69 *PICOPROBE® MODEL 50A*, https://ggb.com/home/model-50a/.

70 *MFLI 500 kHz / 5 MHz Lock-in Amplifier*, https://www.zhinst.com/others/en/products/mfli-lock-amplifier.

71 I. Neudecker. *Magnetization Dynamics of Confined Ferromagnetic Systems*, (2006).

72 G. Counil, J.-V. Kim, T. Devolder, C. Chappert, K. Shigeto & Y. Otani. Spin wave contributions to the high-frequency magnetic response of thin films obtained with inductive methods. *Journal of Applied Physics* **95**, 5646-5652 (2004).

Chapter 4 Thermal Behavior of Spin-Current Generation in Alloys

The spin Hall efficiency has always been one of the spotlights within the spin-orbit torque community with many research revolving about exploring new methods to enhance it. Among the various methods, the alloying method has grown in popularity in recent years. However, in practical device applications there are many other factors that can affect the performance of the device. One such adversity would be the thermal effects due to the heat dissipation from adjacent devices such as the transistors. In this chapter, we explore the effects of elevated temperature on an alloyed material to study its behavior. Part of this chapter has been published in *Scientific Reports*.[1]

4.1 Motivation

Spin-orbit torque (SOT) has attracted a remarkable amount of attention in the field of spintronics due to its ability to manipulate magnetization.[2-7] SOT-based magnetic memory serves as an alternative for energy-efficient memory as compared to spin-transfer torque magnetic random-access memory (STT-MRAM).[8] In a heavy-metal/ferromagnetic layer (HM/FM) system, the SOT is contributed by two well-known phenomena; the spin Hall effect (SHE) in HM[4,7,9-12] and/or the Rashba-Edelstein effect at their interface.[13-15] In the former, a transverse spin current J_S is generated from charge current J_C passing through the material of strong spin-orbit interaction and injected into the adjacent FM to exert an STT on the magnetization. The magnetization switching efficiency depends on the charge-to-spin current conversion ratio which is defined as the spin Hall angle $\theta_{SH} = (2e/\hbar) J_S / J_C$.[2,5]

Alloying is an established approach to enhance spin Hall efficiency by increasing the extrinsic contribution of SHE and this has been shown in many previous studies. *R. Ramaswamy et al.* reported that with as little as x = 28% in Pt_xCu_{1-x}, one can achieve similar spin Hall efficiency as pure Pt. From his study, an enhancement in spin Hall efficiency was observed at room temperature.[16] However, it is also important to characterize the SHE at the elevated temperatures that MRAM devices are often operated at. During MRAM switching, a large current is required resulting in temperature rise that could potentially lead to detrimental effects on the device performance. Temperature studies using various characterization

techniques including second harmonic measurement,[17-20] spin-pumping[21] and spin-transfer ferromagnetic resonance (ST-FMR)[22] have been explored but only within and below room temperature.[23] Although the effects of elevated temperature on SHE is crucial for device applications,[24,25] the quest for high temperature SHE characterization remains relatively uncharted. In a recent ST-FMR study by *P. Phu*, a joule heating technique was applied to momentarily raise the temperature of the sample during characterization.[23] The usage of a heating element as deployed in our experimental setup could provide consistent heating similar to external stimulus for investigating the thermal dependence of spin conductance measurements.

In this chapter, we demonstrated that alloying can help to improve the thermal robustness of spin generation in high spin-orbit coupling (SOC) materials. This was evident by performing in-situ high temperature ST-FMR measurement on our sample, Pt_xCu_{1-x}/Co/Ta. The results revealed that both the spin Hall efficiency and the thermal stability are enhanced in Pt_xCu_{1-x} alloys. The highest spin transparency was observed in the alloy with the smallest switching current density. Our work indicates that there is a relation between the three components of a spin-torque generator: switching current density, diffusion length and spin transparency. This work provides a way to engineer thermally robust spin current generating alloys for application at elevated temperatures.

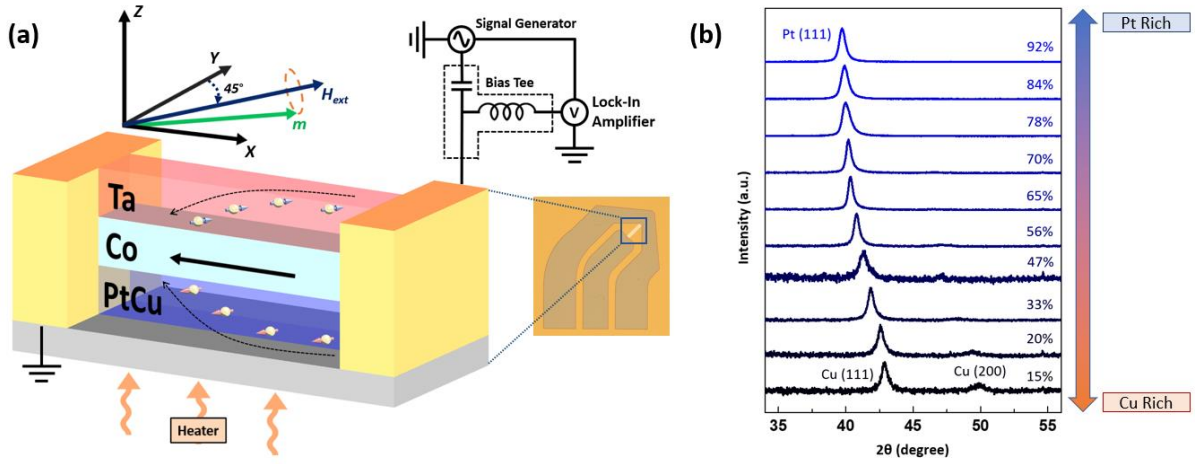

Figure 4-1 (a) Schematic illustration of high temperature ST-FMR setup. Heat is applied from the bottom of the sample stage through a heating element and the temperature is calibrated at the surface of the sample substrate. Optical image of the device is as shown in the inset. (b) X-ray diffraction pattern of 80nm thick Pt_xCu_{1-x} samples showing the shift between the Pt(111) to the Cu(111) peak. The composition of Pt_xCu_{1-x} were determined using EDX spectroscopy.

4.2 Experimental Details

The films were sputtered onto thermally oxidized Si substrates with (100) orientation using an Ar pressure of 2 mTorr and a base pressure <5 × 10^{-8} Torr. Two-inch-diameter targets were used. Stack structure of substrate/Pt_xCu_{1-x}(5 nm)/Co(5 nm)/Ta(5 nm) was fabricated for temperature investigation. Ta was introduced as the spin current source to complement Pt_xCu_{1-x} due to their opposite spin Hall angle signs.[5,16,22] The Pt_xCu_{1-x} alloys are obtained by co-sputtering both Pt and Cu and its atomic composition is varied by adjusting their sputtering power. The sputter power of the deposition system at Pt target is varied between 20 to 100 W while for the Cu target, it is varied from 50 to 150 W. Energy-dispersive X-ray (EDX) spectroscopy was used to verify the percentage composition of the alloys. X-ray diffraction (XRD) results for 80nm thick Pt_xCu_{1-x} films on a continuous Si substrate are shown in Figure 4-1b. Similarly, in the case of pure Pt and Cu, Pt_xCu_{1-x} had a face-centered-cubic (fcc) structure with the Pt_xCu_{1-x} (111) peak gradually shifting from the Pt (111) to the Cu (111) with increasing Cu concentration. At around 70% Pt composition, Pt_xCu_{1-x} (200) peak becomes observable and its intensity gradually increased with decreasing Pt_xCu_{1-x} (111) peak as it transited to the Cu-rich region. From this, it can be concluded that the fcc (111)-textured alloy remained unchanged between the transition of Pt-rich and Cu-rich films, which indicated that the two elements mix well in their binary alloys.

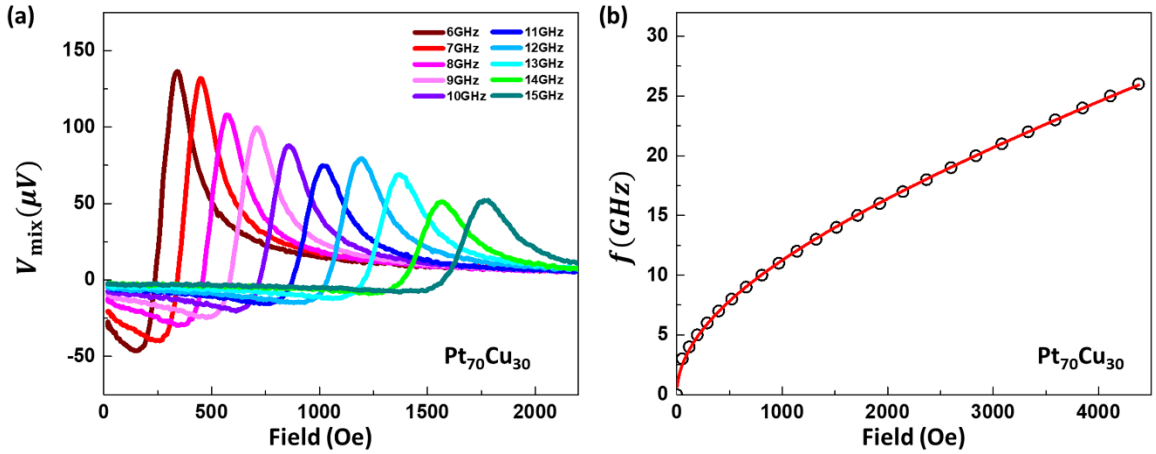

Figure 4-2 (a) Measured ST-FMR spectra of $Pt_{60}Cu_{40}$(5 nm)/Co(5 nm)/Ta(5 nm) trilayer device for frequency from 6 to 15 GHz with nominal input power of 18 dBm. (b) Fitting of Kittel equation for $Pt_{70}Cu_{30}$(5 nm)/Co(5 nm)/Ta(5 nm) trilayer.

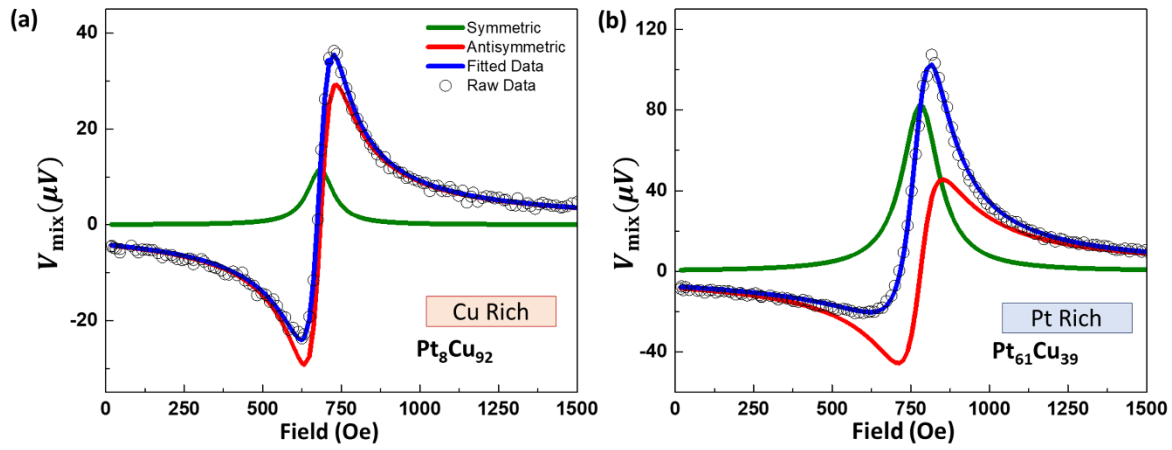

Figure 4-3 ST-FMR Lorentzian fitting of ST-FMR spectra of Pt_xCu_{1-x}(5 nm)/Co(5 nm)/Ta(5 nm) trilayer for (a) x = 8% and (b) 61% and a microwave frequency of 9 GHz. The symmetric component in the Pt rich alloy is much larger than in the Cu rich alloy indicating a larger spin Hall efficiency.

In this study, the spin-torque ferromagnetic resonance (ST-FMR) was deployed to determine the Gilbert damping, α, and spin Hall efficiency, $\theta_{\text{eff.}}$ When the FMR condition was met, the magnetization precession driven by the torques will result in the maximum oscillation of the resistance caused by anisotropic magnetoresistance (AMR) in the Co layer. When coupled together with the oscillating current, a rectified DC voltage was produced and detected using a lock-in amplifier with amplitude modulation of the RF signal. Figure 4-1a illustrates the high temperature ST-FMR setup used with an inset showing an optical image of the device consisting of a microstrip (10 × 50 μm) tilted at 45° with its coplanar waveguide (CPW) electrode. RF charge current was injected through the long axis of the stripe while an in-plane external magnetic field H_{ext} was swept. The longitudinal RF current passing through the device generates a transverse spin current which was then injected into the adjacent Co layer. The magnetization of Co experienced two torques induced by the RF current; an in-plane torque and an out-of-plane torque.[26] The measurement was performed at a microwave power of 18 dBm and measured between 6 to 20 GHz in steps of 1 GHz. Figure 4-2a. shows a segment of the measured ST-FMR spectra with varying current frequencies for $Pt_{60}Cu_{40}$ (5 nm)/Co (5 nm)/Ta (5 nm).

4.3 ST-FMR Characterization

The measured rectified DC voltage V_{mix} is then fitted using Equation 3.8.4 and as shown in Figure 4-3a and b are examples of the Lorentz ST-FMR fitting equation for Cu-rich and Pt-rich trilayer system respectively.[22] The red and the green solid curves are the extracted symmetric and antisymmetric voltage contributions. The fitted curve for the summation of both contributions is fitted in blue and it overlaps well with the raw data indicating a good fit. Through the fitting of Equation 3.8.4, the frequency dependence of properties such as resonance field H_{res}, linewidth ΔH, symmetric component S, and anti-symmetric component A was obtained. Figure 4-2b shows the frequency dependence of the resonance field as described by the Equation 3.8.6.[27]

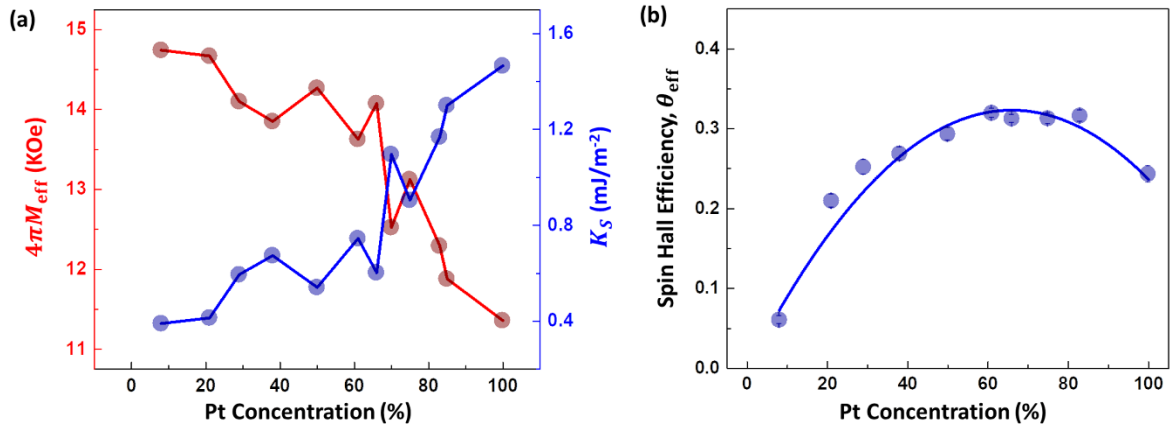

Figure 4-4 (a) The effective magnetization $4\pi M_{eff}$ (red circles) and surface magnetic anisotropy constant K_S (blue circles) dependence on Pt concentration in Pt_xCu_{1-x}(5 nm)/Co(5 nm)/Ta(5 nm) films. (b) θ_{eff} at different Pt concentration extracted using the "lineshape" method (V_S/V_A ratio).

In Figure 4-4a, the effective magnetization given by $4\pi M_{eff} = 4\pi M_S - 2K_S / M_S t$ decreases as Pt concentration increases while the surface anisotropy constant K_S increases. From Figure 4-4b the θ_{eff} of Pt_xCu_{1-x} behaves in a parabolic manner as it increases upon the introduction of Cu into the alloy. This resulted from additional extrinsic SHE from skew and side jump scattering. As the composition of Pt increases indicating that there is an enhancement of the surface anisotropy constant K_S with the introduction of a heavy metal. This can be attributed to a stronger spin-orbit coupling (SOC) when more Pt is present in the alloy. The

FMR linewidth shows a linear dependence with the frequencies measured; indicating that the two-magnon scattering mechanism had negligible contribution in our samples.[28] Subsequently, the relation between frequency and the linewidth was examined using the Equation 3.8.7.[29] Furthermore, as the decrease in intrinsic SHE outweighs the increase, the θ_{eff} starts to deteriorate. The Gilbert damping in Co increases as Pt concentration increases as shown in Figure 4-5a. This enhanced damping is a result of spin pumping to the adjacent metal of high spin-orbit coupling. Figure 4-5b shows the resistivity of Pt_xCu_{1-x} at different Pt concentration fitted to the Nordheim relation for homogenous solid; $\rho_{Pt_xCu_{1-x}} = C_1 x(100-x) + (\rho_{Pt}/100)x + (\rho_{Cu}/100-x)$, where C_1 is coefficient of parabolic relation, ρ_{Pt} and ρ_{Cu} are the resistivity of Pt and Cu respectively.[30,31] The data fits well with the parabolic relation which indicates that the Pt_xCu_{1-x} alloys are homogenous.

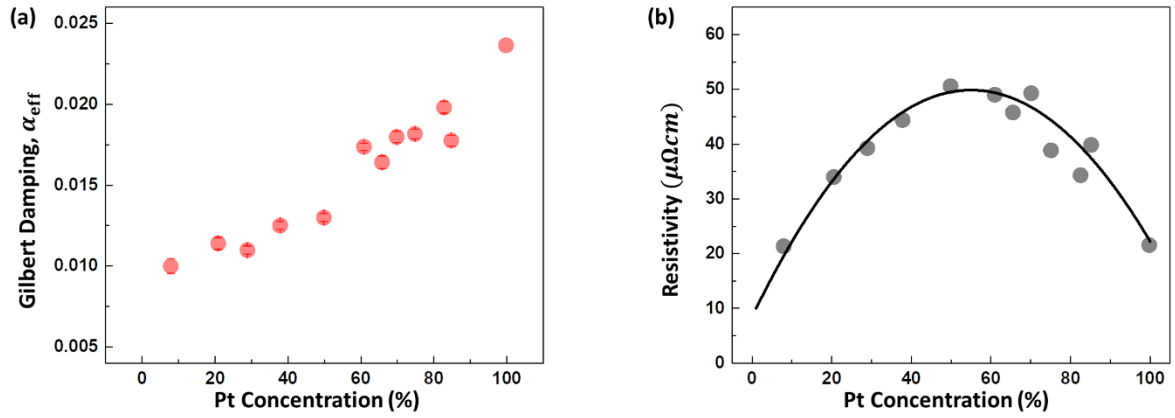

Figure 4-5 (a) α_{eff} at different Pt concentration calculated from the ST-FMR linewidth. (b) $\rho_{Pt_xCu_{1-x}}$ at different Pt concentration fitted with the Nordheim relation.

4.4 Temperature Dependence of Gilbert Damping

For device application, damping parameters should ideally be constant across the operating temperature range to maintain a consistent switching. The effective Gilbert damping constant of the trilayer system is given by $\alpha = \alpha_{\text{int}} + \alpha_{\text{SP}}$, where α_{int} is the intrinsic Gilbert damping contribution from Co and α_{SP} is the damping introduced by spin pumping effect due to the adjacent heavy metals.[32,33] Damping contribution from the proximity effect is assumed to be negligibly small as it only affects the first atomic layer of Pt.[28,34-37] From Equation 3.8.7 using the slope of the linear relation between the linewidth and frequency, the effective Gilbert damping can be calculated. Figure 4-6a shows the calculated damping constants for varying Pt concentrations at different temperatures. The damping constant increases with higher Pt concentration which is in good agreement with the trend observed in prior reports.[16,38] This could be due to the enhanced spin pump effect and interface anisotropy for elements with larger SOC.[32,33]

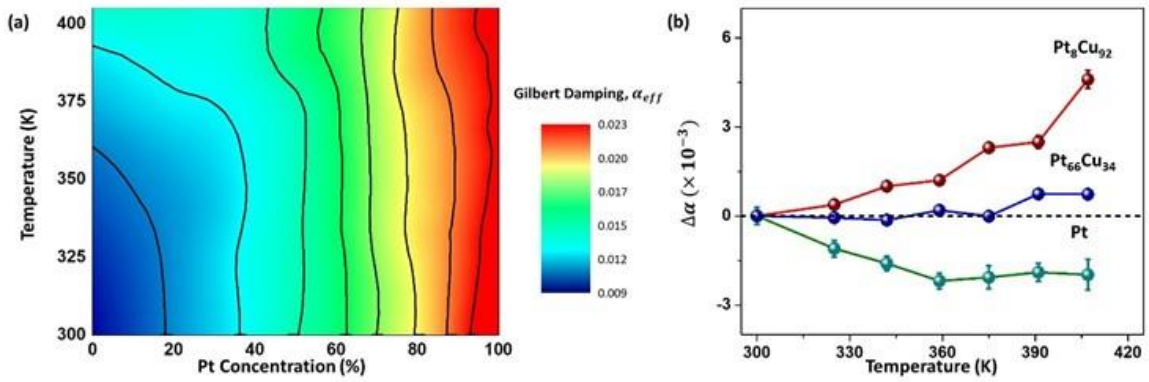

Figure 4-6 (a) Contour plot of α for Pt_xCu_{1-x}(5 nm)/Co(5 nm)/Ta(5 nm) trilayer device with temperature for varying Pt concentrations. (b) $\Delta\alpha$ of Pt_xCu_{1-x}(5 nm)/Co(5 nm)/Ta(5 nm) for x = 8%, 66% and 100%. The temperature dependence of α_{int} and α_{SP} are inverse of one another and at the optimal alloy composition, both contributions will counteract and give rise to a thermally robust alloy.

With accordance to the torque-correlation model, damping is attributed from two main contributions: the intraband electron-hole transitions and the interband electron-hole transitions.[50,51] This model states that the intraband transitions contributions is proportional to relaxation time and that this contribution follows the breathing Fermi-surface model which

Kambersk´y theorized for the dynamics of homogeneous magnetization. On the other hand, the interband transitions contributions has an inversely relation to the relaxation time and is described by the bubbling Fermi-surface model. Therefore, the relaxation relation characteristic from the intra- and inter- band transition contribution leads to the temperature dependence of the intrinsic and spin pumping contribution of the damping. As such, α_{SP} is inversely proportional to temperature whereas α_{int} is directly proportional to the increase in temperature.[39] Here, $\Delta\alpha$ refers to the change in Gilbert damping constant due to an increase in temperature with respect to room temperature. Figure 4-6b shows $\Delta\alpha$ of Pt_xCu_{1-x} at different Pt compositions. When the alloy is within the Cu-rich regime, the increase in damping due to α_{int} is much greater than the decrease from α_{SP}. Therefore, this leads to an overall increase in damping($\Delta\alpha_{int} > \Delta\alpha_{SP}$). Upon increasing the Pt concentration beyond 45%, the Pt-rich regime is established. The magnitude change for the two main damping contributions at this point is approximately the same, giving rise to near-zero increment in damping with the change in temperature($\Delta\alpha_{int} \approx \Delta\alpha_{SP}$). As Pt starts to saturate towards 100% concentration, α_{SP} begins to dominate and the overall damping decreases with temperature($\Delta\alpha_{int} < \Delta\alpha_{SP}$).

4.5 Temperature Dependence of Spin Hall Efficiency

To calculate the spin Hall efficiency of the trilayer system, we implement the line-shape method using Equation 3.8.8.[22] This lineshape method is the most suitable for bilayer structures with a negligible field-like contribution. When used in a trilayer structure, Oersted field generated from the heavy metal layers at the top and bottom will result in cancellation and thus result in an underestimate of the θ_{eff}.[40] To account for this, a correction factor of $1/[1 + (H_{FL}/H_{Oe})]$ can be added where H_{FL} is the fieldlike spin-orbit torque and H_{Oe} is the Oersted field generated.[41,42] Because the resistivity of Ta (216 μΩ cm) is much higher than that of Pt_xCu_{1-x} (10-51 μΩ cm), the current density in Ta is small. Thus, the Oersted field attributed by Ta is ignored as H_{FL}/H_{Oe} is negligible. With the assumption that the top 3nm of Ta forms TaO_x, the θ_{eff} of Pt/Co/Ta measured at room temperature in our work is 0.24 ± 0.03 which is in agreement with previous works suggesting that our approximation is appropriate.[43]

Figure 4-7a summarizes the θ_{eff} across different Pt concentrations at elevated temperatures. Here, we observe that the θ_{eff} has a parabolic dependence with the Pt concentration as shown in Figure 4-4b and this is attributed to the additional extrinsic SHE

through alloying.[16] At room temperature, Pt_xCu_{1-x}/Co/Ta has a peak θ_{eff} of 0.32 ± 0.03 at x = 67%. As shown in Figure 4-7b and c, the Cu-rich alloy is more temperature-sensitive and its θ_{eff} deteriorates more significantly with increasing temperature as compared to the Pt-rich alloy. This decrease in θ_{eff} is most pronounced when x = 15 to 40% as shown by the slightly

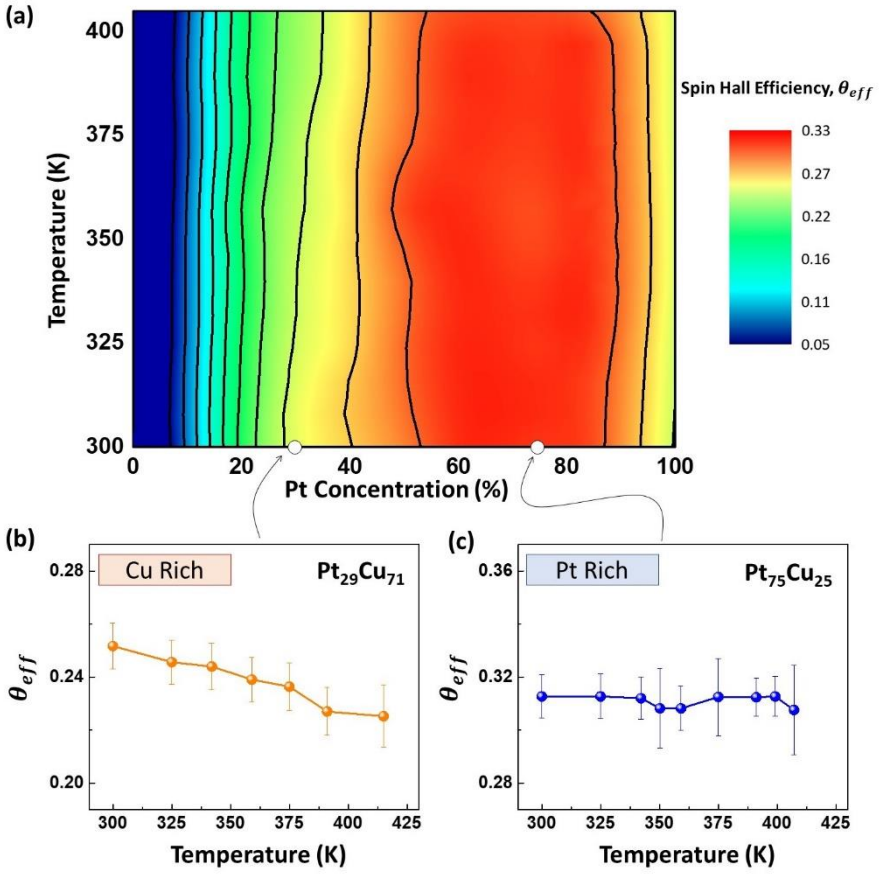

Figure 4-7 (a) Contour plot of θ_{eff} for Pt_xCu_{1-x}(5 nm)/Co(5 nm)/Ta(5 nm) trilayer device with temperature for varying Pt concentrations. (b) and (c) Temperature dependence of θ_{eff} for Cu-rich and Pt-rich Pt_xCu_{1-x}(5 nm)/Co(5 nm)/Ta(5 nm) trilayer device with x = 29% and 75% respectively. The θ_{eff} of Cu rich alloys decreases with increasing temperature while Pt rich alloys remain relatively stable.

slanted vertical lines in Figure 4-7a, which is a result of the predominant side-jump scattering contribution with this region. Side-jump scattering is temperature-dependent while intrinsic and skew scattering contributions are temperature independent. Skew scattering contribution is more dominant when the alloy has a dominating element within the composition.[44-46] At x = 75%, the extrinsic and intrinsic SHE is maximized while being temperature insensitive.

4.6 Spin Transparency and Switching Current Density Relation

Since the optimal spin hall efficiency and damping constant occur at different Pt concentrations, there is a need to analyze and characterize them such that the optimal SOT efficiency for current-induced switching application at elevated temperature can be determined. To do so, the critical switching current density, J_{c0}, was evaluated at various temperatures. The required J_{c0} for in-plane magnetization switching using SOT is given by

$$J_{c0} \approx \frac{2e}{\hbar}\frac{\alpha_{\text{eff}}}{\theta_{\text{eff}}}\left(\frac{4\pi M_{\text{eff}}}{2}\right) M_S t\,, \tag{4.6.1}$$

which is proportional to $\alpha_{\text{eff}}/\theta_{\text{eff}}$. By plotting the ratio at different temperatures as shown in Figure 4-8a, the optimal Pt concentration that has the lowest critical switching current density was found at x = 45%. This occurs at the transition between the Cu-rich and Pt-rich regimes where the alloy becomes more thermally robust. To further understand the reason behind the optimal Pt concentration, the spin diffusion length and the spin transparency were characterized.

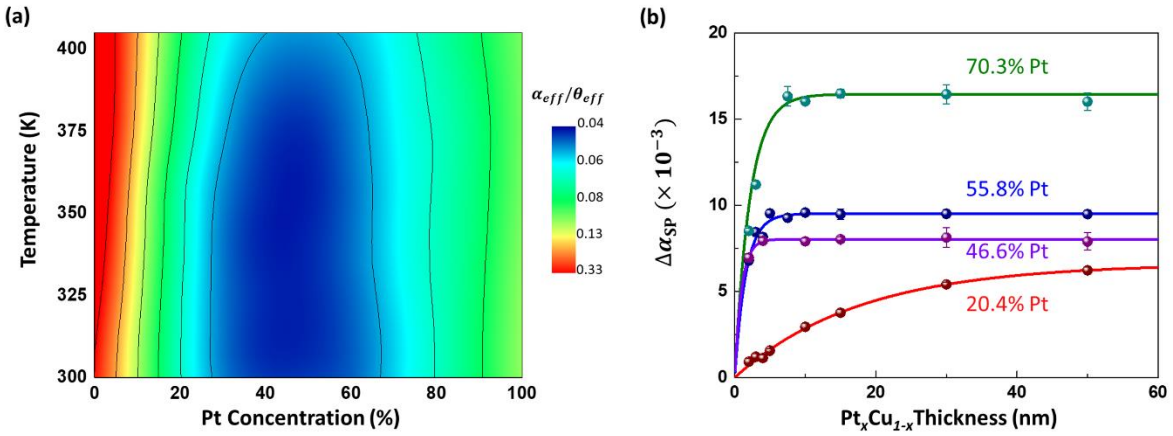

Figure 4-8 (a) Contour plot of $\alpha_{\text{eff}}/\theta_{\text{eff}}$ ratio for Pt_xCu_{1-x}(5 nm)/Co(5 nm)/Ta(5 nm) trilayer device with temperature. (b) Damping parameter due to spin pumping of Pt_xCu_{1-x}(t nm)/Co(20 nm)/Ru(5 nm) with varying t thickness of Co for x = 20.4%, 46.6%, 55.8% and 70.3%.

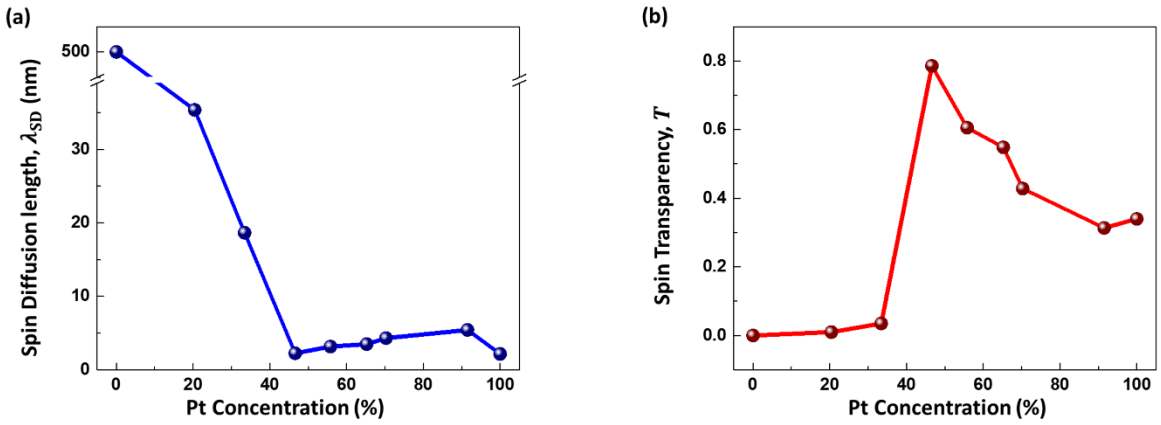

Figure 4-9 Alloy composition dependence of (a) spin diffusion length and (b) spin transparency, respectively, for Pt_xCu_{1-x}(5 nm)/Co(20 nm)/Ru(5 nm). Both the spin diffusion length dip and spin transparency peak occur at $Pt_{47}Cu_{53}$.

The thickness dependence of the heavy metal and damping can be described by[33]

$$\alpha_{\text{eff}} = \alpha_{\text{int}} + \frac{g\mu_{\text{B}}}{4\pi M_{\text{S}}\left(t_{\text{Co}} - t_{\text{d}}\right)} G^{\uparrow\downarrow}_{\text{Pt}_x\text{Cu}_{1-x}} \left(1 - e^{\frac{-2t_{\text{Pt}_x\text{Cu}_{1-x}}}{\lambda}}\right), \tag{4.6.2}$$

where g is the g-factor, t_d is the magnetic dead layer thickness, $G^{\uparrow\downarrow}_{\text{Pt}_x\text{Cu}_{1-x}}$ is the effective spin-mixing conductance due to Pt_xCu_{1-x} and λ is the spin diffusion length. Figure 4-8b shows the change in damping, $\Delta\alpha_{SP}$, of Pt_xCu_{1-x}(t nm)/Co(20 nm)/Ru(5 nm) measured using FMR for varying t thickness of Co at different Pt concentrations due to enhanced damping from alloy. Fitting the data with Equation 4.6.2, the spin diffusion length for different Pt concentrations was obtained. Figure 4-9a indicates that around $Pt_{45}Cu_{55}$, the spin diffusion length is the shortest at 1.9 ± 0.2 nm. The spin transparency can be calculated by the following model,[47-49]

$$T = \frac{G^{\uparrow\downarrow}_{\text{Pt}_x\text{Cu}_{1-x}} \tanh\left(\frac{d}{2\lambda}\right)}{G^{\uparrow\downarrow}_{\text{Pt}_x\text{Cu}_{1-x}} \coth\left(\frac{d}{\lambda}\right) + \frac{\sigma}{\lambda}\frac{h}{2e^2}} \tag{4.6.3}$$

where T is the spin transparency and σ is the electrical conductivity of Pt_xCu_{1-x}. The electrical resistivity of Pt_xCu_{1-x} as a function of Pt concentration has a parabolic relation that follows the Nordheim rule for homogenous solid solutions. In Figure 4-9b, we observe that T peaks at 0.85 ± 0.09 when the Pt concentration is at x = 45%. This peak indicates that there is a relation between the critical switching current density and spin transparency. Improvement in spin transparency between the interface of the FM and the HM results in an increase in spin current propagation, thus reducing the switching current density.[47]

In summary, we have investigated the damping constant and spin Hall efficiency of Pt_xCu_{1-x} at elevated temperatures and discovered that they can be modulated by adjusting the temperature and alloy composition. Pt_xCu_{1-x} that have higher Pt content is less sensitive to temperature, but they suffer a tradeoff with higher damping. By tuning the alloy composition to $Pt_{47}Cu_{53}$, the minimum ratio of $\alpha_{\mathrm{eff}}/\theta_{\mathrm{eff}}$ can be achieved, which could reduce the switching current density for magnetization reversal. The temperature dependence of effective damping is also negligible due to the counteracting relationship between α_{int} and α_{SP}. The spin diffusion length is at its smallest at 1.9 ± 0.2 nm and has high spin transparency of 0.85 ± 0.09. Therefore, our work here has demonstrated a method of characterizing the spin Hall channel material and its optimization for device application at elevated temperatures.

Reference

1 G.D.H. Wong, W.L. Law, F.N. Tan, W.L. Gan, C.C.I. Ang, Z. Xu, C. Seet & W.S. Lew. Thermal behavior of spin-current generation in Pt_xCu_{1-x} devices characterized through spin-torque ferromagnetic resonance. *Scientific Reports* **10**, 1-8 (2020).

2 I.M. Miron, K. Garello, G. Gaudin, P.-J. Zermatten, M.V. Costache, S. Auffret, S. Bandiera, B. Rodmacq, A. Schuhl & P. Gambardella. Perpendicular switching of a single ferromagnetic layer induced by in-plane current injection. *Nature* **476**, 189 (2011).

3 C.O. Avci, A. Quindeau, C.-F. Pai, M. Mann, L. Caretta, A.S. Tang, M.C. Onbasli, C.A. Ross & G.S. Beach. Current-induced switching in a magnetic insulator. *Nature Materials* **16**, 309 (2017).

4 S. Emori, U. Bauer, S.-M. Ahn, E. Martinez & G.S. Beach. Current-driven dynamics of chiral ferromagnetic domain walls. *Nature Materials* **12**, 611-616 (2013).

5 L. Liu, C.-F. Pai, Y. Li, H. Tseng, D. Ralph & R. Buhrman. Spin-torque switching with the giant spin Hall effect of tantalum. *Science* **336**, 555-558 (2012).

6 P. Haazen, E. Murè, J. Franken, R. Lavrijsen, H. Swagten & B. Koopmans. Domain wall depinning governed by the spin Hall effect. *Nature Materials* **12**, 299 (2013).

7 Q.Y. Wong, C. Murapaka, W.C. Law, W.L. Gan, G.J. Lim & W.S. Lew. Enhanced spin-orbit torques in rare-earth Pt/$[Co/Ni]_2$/Co/Tb systems. *Physical Review Applied* **11**, 024057 (2019).

8 M. Baumgartner, K. Garello, J. Mendil, C.O. Avci, E. Grimaldi, C. Murer, J. Feng, M. Gabureac, C. Stamm & Y. Acremann. Spatially and time-resolved magnetization dynamics driven by spin–orbit torques. *Nature Nanotechnology* **12**, 980 (2017).

9 S. Valenzuela & M. Tinkham. Electrical detection of spin currents: The spin-current induced Hall effect. *Journal of Applied Physics* **101**, 09B103 (2007).

10 J. Hirsch. Spin hall effect. *Physical Review Letters* **83**, 1834 (1999).

11 S. Zhang. Spin Hall effect in the presence of spin diffusion. *Physical Review Letters* **85**, 393 (2000).

12 F. Luo, Q.Y. Wong, S. Li, F.N. Tan, G.J. Lim, X. Wang & W.S. Lew. Dependence of spin-orbit torque effective fields on magnetization uniformity in Ta/Co/Pt structure. *Scientific Reports* **9**, 1-7 (2019).

13 K. Garello, I.M. Miron, C.O. Avci, F. Freimuth, Y. Mokrousov, S. Blügel, S. Auffret, O. Boulle, G. Gaudin & P. Gambardella. Symmetry and magnitude of spin–orbit torques in ferromagnetic heterostructures. *Nature Nanotechnology* **8**, 587 (2013).

14 J. Kim, J. Sinha, M. Hayashi, M. Yamanouchi, S. Fukami, T. Suzuki, S. Mitani & H. Ohno. Layer thickness dependence of the current-induced effective field vector in Ta|CoFeB|MgO. *Nature Materials* **12**, 240 (2013).

15 Y.-W. Oh, S.-h.C. Baek, Y. Kim, H.Y. Lee, K.-D. Lee, C.-G. Yang, E.-S. Park, K.-S. Lee, K.-W. Kim & G. Go. Field-free switching of perpendicular magnetization through spin–orbit torque in antiferromagnet/ferromagnet/oxide structures. *Nature Nanotechnology* **11**, 878 (2016).

16 R. Ramaswamy, Y. Wang, M. Elyasi, M. Motapothula, T. Venkatesan, X. Qiu & H. Yang. Extrinsic spin Hall effect in $Cu_{1-x}Pt_x$. *Physical Review Applied* **8**, 024034 (2017).

17 X. Qiu, P. Deorani, K. Narayanapillai, K.-S. Lee, K.-J. Lee, H.-W. Lee & H. Yang. Angular and temperature dependence of current induced spin-orbit effective fields in Ta/CoFeB/MgO nanowires. *Scientific Reports* **4**, 4491 (2014).

18 Y. Wen, J. Wu, P. Li, Q. Zhang, Y. Zhao, A. Manchon, J.Q. Xiao & X. Zhang. Temperature dependence of spin-orbit torques in Cu-Au alloys. *Physical Review B* **95**, 104403, doi:10.1103/PhysRevB.95.104403 (2017).

19 S. Li, S. Goolaup, J. Kwon, F. Luo, W.L. Gan & W.S. Lew. Deterministic spin-orbit torque induced magnetization reversal in Pt/$[Co/Ni]_n$/Co/Ta multilayer Hall bars. *Scientific Reports* **7**, 972 (2017).

20 F. Luo, S. Goolaup, S. Li, G.J. Lim, F.N. Tan, C. Engel, S. Zhang, F. Ma, T. Zhou & W.S. Lew. Characterizing the spin orbit torque field-like term in in-plane magnetic system using transverse field. *Journal of Applied Physics* **120**, 083908 (2016).

21 E. Saitoh, M. Ueda, H. Miyajima & G. Tatara. Conversion of spin current into charge current at room temperature: Inverse spin-Hall effect. *Applied Physics Letters* **88**, 182509 (2006).

22 L. Liu, T. Moriyama, D. Ralph & R. Buhrman. Spin-torque ferromagnetic resonance induced by the spin Hall effect. *Physical Review Letters* **106**, 036601 (2011).

23 P. Phu, K. Yamanoi, K. Ohnishi, J. Hyodo, K. Rogdakis, Y. Yamazaki, T. Kimura & H. Kurebayashi. Bolometric ferromagnetic resonance techniques for characterising spin-Hall effect at high temperatures. *Journal of Magnetism and Magnetic Materials* **485**, 304-307 (2019).

24 J. Slaughter, K. Nagel, R. Whig, S. Deshpande, S. Aggarwal, M. DeHerrera, J. Janesky, M. Lin, H.-J. Chia & M. Hossain. in *2016 IEEE International Electron Devices Meeting (IEDM)*. 21.25. 21-21.25. 24 (IEEE).

25 W. Law, T. Tahmasebi, F. Tan, T. Jin, W. Gan, R. Nistala, X. Zhu, Z. Mo, H. Teo & C. Seet. High temperature ferromagnetic resonance study on pMTJ stacks with diffusion barrier layers. *Journal of Physics D: Applied Physics* **51**, 405001 (2018).

26 H. Kurebayashi, J. Sinova, D. Fang, A. Irvine, T. Skinner, J. Wunderlich, V. Novák, R. Campion, B. Gallagher & E. Vehstedt. An antidamping spin–orbit torque originating from the Berry curvature. *Nature Nanotechnology* **9**, 211 (2014).

27 C. Kittel. On the theory of ferromagnetic resonance absorption. *Physical Review* **73**, 155 (1948).

28 J. Geissler, E. Goering, M. Justen, F. Weigand, G. Schütz, J. Langer, D. Schmitz, H. Maletta & R. Mattheis. Pt magnetization profile in a Pt/Co bilayer studied by resonant magnetic X-ray reflectometry. *Physical Review B* **65**, 020405, doi:10.1103/PhysRevB.65.020405 (2001).

29 M. Belmeguenai, H. Tuzcuoglu, M. Gabor, T. Petrisor Jr, C. Tiusan, D. Berling, F. Zighem, T. Chauveau, S. Chérif & P. Moch. Co_2FeAl thin films grown on MgO substrates: Correlation between static, dynamic, and structural properties. *Physical Review B* **87**, 184431 (2013).

30 K. Chopra, A. Thakoor, S. Barthwal & P. Nath. Electron transport properties of amorphous Cu-Ag films. *Physica Status Solidi (a)* **40**, 247-255 (1977).

31 L. Nordheim. The electron theory of metals. *Ann. Phys* **9**, 607 (1931).

32 O. Mosendz, V. Vlaminck, J.E. Pearson, F.Y. Fradin, G.E.W. Bauer, S.D. Bader & A. Hoffmann. Detection and quantification of inverse spin Hall effect from spin pumping in permalloy/normal metal bilayers. *Physical Review B* **82**, 214403, doi:10.1103/PhysRevB.82.214403 (2010).

33 J.M. Shaw, H.T. Nembach & T.J. Silva. Determination of spin pumping as a source of linewidth in sputtered $Co_{90}Fe_{10}$/Pd multilayers by use of broadband ferromagnetic resonance spectroscopy. *Physical Review B* **85**, 054412 (2012).

34 T. Koyama, Y. Guan, Y. Hibino, M. Suzuki & D. Chiba. Magnetization switching by spin-orbit torque in Pt with proximity-induced magnetic moment. *Journal of Applied Physics* **121**, 123903 (2017).

35 S. Ferrer, J. Alvarez, E. Lundgren, X. Torrelles, P. Fajardo & F. Boscherini. Surface X-ray diffraction from C o/P t (111) ultrathin films and alloys: Structure and magnetism. *Physical Review B* **56**, 9848 (1997).

36 H. Bouloussa, R. Ramaswamy, Y. Roussigné, A. Stashkevich, H. Yang, M. Belmeguenai & S. Chérif. Pt concentration dependence of the interfacial Dzyaloshinskii–Moriya interaction, the Gilbert damping parameter and the magnetic anisotropy in Py/$Cu_{1-x}Pt_x$ systems. *Journal of Physics D: Applied Physics* **52**, 055001 (2018).

37 T. White, T. Bailey, M. Pierce & C.W. Miller. Strong Spin Pumping in Permalloy-Iridium Heterostructures. *IEEE Magnetics Letters* **8**, 1-4 (2017).

38 L. Zhu, D.C. Ralph & R.A. Buhrman. Highly Efficient Spin-Current Generation by the Spin Hall Effect in Au 1− x Pt x. *Physical Review Applied* **10**, 031001 (2018).

39 T. Verhagen, H. Tinkey, H. Overweg, M. van Son, M. Huber, J. van Ruitenbeek & J. Aarts. Temperature dependence of spin pumping and Gilbert damping in thin Co/Pt bilayers. *Journal of Physics: Condensed Matter* **28**, 056004 (2016).

40 L. Huang, S. He, Q.J. Yap & S.T. Lim. Engineering magnetic heterostructures to obtain large spin Hall efficiency for spin-orbit torque devices. *Applied Physics Letters* **113**, 022402 (2018).

41 W. Skowroński, Ł. Karwacki, S. Ziętek, J. Kanak, S. Łazarski, K. Grochot, T. Stobiecki, P. Kuświk, F. Stobiecki & J. Barnaś. Determination of Spin Hall Angle in Heavy-Metal/Co−Fe−B-Based Heterostructures with Interfacial Spin-Orbit Fields. *Physical Review Applied* **11**, 024039 (2019).

42 E. Liu, T. Fache, D. Cespedes-Berrocal, Z. Zhang, S. Petit-Watelot, S. Mangin, F. Xu & J.-C. Rojas-Sánchez. Strain-Enhanced Charge-to-Spin Conversion in Ta/Fe/Pt Multilayers Grown on Flexible Mica Substrate. *Physical Review Applied* **12**, 044074 (2019).

43 S. Woo, M. Mann, A.J. Tan, L. Caretta & G.S. Beach. Enhanced spin-orbit torques in Pt/Co/Ta heterostructures. *Applied Physics Letters* **105**, 212404 (2014).

44 A. Fert & P.M. Levy. Spin Hall Effect Induced by Resonant Scattering on Impurities in Metals. *Physical Review Letters* **106**, 157208, doi:10.1103/PhysRevLett.106.157208 (2011).

45 S. Lowitzer, M. Gradhand, D. Ködderitzsch, D.V. Fedorov, I. Mertig & H. Ebert. Extrinsic and Intrinsic Contributions to the Spin Hall Effect of Alloys. *Physical Review Letters* **106**, 056601, doi:10.1103/PhysRevLett.106.056601 (2011).

46 A. Hoffmann. Spin Hall effects in metals. *IEEE Transactions on Magnetics* **49**, 5172-5193 (2013).

47 W. Zhang, W. Han, X. Jiang, S.-H. Yang & S.S. Parkin. Role of transparency of platinum–ferromagnet interfaces in determining the intrinsic magnitude of the spin Hall effect. *Nature Physics* **11**, 496 (2015).

48 X. Wang, C.O. Pauyac & A. Manchon. Spin-orbit-coupled transport and spin torque in a ferromagnetic heterostructure. *Physical Review B* **89**, 054405 (2014).

49 Y. Wang, P. Deorani, X. Qiu, J.H. Kwon & H. Yang. Determination of intrinsic spin Hall angle in Pt. *Applied Physics Letters* **105**, 152412 (2014).

50 M. Fähnle & C. Illg. Electron theory of fast and ultrafast dissipative magnetization dynamics. *Journal of Physics: Condensed Matter* **23**, 493201 (2011).

51 Y. Zhao, Q. Song, S.-H. Yang, T. Su, W. Yuan, S.S. Parkin, J. Shi & W. Han. Experimental investigation of temperature-dependent Gilbert damping in permalloy thin films. *Scientific Reports* **6**, 1-8 (2016).

Chapter 5 Strain-Mediated Spin-Orbit Torque Enhancement

Current-induced magnetization switching by spin-current generated in heavy metals offers an enticing realm for energy-efficient memory and logic devices. The spin Hall efficiency is a key parameter in describing the generation of spin current. Recent findings have reported enhancement of spin Hall efficiency by mechanical strain, but its origin remains elusive. In this chapter, we explore the origin of the strain-mediated spin-orbit torque enhancement. Part of this chapter has been published in *ACS Nano*.[1]

5.1 Motivation

Since the demonstration of the spin Hall effect, the ability to manipulate magnetization with the use of current-induced spin-orbit torque (SOT) for energy-efficient memory and logic devices has attracted significant interest in the field of spintronics.[2-7] The spin Hall effect capitalizes on the spin-orbit interaction in nonmagnetic material to generate a pure spin current from an unpolarized charge current. In a heavy-metal/ferromagnetic layer (HM/FM) bilayer system, this results in a magnetic torque acting on the adjacent ferromagnet, thus allowing for SOT-induced magnetic switching.[8-12] Heavy metals, such as platinum (Pt), tantalum (Ta) and tungsten (W), have been widely explored due to their strong spin-orbit interaction.[4,13-17] In particular, Pt, in spite of its higher cost, has been pivotal and often seen as a benchmark in the development of spin Hall material due to its large intrinsic spin Hall conductivity, easy growth, and ease of integration into existing manufacturing processes.

As such, attempts to improve the spin Hall efficiency, $\theta_{\text{eff}} = (2e/\hbar) T_{\text{int}} \sigma_{\text{SH}} \rho_{\text{Pt}}$, of Pt have been conducted extensively by understanding and manipulating the three distinct microscopic mechanisms: the skew, the side jump, and the intrinsic scattering.[4,14,18-21] Here, e is the elementary charge, $\hbar$ is the reduced Planck's constant, and T_{int} is the spin transparency, σ_{SH} is the spin Hall conductivity and ρ_{Pt} is the electrical resistivity. To date, most of such attempts to enhance the spin Hall efficiency are focused on alloying the HM with lighter and more conductive metals,[22-30] having insertion layers within the HM[31] and the varying deposition condition of the HM.[32,33] Among the different methods used, a promising technique of enhancing the spin Hall efficiency is the use of mechanical strain. Recent works by T. Nan

et al. and E. Liu *et al.* have shown that tensile strain enhances θ_{eff} in spin Hall materials while compressive strain deteriorates it. However, the understanding behind the origin of the scattering mechanism that leads to this enhancement remains unclear and more studies are needed to deepen our understanding of the physics of flexible spintronics devices.[34,35]

In this work, we study the effects of tensile strain on θ_{eff} in Pt/Co bilayer system with the use of the spin-torque ferromagnetic resonance technique (ST-FMR) and demonstrate that the strain-induced θ_{eff} enhancement remains even after the strain has been removed. Spin transparency and X-ray absorption spectroscopy/X-ray magnetic circular dichroism (XAS/XMCD) results rule out the possibility of an improvement in the platinum/cobalt (Pt/Co) interface quality or interfacial spin-orbit interaction, thus leading us to hypothesize that the enhancement is a bulk effect in Pt. This is confirmed by the increased resistivity of Pt when strained, implying that tensile strain results in additional scattering within the Pt bulk. Furthermore, the switching current density is significantly reduced with the decrease in Gilbert damping parameter. These findings establish an understanding on how strain affects the spin-Hall generation in heavy metal and offer a very compelling justification to push the boundaries of existing spin-Hall material for low-power SOT application.

5.2 Experimental Details

The spin current generation mediated by the applied mechanical tensile strain on Pt was characterized using the spin-torque ferromagnetic resonance (ST-FMR) measurement. Figure 5-1a depicts a schematic illustration of the measurement setup and device structure with an inset showing an optical image of the device. All samples were sputter-deposited onto unstrained Kapton substrate at room temperature. As such, the initial internal stress from the fabrication of the films is the same for all samples and is thus negligible. The strain is applied thereafter the device fabrication during the device characterization process. Bilayer Pt(5 nm)/Co(5 nm) were fabricated with a 5 nm titanium (Ti) seed and capping layer for film adhesion and oxidation prevention. A photo of an as-grown Pt/Co bilayer on the Kapton substrate is shown in Figure 5-1b, demonstrating its flexibility. Here, Pt plays the role of the heavy metal (HM) layer in producing SOTs *via* spin-Hall effect.

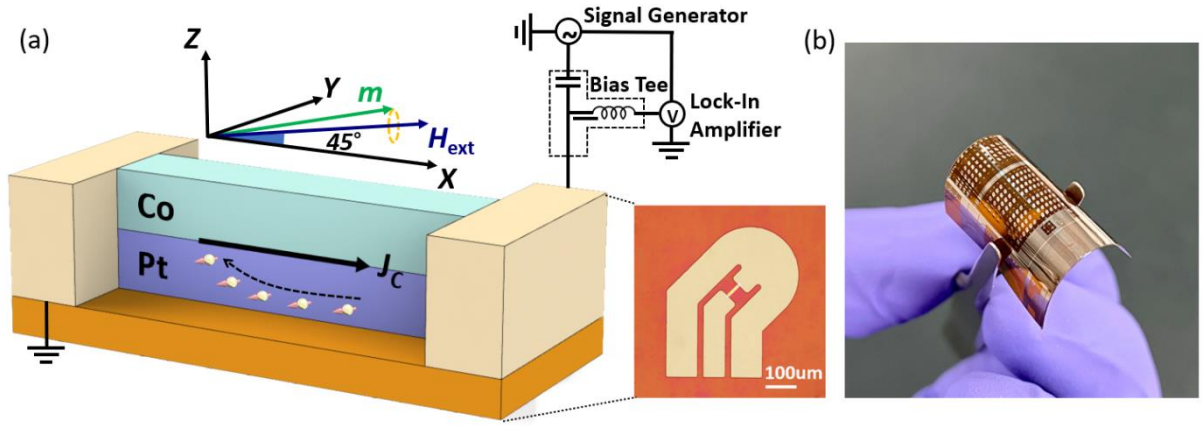

Figure 5-1 (a) Schematic illustration of Pt/Co bilayer for the ST-FMR measurement. The green and navy arrows represent the precessing magnetization in the Co layer and applied external field, respectively. A RF current was applied along the longitudinal direction (*x*-axis) of the device generating two orthogonal torques as it passes through the heavy metal. An optical image of the device is as shown in the inset. (b) Photo of an array of strained ST-FMR devices on the flexible Kapton substrate.

Figure 5-2 illustrates how the strain used in this study was applied after fabrication in two different configurations: tensile strain in the parallel and orthogonal direction to the radiofrequency (RF) current. The bending strain ε of the Kapton film in the bending direction was estimated by using $\varepsilon = t/2R$, where t and R are the total thickness of the substrate (120 μm) and bilayer structure and the curvature radius of the mold, respectively.[36] By varying the radius of curvature of the mold used, tensile strain ε of 0 to approximately 1.5 % was employed in this study. All strain used in this experiment is tensile strain if not specifically mentioned. *In-situ* strain measurements are described by ε_{in} while measurements taken after relaxing the strain are defined as ε_{post}, where ε_{post} is the magnitude of the tensile strain applied for 60 minutes before relaxing it for measurement. Plastic molds of predetermined curvature for the application of tensile strain were 3D printed using polylactic acid (PLA) filament.

The XMCD measurements were performed at the Co $L_{2,3}$ edge using circularly polarized X-rays at the Surface, Interface and Nanostructure Science (SINS) beamline of the Singapore Synchrotron Light Source.[37,38] All spectra were measured at room temperature in the total-electron-yield mode with fixed helicity of 80% circularly polarized X-rays and opposite magnetic fields up to ±1 T. The angle of incidence of the photon beam was positioned at 60° with respect to the sample surface normal. The orbital to spin magnetic moment ratio was extracted using the sum rules.

5.3 Material Characterization

X-ray diffraction (XRD) was performed on two different Pt/Co thin-film samples. The first sample is kept in pristine condition while the other was relaxed after applying a 1.5% tensile strain for 60 minutes. The XRD spectra are as presented in Figure 5-3a. After the application of strain, the Pt (111) peak makes a $0.14°$ shift to the left while Co (002) peak remains unchanged. This different behavior is due to the difference in Poisson's ratio between the two materials with Pt having a larger ratio of 0.41 while Co is 0.29.[39] The shift in Pt (111) peak suggests a change in Pt's bulk property and an increase in lattice constant due to the tensile strain. One such property change observed is the electrical resistivity (ρ_{Pt}) of Pt.

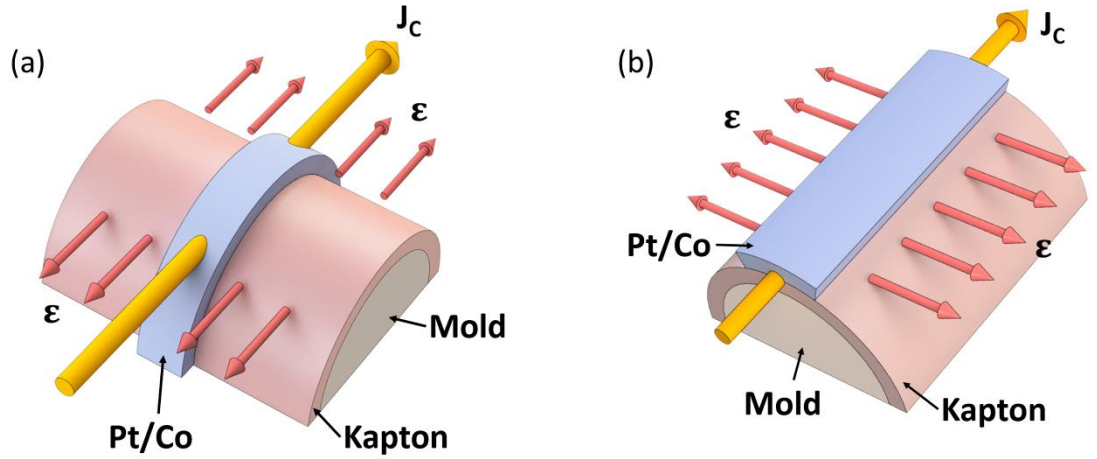

Figure 5-2 (a) Schematic of strain application onto the sample using a plastic mold in different directions. Strain in the parallel and (b) orthogonal direction as the radiofrequency current was applied during the ST-FMR measurement.

As tensile strain is applied along the longitudinal direction (x-axis) of the Pt microstrip, the stripe expands and narrows along the direction of strain. Narrowing of the stripe results in an increase in resistivity which scales with the magnitude of the strain as shown in Figure 5-3b. This change can be described by the gauge factor given by $GF = (\Delta R/R)/\varepsilon$, where $\Delta R/R$ is the relative change in resistance and ε is the applied strain.[40] For the Pt strained along the x-axis, GF is calculated to be 10.5 ± 0.5, which is consistent with previous findings.[41] Upon removing the strain, the film relaxes but the shift in lattice constant of Pt remains indicating that the enhanced resistivity is still present due to internal stress. This residual strain is speculated to be the result of a change in lattice constant and the possibility of grain rotation

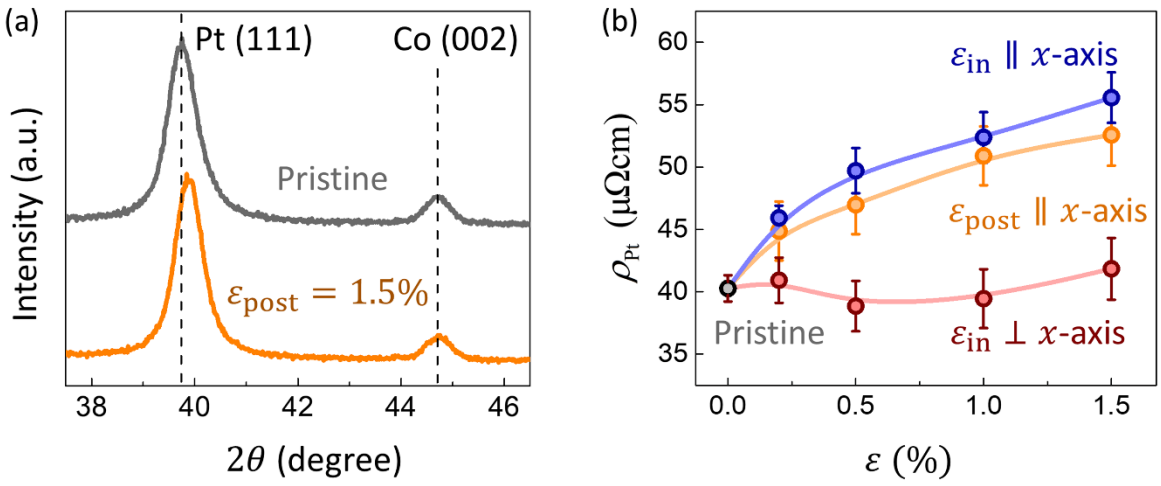

Figure 5-3 (a) X-ray diffraction pattern of 25 nm thick Pt/Co samples showing the shift between the Pt (111) to the Cu (111) peak. The pristine sample is as-deposited while the $\varepsilon_{post} = 1.5\%$ sample was strained for 60 minutes before measurement. (b) Resistivity of Pt under tensile strain ε_{in} and when the substrate is relaxed after tensile strain ε_{post} is applied.

mediated by grain boundary dislocation. The slight decrease in resistivity is caused by the relaxation of the substrate reversing the narrowing of the stripe. On the other hand, exerting strain in the transverse direction (y-axis) of the microstrip results in a less pronounced change in resistivity ρ_{Pt}.

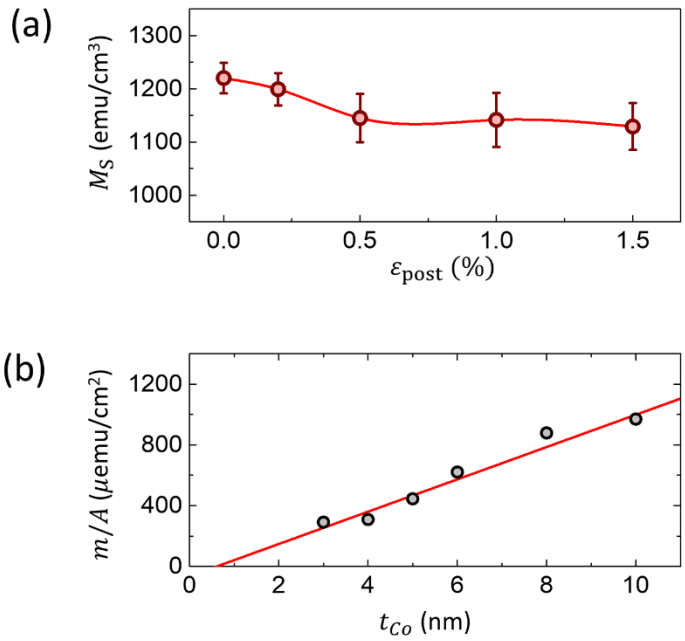

Figure 5-4 (a) Magnetization saturation of Pt (5 nm)/Co (5 nm) as a function ε_{post}. (b) Magnetic dead layer extrapolation of pristine Pt (5 nm)/Co (t_{Co} nm).

The magnetization saturation of Pt (5 nm)/Co (5 nm) bilayer slightly decreases when exposed to tensile strain ε_{post} ranging between 1220 to 1129 emu/cc as shown in Figure 5-4a. This value is consistent with other works and it shows that there is negligible magnetization contribution from the magnetic proximity effect.[42-47] In Figure 5-4b, the dead layer of Pt (5 nm)/Co (t_{Co} nm) was measured to be 0.61 ± 0.08 nm.

5.4 Spin-Torque Generation Efficiency Analysis

To systematically evaluate the effects of tensile strain in the Pt layer on the spin-torque efficiency, ST-FMR was employed for bilayer Pt/Co. During the measurement, a RF current (J_C) was injected into the coplanar waveguide and flows along the long axis of the microstrip device (10 μm × 50 μm). Simultaneously, an external magnetic field (H_{ext}) was applied at a 45°. The longitudinal RF current passing through the Pt layer generates an oscillating transverse spin current by spin Hall effect (SHE), which is then injected into the adjacent Co layer. The magnetization of Co experiences three different torques induced by the RF current: Oersted-field torque as current passes through the Co layer, field-like and damping-like torque produced by the current-induced SOT from the Pt layer. At the resonance field (H_{res}) when the microwave frequency matches the precessional frequency of the magnetization, the FMR condition is satisfied and the oscillating torques will result in the oscillation of the device resistance due to anisotropic magnetoresistance in the Co layer. The mixing of the RF current and oscillating resistance results in a rectified DC voltage signal (V_{mix}) across the device.

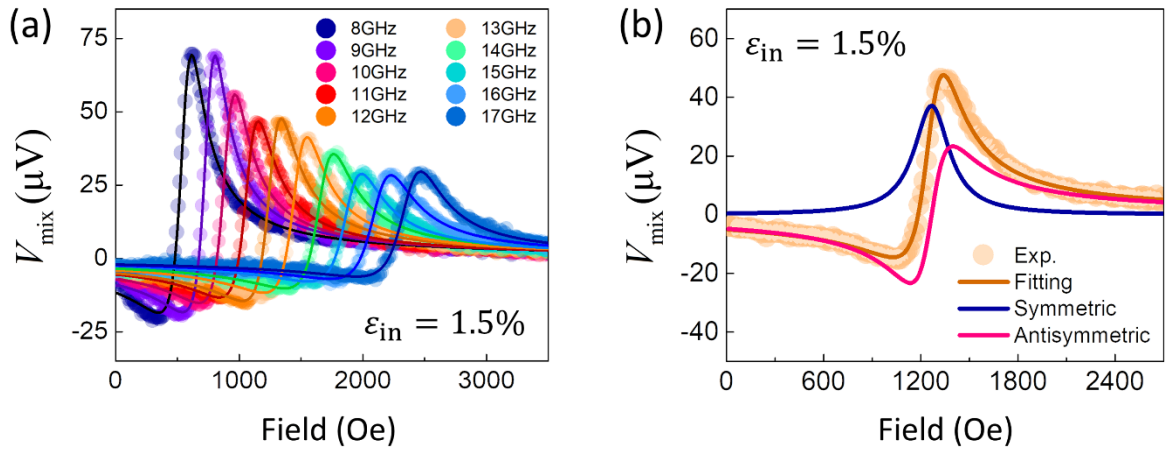

Figure 5-5 (a) Measured ST-FMR spectra of Pt/Co bilayer while applying $\varepsilon_{in} = 1.5\%$ for frequency from 8 to 17 GHz with nominal input power of 12 dBm. (b) ST-FMR Lorentzian fitting of measured V_{mix} for device with $\varepsilon_{in} = 1.5\%$ applied in the parallel direction of the 12 GHz microwave current.

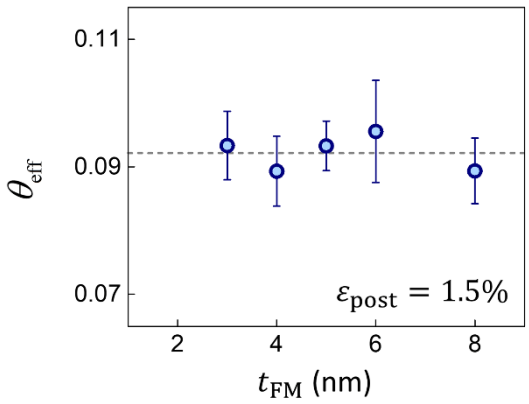

Figure 5-6 Co thickness dependence of spin Hall efficiency measured at $\varepsilon_{post} = 1.5\%$ to verify the absence of field-like torque in Pt(5 nm)/Co(t_{FM} nm) system.

Using a bias tee, V_{mix} can be measured during the microwave current application. The ST-FMR spectra of bilayer Pt/Co was measured using a microwave power of 12 dBm as shown in Figure 5-5a. A frequency range between 8 to 17 GHz in steps of 1 and the measured V_{mix} is fitted using Equation 3.8.4. The symmetric Lorentzian contribution is produced when the spin Hall torque from the generated spin current and the magnetization precession are in phase, while the antisymmetric Lorentzian contribution arise from the phase difference between the Oersted field and the field-like torque from the charge current passing through the Pt layer and the magnetization precession. Figure 5-5b shows the different Lorentz contribution of the V_{mix}.

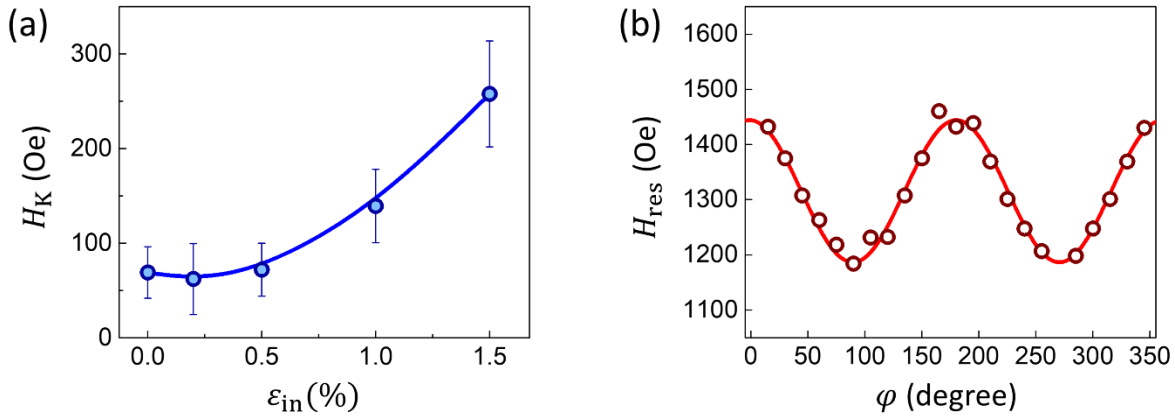

Figure 5-7 (a) Strain dependence of total magnetic anisotropy field of Pt (5 nm)/Co (5 nm). (b) Angular dependence of resonance field of pristine Pt (5 nm)/Co (5 nm), where φ is the angle between the microstrip and the external magnetic field.

The effective magnetization (M_{eff}) was obtained by an in-plane magnetization Kittel equation fitting (Equation 3.8.6) as shown in Figure 5-8a, where γ is the gyromagnetic ratio and H_K is the total magnetic anisotropy field. From Figure 5-8b, when exposed to tensile strain, M_{eff} decreases and this corresponds to an enhancement in the H_K and surface anisotropy constant (K_S) given by $K_S = 2\pi M_S t_{\text{FM}}(M_S - M_{\text{eff}})$, where M_S and t_{FM} is the saturation magnetization of Co and thickness of Co layer respectively.[26,31,42] The M_{eff} decrease observed could also be attributed to the slight decrease in the M_S and increase in strain-induced anisotropy. The total magnetic anisotropy field (H_K) of Pt/Co bilayer was obtained from fitting of the Kittel equation and its strain dependence is as shown in Figure 5-7a. Here, H_K encompasses the strain-induced anisotropy and shape anisotropy of the microstrip. As tensile strain is applied, H_K appreciates along with the K_S of the sample resulting in a decrease in M_{eff}. The large H_K when strained could also be a result of the shape anisotropy. From Figure 5-7b, the shape anisotropy is determined to be 129 ± 6 Oe.

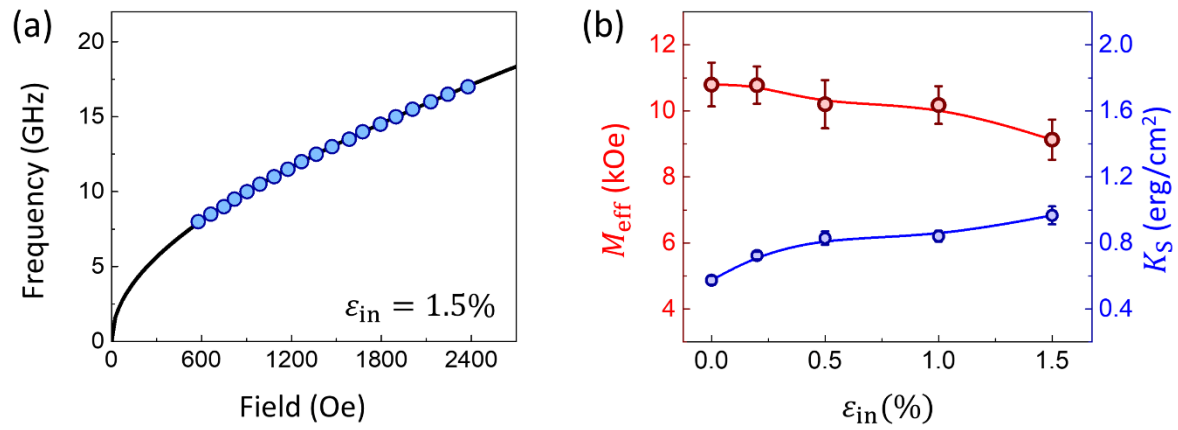

Figure 5-8 (a) Kittel fitting of Pt/Co bilayer device with $\varepsilon_{\text{in}} = 1.5\%$. (b) Strain dependence of M_{eff} and K_S for device with varying ε_{in} strain.

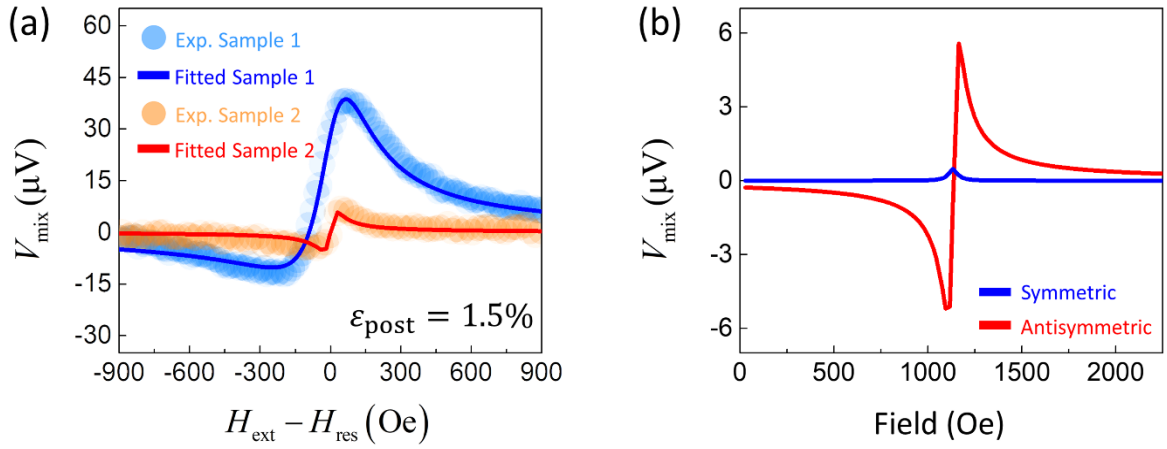

Figure 5-9 ST-FMR spectra of Sample 1 and Sample 2 which are Ti(5 nm)/Pt(5 nm)/Co(5 nm)/Ti(5 nm) and Co(5 nm)/Ti(5 nm) respectively. (b) Lorentz fitting of the symmetric and antisymmetric contribution.

The field-like torque in Pt/Co bilayer is assumed to be negligible due to the sufficiently thick Pt layer used and this is assumption is consistent with previous work for Pt.[17,48] In order to further validate the use of the lineshape analysis, we performed a Co thickness dependence study. From Equation 3.8.9 if field-like torque exists, the spin Hall efficiency will be dependent on the ferromagnetic layer thickness. However, in Figure 5-6, the θ_{eff} remains constant with the varying Co thickness indicating the absence of field-like torque in Pt/Co. The lineshape method is a widely used method to characterize spin Hall efficiency of materials with negligible field-like torque. We have demonstrated that in the case of Pt, this method of analyzing the spin Hall efficiency is adequate.

Next, the SOT contribution of the titanium (Ti) seed and capping layer is studied in order to verify its significance. A bilayer Ti/Co sample was fabricated and its ST-FMR spectra was measured. Since the thickness of Pt is greater than its spin diffusion length, the contribution coming from the Ti seed layer can be safely excluded from our analysis which allows us to focus on the capping layer. From Figure 5-9, the magnitude of the symmetric contribution is much smaller that the asymmetric contribution. Using the lineshape analysis, the spin Hall efficiency of Ti was calculated to be 0.002 ± 0.003 at $\varepsilon_{post} = 1.5\%$, which is minute compared to the contribution from Pt. This result is consistent with other works[24,49] and therefore, we conclude that the spin Hall efficiency in the samples used in this work have negligible spin Hall efficiency.

With this, the spin-Hall efficiency for the Pt/Co bilayer can be determined using the line-shape method described by the Equation 3.8.8. The illustration in Figure 5-10 establishes the different stages of the experiment. For ease of comparison, all three ST-FMR spectra of bilayer Pt/Co were normalized to its minimum value. From the line-shape equation, the magnitude of S/A is proportional to the spin Hall efficiency, which implies that a larger $V_{\text{mix}}/V_{\text{min}}$ magnitude corresponds to a larger spin Hall efficiency.

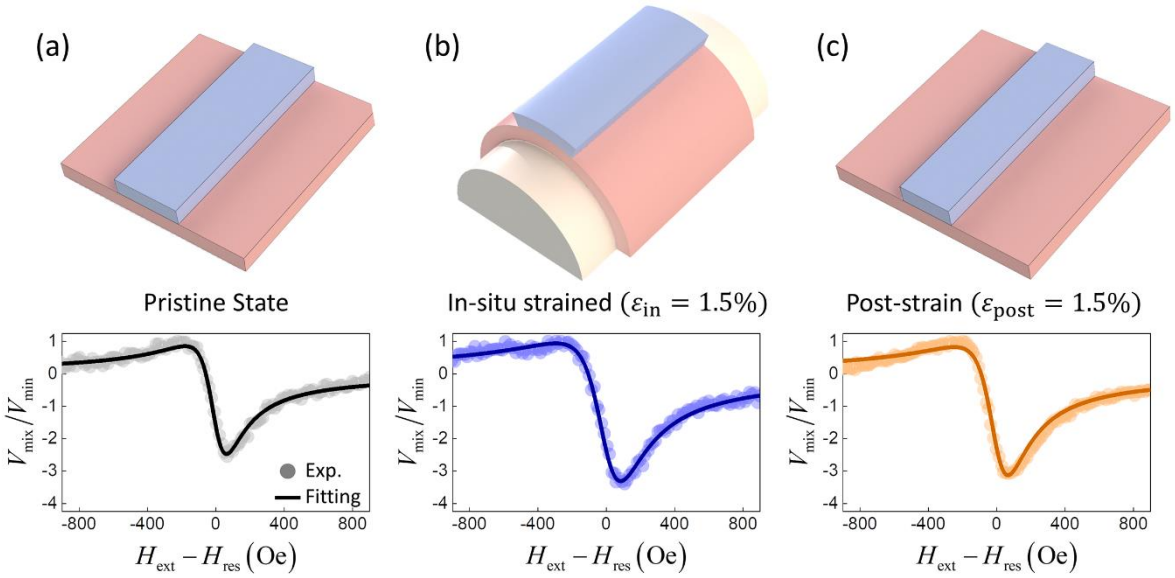

Figure 5-10 Schematic of sample and the measured ST-FMR spectra at 12 GHz at different strained conditions. The ST-FMR spectra V_{mix} are normalized to their minimum value. (a) Pristine, (b) while 1.5% strain is applied and (c) after strain is removed with the sample flattened.

Using the $V_{\text{mix}}/V_{\text{min}}$ value for the pristine Pt/Co as a benchmark in Figure 5-10a, the effects of strain on the spin Hall efficiency can be observed. At $\varepsilon_{\text{in}} = 1.5\%$, $V_{\text{mix}}/V_{\text{min}}$ increases by 36% as shown Figure 5-10b suggesting that an enhancement in the spin Hall efficiency was brought about by the strain, which was previously reported.[34,35,50] However, a more striking observation was made after the removal of the strain in Figure 5-10c, which shows that the strain-induced increment was retained. The corresponding spin Hall efficiency was calculated and is summarized in Figure 5-11 (a and b).

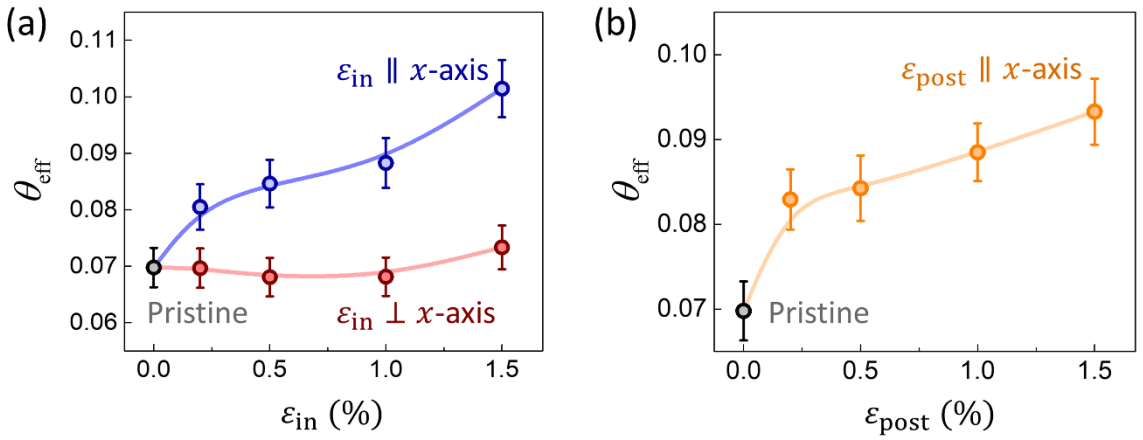

Figure 5-11 Spin-Hall efficiency as a function of (a) in-situ tensile strain ε_{in} and (b) after applying tensile strain ε_{post} for the Pt/Co bilayer.

The θ_{eff} dependence of tensile strain in the parallel and orthogonal direction to the current is shown in Figure 5-11a. Here, θ_{eff} increases proportionally with tensile strain along the direction of current. When $\varepsilon_{in} = 1.5\%$ is applied, θ_{eff} is enhanced by 45% from 0.070 ± 0.003 to 0.101 ± 0.005. Interestingly, upon removing the tensile strain in this direction, 78% of the θ_{eff} enhancement is retained giving a value of 0.093 ± 0.007 even when the substrate is flattened and relaxed as shown in Figure 5-11b. However, not all tensile strain will result in an enhancement. For the tensile strain to enhance the θ_{eff}, the direction at which the strain is applied is crucial. Applying strain in the orthogonal direction did not affect the θ_{eff} which is consistent with previous work.[34] Base on $\theta_{eff} = T \times \theta_{SH}$, where θ_{SH} is the spin Hall angle of Pt, the origin of the θ_{eff} enhancement can be categorized into either (i) an interfacial or (ii) bulk effect. To better comprehend the physics and distinguish between the two effects of strain on

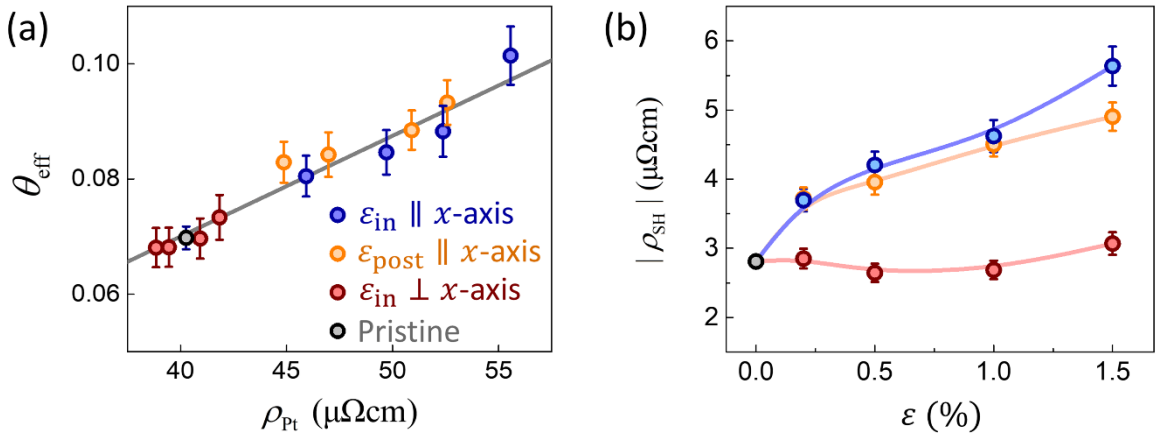

Figure 5-12 (a) Spin Hall efficiency dependence of electrical resistivity of Pt. (b) Spin Hall resistivity of Pt dependence of tensile strain.

the Pt/Co interface, spin transparency and XMCD were measured. FMR measurements were performed on Pt/Co bilayer thin film and the $\varepsilon_{\text{post}}$ strain was applied before measurement. Plotting θ_{eff} as a function of ρ_{Pt}, a linear relation is observed in Figure 5-12a. Both θ_{eff} and ρ_{Pt} increase by about 40% when $\varepsilon_{\text{in}} = 1.5\%$ is applied. However, the increase in θ_{eff} is lower than previous work reporting that the increase in resistivity will result in a much greater increase in spin Hall angle.[32] Varying pressure during film deposition affects the growth condition of the HM layer directly as compared to the use of mechanical strain. Hence, it is difficult to compare the two methods directly as their effects on the HM layer to change the resistivity are different. From Figure 5-12b, the spin Hall resistivity, $\rho_{\text{SH}} = \theta_{\text{eff}} \times \rho_{\text{Pt}}$, increases in a similar trend as θ_{eff} when strain is applied.

5.5 Gilbert Damping and Spin Transparency Analysis

Figure 5-13a linewidth shows the dependence of linewidth on the resonance frequency and from the linear regression, two magnon scattering was assumed to be negligible.[51] The decreasing gradient of the fitted line indicates a reduction in the Gilbert damping parameter as shown in the main text. Ideally, the ΔH_0 should be zero in a uniform bulk film however in the samples exposed to strain it gradually increases with the magnitude of strain applied as shown in Figure 5-13b. This suggest that there might be an increase in inhomogeneity as the film is exposed to more strain and therefore explaining the slight decrease in magnetization saturation.

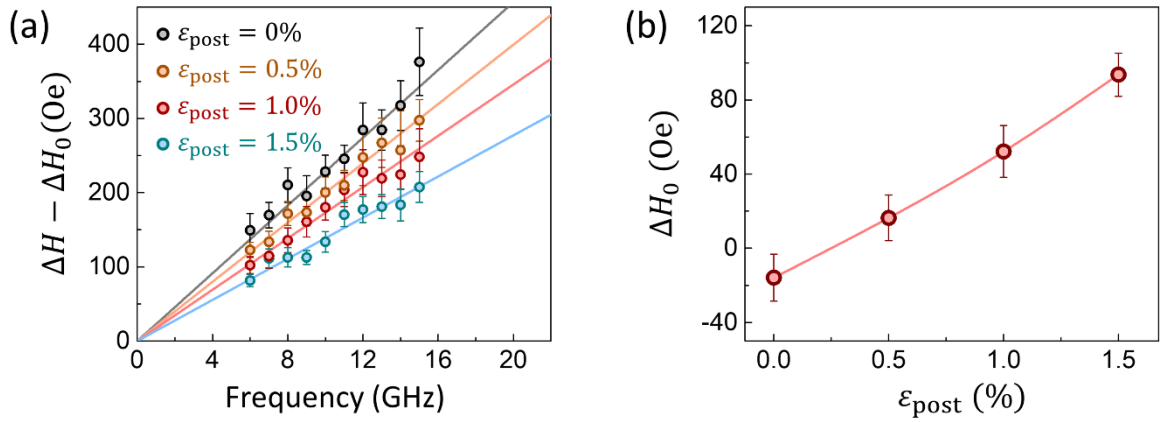

Figure 5-13 (a) Dependence of the linewidth on resonance frequency with varying ε_{post}. (b) ΔH_0 dependence of ε_{post}.

The effective Gilbert damping (α_{eff}) was calculated from the linewidth of the FMR measurement of the Pt/Co bilayer using Equation 3.8.7. The α_{eff} of Pt/Co bilayer is mainly contributed by the intrinsic Gilbert damping (α_{int}) from Co and the damping introduced by spin pumping effect (α_{SP}) due to the adjacent Pt.[52,53] A Pt thickness dependence of spin pumping induced damping was performed as shown in Figure 5-15a and their relation can be described by Equation 4.6.2.

Using the obtained α_{SP}, the two main Gilbert damping contributions are consolidated and compared in Figure 5-15b. The change in intrinsic damping from the Co is negligibly small as compared to the decrease in α_{SP}. This outcome matches our XRD result that the Co lattice constant is not affected by ε_{post}. Pt on the other hand is greatly affected by the tensile strain and since α_{SP} is heavily dependent on the interface between Pt and Co, any deterioration of the interface will translate to a decrease in α_{SP}. The effective damping drops by 40% from $(1.7 \pm 0.1) \times 10^{-3}$ to $(0.99 \pm 0.06) \times 10^{-3}$ primarily attributed to the decrease in α_{SP}.

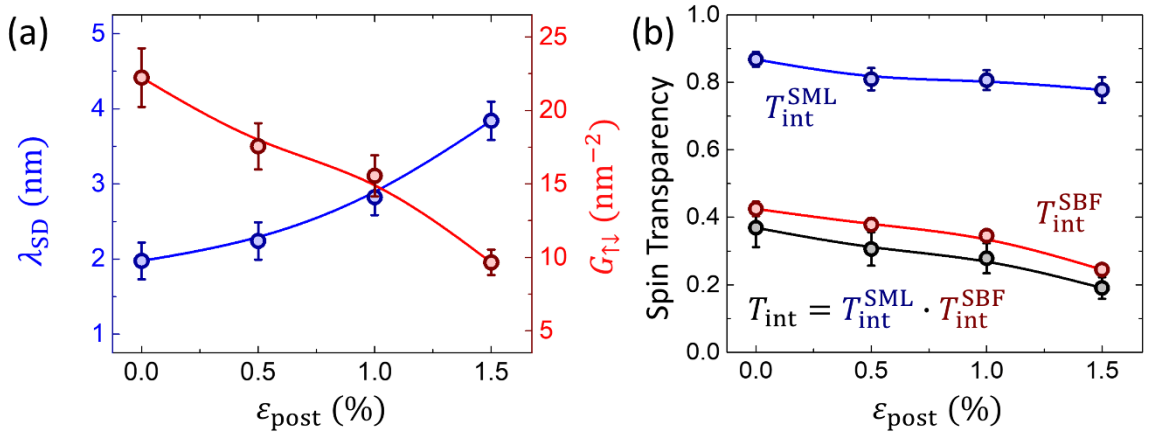

Figure 5-14 (a) λ_{SD} and $G^{\uparrow\downarrow}$ and (b) spin transparency T_{int} as a function of ε_{post} application.

From Figure 5-14a, the ε_{post} dependence of the spin diffusion length and spin-mixing conductance of Pt/Co bilayer is shown. The spin diffusion length increases inversely with the spin-mixing conductance when strain is introduced. Based on the Elliott-Yafet (EY) mechanism, an increased Pt electrical resistivity should lead to shorter spin diffusion length, however the opposite is observed. This indicates a possible decrease in interfacial spin-orbit coupling (ISOC), which was reflected from the XMCD analysis later.[54]

The interfacial intrinsic spin transparency T_{int} between a FM/HM is more often than not below unity due to two main contributing phenomena known as spin memory loss (SML) and spin backflow (SBF). SML is the interfacial spin-orbit scattering that results in a loss in spin transmission. For Pt/Co interface with in-plane magnetic anisotropy, the effects of SML on T_{int} can be approximated using $T_{int}^{SML} \approx 1 - 0.23K_S$.[31,33,55] SBF on the other hand is attributed

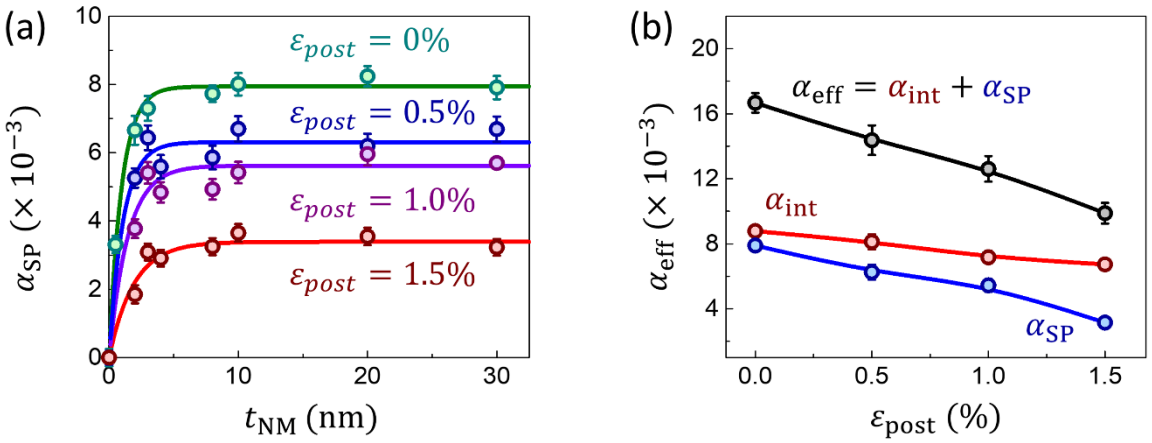

Figure 5-15 (a) Damping parameter due to spin pumping of Pt/Co bilayer with varying Pt thickness for samples after ε_{post} application. (b) α_{eff} as a function of ε_{post} application.

to the finite spin-mixing conductance at the interface and can be analyzed using the drift-diffusion model given by Equation 4.6.3.[31,33,56,57] Figure 5-14b, shows effects of tensile strain on the $T_{\text{int}}^{\text{SML}}$ and $T_{\text{int}}^{\text{SBF}}$ along with the T_{int} which can be obtained by taking the product of the two contributing factors. At $\varepsilon_{\text{post}} = 1.5\%$, the T_{int} decreases by 48% from 0.37 ± 0.06 to 0.19 ± 0.03 with majority of the effect coming from the $T_{\text{int}}^{\text{SBF}}$. The greater decline in $T_{\text{int}}^{\text{SBF}}$ as compared to $T_{\text{int}}^{\text{SML}}$ is hypothesized to be attributed by the change in interfacial spin-orbit interaction between Pt/Co interface. This decrease in T_{int} suggests that the enhancement in θ_{eff} is not a result of an improvement of the interfacial quality.

5.6 XAS/XMCD Measurement

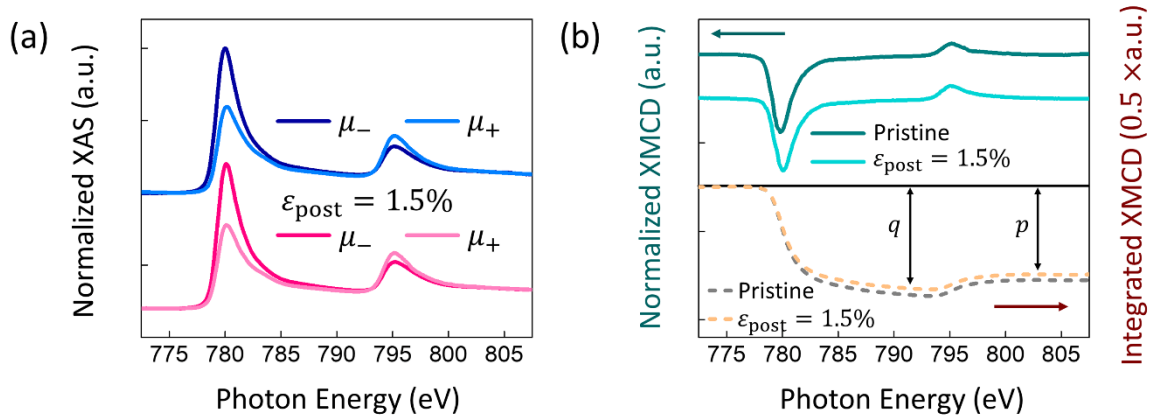

Figure 5-16 (a) Normalized XAS at the Co $L_{2,3}$ absorption edge. (b) Corresponding normalized XMCD spectra with their integrated intensities. The vertical arrows indicate the values of p and q, derived from the integrals of the dichroic signals.

To further verify that the θ_{eff} enhancement is not attributed by the interface between the Pt/Co bilayer, XAS/XMCD measurements were performed. The total electron yield intensities μ_+ and μ_- around the L_2 and L_3 edges for Co (770-810 eV) were measured at the grazing incidence as shown in Figure 5-16. By applying the sum rules to the XMCD spectra, the orbital to spin magnetic moment ratio $(m_{\text{L}}/m_{\text{S}})$ can be obtained as follows,

$$\frac{m_{\text{L}}}{m_{\text{S}}} = \frac{2q}{9p - 6q} \tag{5.6.1}$$

where p is the integral of the dichroic signal of the L_3 peak alone and q is the integrated

dichroism over both the L_2 and L_3 edges.[32,58,59] The m_L/m_S ratio of Co decreases by 22% from 0.394±0.03 to 0.304±0.02 when the strain was applied, implying a reduction in spin-orbit coupling.[60,61] This suggests that the enhancement in θ_{eff}, revealed by our spin transparency measurement, is not caused by an enhanced ISOC while the bulk effect may prevail. The decreasing trend of Co m_L/m_S ratio, upon the strain application seems to be in line with the inverse proportional relationship between λ_{SD} and ISOC.[54]

To date, it has been reported that the intrinsic scattering mechanism dominates over the extrinsic in 4d and 5d transition metals such as Pd, Pt, Ta and W.[4,14] In a non-alloyed metal such as Pt, the side jump scattering contribution can be assumed to be negligibly small as compared to the skew-scattering.[62] Therefore, the only extrinsic contribution considered in the Pt/Co system is the skew-scattering. By assuming the total spin Hall conductivity of the system to be the sum of the intrinsic and extrinsic contribution, the spin Hall resistivity can be expressed by the following equation:

$$-\rho_{SH} = \sigma_{SH}^{int}\rho_{Pt}^2 - \rho_{SH}^{SS}, \tag{5.6.2}$$

where σ_{SH}^{int} is the intrinsic spin Hall conductivity of Pt and ρ_{SH}^{SS} is the spin Hall resistivity influenced by the skew-scattering mechanism.[63,64] By plotting the $|\rho_{SH}|$ as a function of the ρ_{Pt}^2 in Figure 5-17a, σ_{SH}^{int} is found to be $1.79\pm0.05\times10^5\ (\hbar/2e)\Omega m$ which is consistent with previous reports of a value of $1.6\times10^5\ (\hbar/2e)\Omega m$.[65,66] Since there is little change to the intrinsic contribution of Pt, this implies that the source of the enhancement is contributed by extrinsic scattering. From the linear relation, σ_{SH}^{SS} is calculated to be $1.09\pm0.06\times10^5$ $(\hbar/2e)\Omega m$. Additional skew-scattering as a result of the tensile strain makes up for 38% of the total spin Hall conductivity and this is larger than previous works reporting only 28% contribution by varying the deposition condition of Pt.[62,65] Due to the nature of non-alloyed metals, the contribution from the intrinsic scattering in Pt dominates. However, the extrinsic contribution from the skew-scattering grows when tensile strain is introduced, resulting in enhanced θ_{eff}. Apart from the θ_{eff} enhancement, another benefit of the use of tensile strain is the reduction in the switching current density J_{C_0} required for an SOT device. J_{C_0} can be estimated using Equation 4.6.1. Since J_{C_0} is proportional to the ratio between α_{eff} and θ_{eff}, a

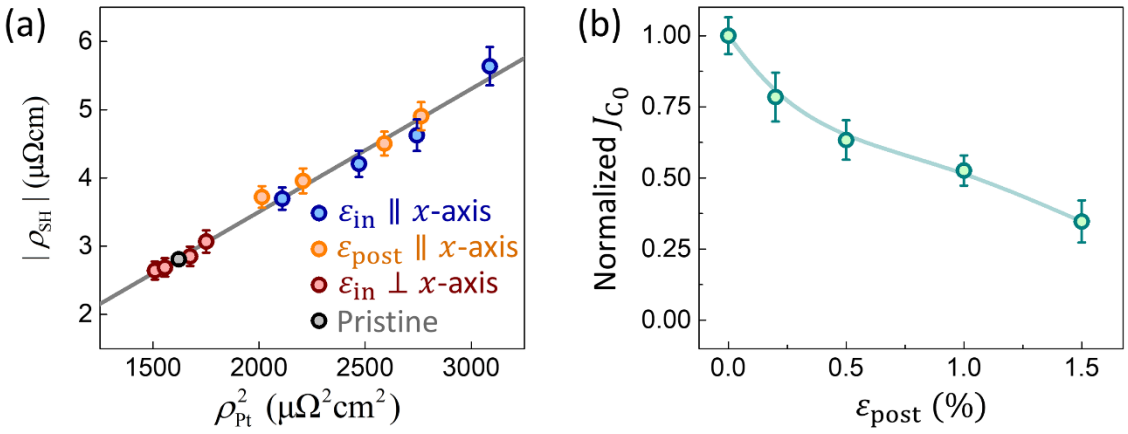

Figure 5-17 (a) Spin-Hall resistivity as a function of the squared Pt resistivity. (b) Normalized switching current density as a function of ε_{post} application.

decrease in the ratio implies a lower J_{C_0}, as shown in Figure 5-17b. At $\varepsilon_{post} = 1.5\%$, J_{C_0} decreases by 65% making tensile strain a very viable and flexible method of achieving low-power consumption SOT devices.

In summary, we have demonstrated the use of tensile strain to enhance θ_{eff} and showed that 78% of the enhancement can be retained even after removing the strain. The linear relation between the spin Hall efficiency and the resistivity of Pt hints that the enhancement is coming from the additional spin Hall effect coming from the bulk Pt layer instead of the Pt/Co interface. The results from spin transparency and XMCD measurements suggest that there were signs of deterioration in the Pt/Co interface quality and slight reduction in the spin-orbit coupling. This implies that it is unlikely that the interface contributed to the enhancement. Analyzing the relationship between resistivity and spin Hall efficiency relation, it was identified that the strain-mediated enhancement was due to additional extrinsic spin Hall effect, which occurred within the bulk Pt layer. With strain treatment, the spin Hall angle, $\theta_{SH} = \theta_{eff}/T_{int}$, of Pt could potentially be much greater than previously reported value of ~0.30 after accounting for the spin transparency at $\varepsilon_{post} = 1.5\%$.[67] Moreover, the J_{C_0} required is drastically reduced due to the decrease in the $\alpha_{eff}/\theta_{eff}$ ratio. Our findings will aid with the development of power efficient and flexible spintronics devices through mechanical strain engineering. Directional control of strain during application plays a critical role in the device functionality and one potential approach includes the use of micro-electromechanical system (MEMS) and origami architected microbots which can guide strains in a specific direction.

Reference

1 G.D.H. Wong, Z. Xu, W.L. Gan, C.C.I. Ang, W.C. Law, J. Tang, W. Zhang, P.K.J. Wong, X. Yu, F. Xu, A.T.S. Wee, C.S. Seet & W.S. Lew. Strain-Mediated Spin–Orbit Torque Enhancement in Pt/Co on Flexible Substrate. *ACS Nano* **15**, 8319-8327, doi:10.1021/acsnano.0c09404 (2021).

2 Y.K. Kato, R.C. Myers, A.C. Gossard & D.D. Awschalom. Observation of the spin Hall effect in semiconductors. *Science* **306**, 1910-1913 (2004).

3 J. Wunderlich, B. Kaestner, J. Sinova & T. Jungwirth. Experimental observation of the spin-Hall effect in a two-dimensional spin-orbit coupled semiconductor system. *Physical Review Letters* **94**, 047204 (2005).

4 T. Tanaka, H. Kontani, M. Naito, T. Naito, D.S. Hirashima, K. Yamada & J. Inoue. Intrinsic spin hall effect and orbital Hall effect in 4 d and 5 d transition metals. *Physical Review B* **77**, 165117 (2008).

5 G.-Y. Guo, S. Murakami, T.-W. Chen & N. Nagaosa. Intrinsic spin Hall effect in platinum: First-principles calculations. *Physical Review Letters* **100**, 096401 (2008).

6 E. Saitoh, M. Ueda, H. Miyajima & G. Tatara. Conversion of spin current into charge current at room temperature: Inverse spin-Hall effect. *Applied Physics Letters* **88**, 182509 (2006).

7 T. Kimura, Y. Otani, T. Sato, S. Takahashi & S. Maekawa. Room-temperature reversible spin Hall effect. *Physical Review Letters* **98**, 156601 (2007).

8 S. Emori, U. Bauer, S.-M. Ahn, E. Martinez & G.S. Beach. Current-driven dynamics of chiral ferromagnetic domain walls. *Nature Materials* **12**, 611-616 (2013).

9 Z. Xu, G.D.H. Wong, J. Tang, E. Liu, W.L. Gan, F. Xu & W.S. Lew. Giant Spin Hall Effect in Cu-Tb Alloy Thin Films. *ACS Applied Materials & Interfaces* (2020).

10 S. Valenzuela & M. Tinkham. Electrical detection of spin currents: The spin-current induced Hall effect. *Journal of Applied Physics* **101**, 09B103 (2007).

11 J. Hirsch. Spin hall effect. *Physical Review Letters* **83**, 1834 (1999).

12 S. Zhang. Spin Hall effect in the presence of spin diffusion. *Physical Review Letters* **85**, 393 (2000).

13 X. Tao, Q. Liu, B. Miao, R. Yu, Z. Feng, L. Sun, B. You, J. Du, K. Chen & S. Zhang. Self-consistent determination of spin Hall angle and spin diffusion length in Pt and Pd: The role of the interface spin loss. *Science Advances* **4**, eaat1670 (2018).

14 M. Morota, Y. Niimi, K. Ohnishi, D. Wei, T. Tanaka, H. Kontani, T. Kimura & Y. Otani. Indication of intrinsic spin Hall effect in 4 d and 5 d transition metals. *Physical Review B* **83**, 174405 (2011).

15 C.-F. Pai, L. Liu, Y. Li, H. Tseng, D. Ralph & R. Buhrman. Spin transfer torque devices utilizing the giant spin Hall effect of tungsten. *Applied Physics Letters* **101**, 122404 (2012).

16 L. Liu, C.-F. Pai, Y. Li, H. Tseng, D. Ralph & R. Buhrman. Spin-torque switching with the giant spin Hall effect of tantalum. *Science* **336**, 555-558 (2012).

17 L. Liu, T. Moriyama, D. Ralph & R. Buhrman. Spin-torque ferromagnetic resonance induced by the spin Hall effect. *Physical Review Letters* **106**, 036601 (2011).

18 J. Smit. The spontaneous Hall effect in ferromagnetics II. *Physica* **24**, 39-51 (1958).

19 L. Berger. Side-jump mechanism for the Hall effect of ferromagnets. *Physical Review B* **2**, 4559 (1970).

20 R. Karplus & J. Luttinger. Hall effect in ferromagnetics. *Physical Review* **95**, 1154 (1954).

21 J. Sinova, D. Culcer, Q. Niu, N. Sinitsyn, T. Jungwirth & A.H. MacDonald. Universal intrinsic spin Hall effect. *Physical Review Letters* **92**, 126603 (2004).

22 R. Ramaswamy, Y. Wang, M. Elyasi, M. Motapothula, T. Venkatesan, X. Qiu & H. Yang. Extrinsic spin Hall effect in $Cu_{1-x}Pt_x$. *Physical Review Applied* **8**, 024034 (2017).

23 G.D.H. Wong, W.L. Law, F.N. Tan, W.L. Gan, C.C.I. Ang, Z. Xu, C.S. Seet & W.S. Lew. Thermal behavior of spin-current generation in Pt_xCu_{1-x} devices characterized through spin-torque ferromagnetic resonance. *Scientific reports* **10**, 1-8 (2020).

24 L. Zhu, D.C. Ralph & R.A. Buhrman. Enhancement of spin transparency by interfacial alloying. *Physical Review B* **99**, 180404 (2019).

25 A. Fert & P.M. Levy. Spin Hall effect induced by resonant scattering on impurities in metals. *Physical Review Letters* **106**, 157208 (2011).

26 M.-H. Nguyen, M. Zhao, D. Ralph & R. Buhrman. Enhanced spin Hall torque efficiency in $Pt_{100-x}Al_x$ and $Pt_{100-x}Hf_x$ alloys arising from the intrinsic spin Hall effect. *Applied Physics Letters* **108**, 242407 (2016).

27 P. Laczkowski, J.-C. Rojas-Sánchez, W. Savero-Torres, H. Jaffrès, N. Reyren, C. Deranlot, L. Notin, C. Beigné, A. Marty & J.-P. Attané. Experimental evidences of a large extrinsic spin Hall effect in AuW alloy. *Applied Physics Letters* **104**, 142403 (2014).

28 D. Qu, S. Huang, G. Guo & C. Chien. Inverse spin Hall effect in Au_xTa_{1-x} alloy films. *Physical Review B* **97**, 024402 (2018).

29 C.Y. Hu & C.F. Pai. Benchmarking of Spin–Orbit Torque Switching Efficiency in Pt Alloys. *Advanced Quantum Technologies* **3**, 2000024 (2020).

30 Y. Niimi, Y. Kawanishi, D. Wei, C. Deranlot, H. Yang, M. Chshiev, T. Valet, A. Fert & Y. Otani. Giant spin Hall effect induced by skew scattering from bismuth impurities inside thin film CuBi alloys. *Physical Review Letters* **109**, 156602 (2012).

31 L. Zhu & R. Buhrman. Maximizing Spin-Orbit-Torque Efficiency of Pt/Ti Multilayers: Trade-Off Between Intrinsic Spin Hall Conductivity and Carrier Lifetime. *Physical Review Applied* **12**, 051002 (2019).

32 J.W. Lee, Y.-W. Oh, S.-Y. Park, A.I. Figueroa, G. Van Der Laan, G. Go, K.-J. Lee & B.-G. Park. Enhanced spin-orbit torque by engineering Pt resistivity in Pt/Co/Al O x structures. *Physical Review B* **96**, 064405 (2017).

33 M.-H. Nguyen, D. Ralph & R. Buhrman. Spin torque study of the spin Hall conductivity and spin diffusion length in platinum thin films with varying resistivity. *Physical Review Letters* **116**, 126601 (2016).

34 E. Liu, T. Fache, D. Cespedes-Berrocal, Z. Zhang, S. Petit-Watelot, S. Mangin, F. Xu & J.-C. Rojas-Sánchez. Strain-Enhanced Charge-to-Spin Conversion in Ta/Fe/Pt Multilayers Grown on Flexible Mica Substrate. *Physical Review Applied* **12**, 044074 (2019).

35 M. Filianina, J.-P. Hanke, K. Lee, D.-S. Han, S. Jaiswal, A. Rajan, G. Jakob, Y. Mokrousov & M. Kläui. Electric-field control of spin-orbit torques in perpendicularly magnetized W/CoFeB/MgO films. *Physical Review Letters* **124**, 217701 (2020).

36 Z. Zhang, E. Liu, W. Zhang, P.K.J. Wong, Z. Xu, F. Hu, X. Li, J. Tang, A.T.S. Wee & F. Xu. Mechanical Strain Manipulation of Exchange Bias Field and Spin Dynamics in FeCo/IrMn Multilayers Grown on Flexible Substrates. *ACS Applied Materials & Interfaces* **11**, 8258-8265 (2019).

37 X. Yu, O. Wilhelmi, H.O. Moser, S.V. Vidyaraj, X. Gao, A.T. Wee, T. Nyunt, H. Qian & H. Zheng. New soft X-ray facility SINS for surface and nanoscale science at SSLS. *Journal of Electron Spectroscopy and Related Phenomena* **144**, 1031-1034 (2005).

38 X. Yu, X. Chi, A. Wee, A. Rusydi & M. Breese. A scripting LabVIEW based program for experiment automation in synchrotron radiation applications. *Review of Scientific Instruments* **90**, 103902 (2019).

39 M. De Jong, W. Chen, T. Angsten, A. Jain, R. Notestine, A. Gamst, M. Sluiter, C.K. Ande, S. Van Der Zwaag & J.J. Plata. Charting the complete elastic properties of inorganic crystalline compounds. *Scientific Data* **2**, 1-13 (2015).

40 Y.-Z. Zhang, K.H. Lee, D.H. Anjum, R. Sougrat, Q. Jiang, H. Kim & H.N. Alshareef. MXenes stretch hydrogel sensor performance to new limits. *Science Advances* **4**, eaat0098 (2018).

41 S. Fricke, A. Friedberger, G. Mueller, H. Seidel & U. Schmid. in *SENSORS, 2008 IEEE.* 1532-1535 (IEEE).

42 H. Bouloussa, R. Ramaswamy, Y. Roussigné, A. Stashkevich, H. Yang, M. Belmeguenai & S. Chérif. Pt concentration dependence of the interfacial Dzyaloshinskii–Moriya interaction, the Gilbert damping parameter and the magnetic anisotropy in Py/Cu1− xPtx systems. *Journal of Physics D: Applied Physics* **52**, 055001 (2018).

43 J. Geissler, E. Goering, M. Justen, F. Weigand, G. Schütz, J. Langer, D. Schmitz, H. Maletta & R. Mattheis. Pt magnetization profile in a Pt/Co bilayer studied by resonant magnetic x-ray reflectometry. *Physical Review B* **65**, 020405 (2001).

44 T. Koyama, Y. Guan, Y. Hibino, M. Suzuki & D. Chiba. Magnetization switching by spin-orbit torque in Pt with proximity-induced magnetic moment. *Journal of Applied Physics* **121**, 123903 (2017).

45 S. Ferrer, J. Alvarez, E. Lundgren, X. Torrelles, P. Fajardo & F. Boscherini. Surface x-ray diffraction from Co/Pt(111) ultrathin films and alloys: Structure and magnetism. *Physical Review B* **56**, 9848 (1997).

46 T. White, T. Bailey, M. Pierce & C.W. Miller. Strong Spin Pumping in Permalloy-Iridium Heterostructures. *IEEE Magnetics Letters* **8**, 1-4 (2017).

47 L. Zhu, D. Ralph & R. Buhrman. Irrelevance of magnetic proximity effect to spin-orbit torques in heavy-metal/ferromagnet bilayers. *Physical Review B* **98**, 134406 (2018).

48 W. Skowroński, Ł. Karwacki, S. Ziętek, J. Kanak, S. Łazarski, K. Grochot, T. Stobiecki, P. Kuświk, F. Stobiecki & J. Barnaś. Determination of Spin Hall Angle in Heavy-Metal/Co− Fe− B-Based Heterostructures with Interfacial Spin-Orbit Fields. *Physical Review Applied* **11**, 024039 (2019).

49 H. An, S. Haku, Y. Kanno, H. Nakayama, H. Maki, J. Shi & K. Ando. Manipulation of Spin-Torque Generation Using Ultrathin Au. *Physical Review Applied* **9**, 064016 (2018).

50 T. Nan, J.M. Hu, M. Dai, S. Emori, X. Wang, Z. Hu, A. Matyushov, L.Q. Chen & N. Sun. A Strain-Mediated Magnetoelectric-Spin-Torque Hybrid Structure. *Advanced Functional Materials* **29**, 1806371 (2019).

51 R. Arias & D. Mills. Extrinsic contributions to the ferromagnetic resonance response of ultrathin films. *Physical Review B* **60**, 7395 (1999).

52 O. Mosendz, V. Vlaminck, J. Pearson, F. Fradin, G. Bauer, S. Bader & A. Hoffmann. Detection and quantification of inverse spin Hall effect from spin pumping in permalloy/normal metal bilayers. *Physical Review B* **82**, 214403 (2010).

53 J.M. Shaw, H.T. Nembach & T.J. Silva. Determination of spin pumping as a source of linewidth in sputtered Co 90 Fe 10/Pd multilayers by use of broadband ferromagnetic resonance spectroscopy. *Physical Review B* **85**, 054412 (2012).

54 L. Ma, L. Lang, J. Kim, Z. Yuan, R. Wu, S. Zhou & X. Qiu. Spin diffusion length and spin Hall angle in $Pd_{1-x}Pt_x$/YIG heterostructures: Examination of spin relaxation mechanism. *Physical Review B* **98**, 224424 (2018).

55 L. Zhu, D. Ralph & R. Buhrman. Spin-orbit torques in heavy-metal–ferromagnet bilayers with varying strengths of interfacial spin-orbit coupling. *Physical Review Letters* **122**, 077201 (2019).

56 Y.-T. Chen, S. Takahashi, H. Nakayama, M. Althammer, S.T. Goennenwein, E. Saitoh & G.E. Bauer. Theory of spin Hall magnetoresistance. *Physical Review B* **87**, 144411 (2013).

57 P.M. Haney, H.-W. Lee, K.-J. Lee, A. Manchon & M.D. Stiles. Current induced torques and interfacial spin-orbit coupling: Semiclassical modeling. *Physical Review B* **87**, 174411 (2013).

58 C. Chen, Y. Idzerda, H.-J. Lin, N. Smith, G. Meigs, E. Chaban, G. Ho, E. Pellegrin & F. Sette. Experimental confirmation of the X-ray magnetic circular dichroism sum rules for iron and cobalt. *Physical Review Letters* **75**, 152 (1995).

59 A. Hrabec, F. Gonçalves, C. Spencer, E. Arenholz, A. N'Diaye, R. Stamps & C.H. Marrows. Spin-orbit interaction enhancement in permalloy thin films by Pt doping. *Physical Review B* **93**, 014432 (2016).

60 X. Qiu, K. Narayanapillai, Y. Wu, P. Deorani, D.-H. Yang, W.-S. Noh, J.-H. Park, K.-J. Lee, H.-W. Lee & H. Yang. Spin–orbit-torque engineering via oxygen manipulation. *Nature Nanotechnology* **10**, 333-338 (2015).

61 C. Nistor, T. Balashov, J. Kavich, A.L. Rizzini, B. Ballesteros, G. Gaudin, S. Auffret, B. Rodmacq, S. Dhesi & P. Gambardella. Orbital moment anisotropy of Pt/Co/AlO_x heterostructures with strong Rashba interaction. *Physical Review B* **84**, 054464 (2011).

62 M. Isasa, E. Villamor, L.E. Hueso, M. Gradhand & F. Casanova. Temperature dependence of spin diffusion length and spin Hall angle in Au and Pt. *Physical Review B* **91**, 024402 (2015).

63 S. Onoda, N. Sugimoto & N. Nagaosa. Intrinsic versus extrinsic anomalous Hall effect in ferromagnets. *Physical Review Letters* **97**, 126602 (2006).

64 N. Sinitsyn. Semiclassical theories of the anomalous Hall effect. *Journal of Physics: Condensed Matter* **20**, 023201 (2007).

65 E. Sagasta, Y. Omori, M. Isasa, M. Gradhand, L.E. Hueso, Y. Niimi, Y. Otani & F. Casanova. Tuning the spin Hall effect of Pt from the moderately dirty to the superclean regime. *Physical Review B* **94**, 060412 (2016).

66 L. Wang, R. Wesselink, Y. Liu, Z. Yuan, K. Xia & P.J. Kelly. Giant room temperature interface spin Hall and inverse spin Hall effects. *Physical Review Letters* **116**, 196602 (2016).

67 C.-F. Pai, Y. Ou, L.H. Vilela-Leão, D. Ralph & R. Buhrman. Dependence of the efficiency of spin Hall torque on the transparency of Pt/ferromagnetic layer interfaces. *Physical Review B* **92**, 064426 (2015).

Chapter 6 Reversible Strain-Induced Spin-Orbit Torque

Strain-induced spin-orbit torque is an enticing method to enhance the spin current generation in SOT devices, however, the ability to control and tune this enhancement remains elusive. In order to fully harness the potential of this enhancement technique, more needs to be done to understand and provide a means to control the enhancement. In this chapter, we propose the use of mechanical strain and mild annealing to achieve reversible modulation of spin-orbit torque and Gilbert damping parameter. Part of this chapter has been published in *Applied Physics Letters*.[1]

6.1 Motivation

The ability to manipulate magnetization has helped the current-induced spin-orbit torque (SOT) gather a considerable amount of interest in recent decades.[2-7] SOT is induced by a pure spin current that is generated as the result of spin-orbit interaction when a charge current passes through non-magnetic metal.[7,8] In heavy-metal/ferromagnetic (HM/FM) heterostructures, the SOT is contributed by two established phenomena: the spin Hall effect in the HM and/or the Rashba–Edelstein effect at the HM/FM interface.[9-12] The spin Hall efficiency θ_{eff} is commonly used to quantify the performance of this charge-to-spin conversion and it is ideal to have a large θ_{eff} for better energy-efficient memory. To date, most studies are concentrated around HM with strong spin-orbit coupling (SOC) such as Pt, β-Ta and β-W, topological insulators and even antiferromagnetic material.[13-22]

To further push the boundaries of the θ_{eff}, many efforts have been devoted to manipulating the extrinsic contribution of the spin Hall effect (SHE). Such works include alloying of the HM with lighter conductive metals, usage of insertion layers within the HM and the varying deposition condition of the HM and many others.[23-33] The extrinsic SHE mechanism capitalizes on electron scattering caused by impurities within the HM and the two most prominent scattering processes are skew scattering and side-jump scattering.[34,35] Although the θ_{eff} can be easily enhanced through tuning the resistivity of the HM, its manipulation after the device fabrication is irreversible.[26-28] Among them, the use of mechanical strain is a promising candidate for not only enhancing the θ_{eff}, but also for tunning it reversibly.[36-38] Previous works have demonstrated SOT enhancement with the use of strain,[42]

however, the ability to revert the enhancement has yet to be demonstrated and research is required to further develop the use of mechanical strain into a feasible option for the manipulation of the SOT.

In this work, we demonstrate the ability to manipulate the strain-mediated SOT enhancement reversibly in Pt/Co using a combination of mechanical strain and mild annealing. By annealing Pt/Co at mild temperature, the internal strain induced by mechanical tensile strain is alleviated and this has been confirmed using X-ray diffraction (XRD). When the internal strain is removed, the device behaves similarly to its pristine state making further manipulation of the device possible. The generated spin current was characterized using the spin-torque ferromagnetic resonance technique (ST-FMR) and the Gilbert damping parameter of Pt/Co was found to behave inversely with the manipulated SOT. Furthermore, using mechanical tensile strain, the resonance field of Pt/Co devices can be tuned allowing for microwave detection applications. These findings establish a unique technique to influence the strain-mediated SOT and have a considerable contribution to the development of flexible spintronics devices.

6.2 Experimental Details

The effects of tensile strain and mild annealing on the spin current generation of Pt/Co bilayers are characterized using the spin-torque ferromagnetic resonance (ST-FMR) measurement. The bilayer Pt(5 nm)/Co(5 nm) films used in this study were deposited using magnetron sputtering onto unstrained flexible Kapton at room temperature using an Ar pressure of 2 mTorr and a base pressure lower than 5×10^{-8} Torr. Ti(5 nm) seed and cap layer were used for film adhesion and oxidation prevention and from previous study, it was shown that Ti does not contribute to spin current generation.[38] Within the bilayer, Pt takes up the role of the SOT generation via SHE due to its strong SOC. ST-FMR devices and coplanar waveguides (CPW) were patterned using optical lithography. Figure 6-1 illustrates the ST-FMR measurement setup and device. During the ST-FMR measurement, a microwave radiofrequency (RF) charge current (J_C) is injected into the CPW and along the longitudinal direction of the microstrip device (10 μm × 50 μm). Simultaneously, an in-plane external magnetic field (H_{ext}) is applied at a 45° angle with respect to the longitudinal direction of the device. The RF current passing through the Pt layer generates an oscillating transverse spin current by SHE, which will then enter the adjacent Co layer. The magnetization of the Co layer experiences an in-plane and out-

of-plane torque from the RF current.[17,18] When the RF spin current frequency matches the precessional frequency of the magnetization, the FMR is established, and the oscillating torques will result in the oscillation of the device resistance due to anisotropic magnetoresistance in the Co layer. By using a bias tee, the mixing of the RF current and oscillating resistance is measured as a rectified DC voltage signal (V_{mix}).

The magnitude of the strain ε was approximated using $\varepsilon = T/2R$, where T and R are the total thickness of the substrate (120 μm) and bilayer structure, and the curvature radius of the mold, respectively.[39] All strains used in this work are mechanical tensile strain and the direction of the strain is along the longitudinal direction of the microstrip. Two methods of strain measurement were used. The first is the strain treatment, where the sample is strained at a specific $\varepsilon_{\mathrm{post}}$ for 1 hr and measured at its relaxed state, while the second is an in-situ strain measurement where the sample is strained at $\varepsilon_{\mathrm{in}}$ during measurement.

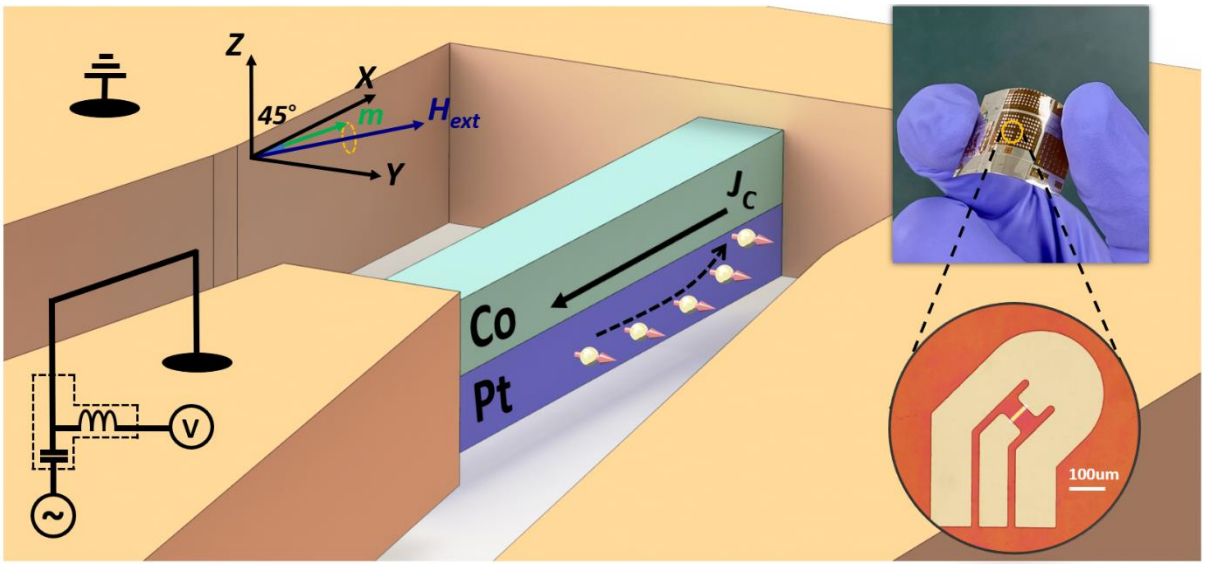

Figure 6-1 Schematic illustration of Pt/Co bilayer device for the ST-FMR measurement. The green and navy-blue arrows represent the precessing magnetization in the Co layer and applied external field, respectively. An RF current was applied along the longitudinal direction (x-axis) of the device generating two orthogonal torques as it passes through the heavy metal. Photo of strained ST-FMR devices on flexible Kapton substrate and optical image of the device is as shown in the inset.

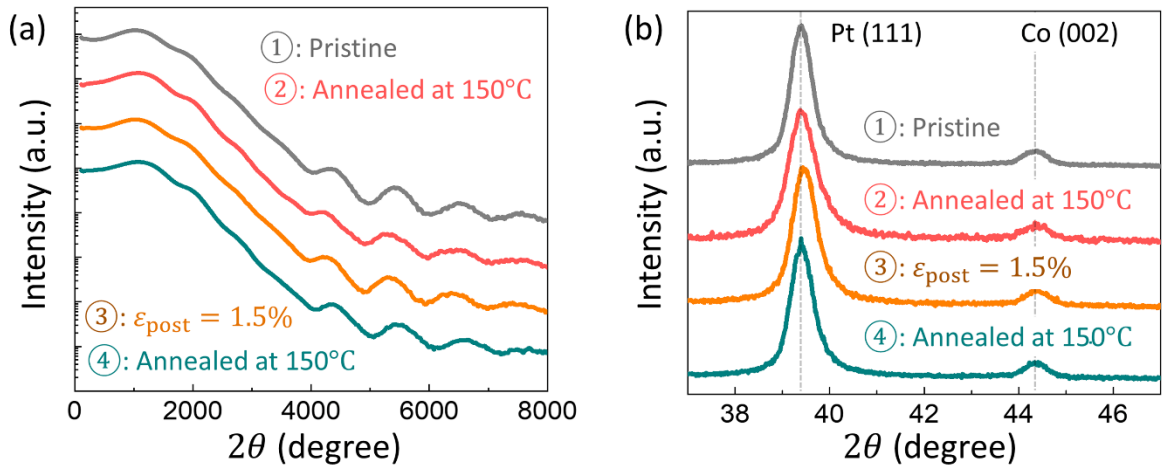

Figure 6-2 (a) X-ray reflectivity profiles for Pt(5 nm)/Co(10 nm) films at different steps of the process: step ① is the pristine film, step ② is the pristine film annealed at 150°C for 1 hr, step ③ is the tensile strain treatment of $\varepsilon_{post} = 1.5\%$ for 1 hr and step ④ is the annealing process at 150°C for 1 hr. (b) X-ray diffraction spectra of Pt(25 nm)/Co(25 nm) films demonstrating a right shift in Pt (111) peak shift when strained and back when treated with mild annealing. The Pt (111) peak location for steps ①, ②, ③ and ④ are 39.396, 39.397, 39.468 and 39.396 respectively.

Table 6-1 The interfacial roughness of Pt and Co layer within Pt(5 nm)/Co(10 nm) bilayer on Kapton substrate at different *N* steps measuring using X-ray reflectivity (XRR) spectroscopy.

Step (*N*)	Co roughness (nm)	Pt roughness (nm)	Description
1	0.80	1.43	Pristine
2	0.76	1.46	Annealed at 150°C for 1 hr
3	0.81	1.42	$\varepsilon_{post} = 1.5\%$ for 1 hr
4	0.77	1.51	Relaxed and annealed at 150°C for 1 hr

The X-ray reflectivity (XRR) spectroscopy of Pt(5 nm)/Co(10 nm) bilayer was measured and the interfacial results are as shown in Table 6-1. Annealing and straining the film has negligible impact on the interfacial roughness of Pt/Co.[40] This indicates that the interface spin-orbit scattering does not contribute to the enhancement spin-orbit torque but rather the extrinsic spin Hall effect from the change in Pt resistivity and this is consistent with previous finding.[41]

6.3 Material Characterization

X-ray reflectivity (XRR) spectroscopy was performed on Pt(5 nm)/Co(10 nm) at different steps of the characterization process to determine the effects of strain and mild annealing on the interfacial roughness between Pt and Co. The sample used throughout the different step processes is the same and the spectra are shown in Figure 6-2(a). The different steps of the process are: step ① is where the film is pristine and this is used as a reference, step ② is the pristine film after being vacuum annealed at 150°C for 1 hr, step ③ is the annealed film treated with a tensile strain of $\varepsilon_{\text{post}} = 1.5\%$ for 1 hr and step ④ is the strain-treated film after annealing at 150°C for 1 hr. From the XRR measurements (see the Supplementary Material), no significant change in interfacial roughness was observed and this concurs with previous study that strain-mediated SOT enhancement is a bulk effect due to the extrinsic SHE.[40,41] X-ray diffraction measurement was also performed on Pt(25 nm)/Co(25 nm) films for step ①, ②, ③, and ④. Similar to the XRR measurement, the XRD sample used for all four steps is the same. From Figure 6-2(b), the Pt(111) peak shifts right after the strain treatment indicating that internal strain persists within the film even after the strain has been removed. However, upon treating the film with mild annealing, the Pt(111) peak shifted back. This demonstrates the use of annealing as a means to relieve the residual internal strain-induced and suggests that the strain-mediated SOT enhancement can be reversed. Unlike the Pt (111) peak, the Co(002) peak remains stationary and this difference in response found in the Co and Pt layer is due to their different Poison's ratio.[42] This implies that the Co layer is unaffected by both the strain and mild annealing.

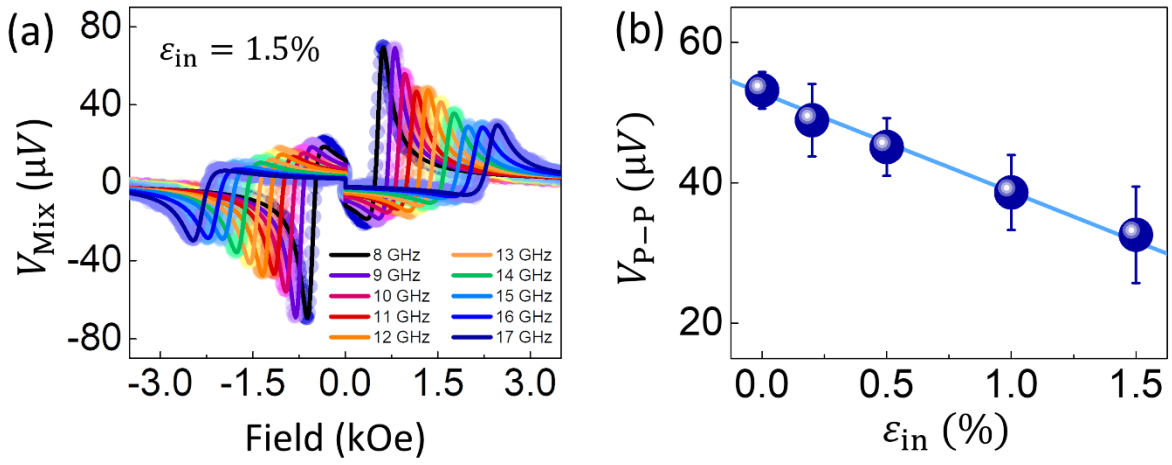

Figure 6-3 (a) Measured ST-FMR spectra of Pt/Co bilayer while applying $\varepsilon_{\text{in}} = 1.5\%$ for frequencies between 8 GHz and 17 GHz using microwave power of 12 dBm. (b) In-situ strain dependence of $V_{\text{P-P}}$ measured at 12 GHz.

Figure 6-3(a) shows the ST-FMR spectra for bilayer Pt/Co measured at a microwave power of 12 dBm with a frequency range of 8 to 17 GHz in steps of 1 GHz. The measured V_{mix} is fitted using Equation 3.8.4. The symmetric component is proportional to the damping-like torque and the anti-symmetric component is the result of the sum of the Oersted field and the field-like torque.[17,43] Here, the fitting equation 3.8.4 can be rewritten with a scaling factor V_0 which can be expressed as

$$V_{mix} = V_0\left[SF_S\left(H_{ext}\right) + AF_A\left(H_{ext}\right)\right], \tag{6.3.1}$$

where

$$V_0 = -\frac{1}{4}\frac{dR}{d\varphi}\frac{\gamma\mu_0 I_{RF}\cos\varphi}{2\pi\Delta H\left(df/dH_{ext}\right)\Big|_{H_{ext}=H_{res}}}, \tag{6.3.2}$$

and φ is the angle between the magnetization and the field and γ is the gyromagnetic ratio. The peak-to-peak voltage $V_{P\text{-}P}$ of the ST-FMR spectra decreases with increasing ε_{in} as shown in Figure 6-3(b). From Equation 6.3.2, V_0 is dependent on the ΔH, I_{RF} and $\left(df/dH_{ext}\right)\Big|_{H_{ext}=H_{res}}$. ΔH is related to the magnetic damping of the sample and previous work[41] had been shown ΔH to remain relatively constant with increasing strain, even with the decrease in effective damping of Pt/Co bilayer. Next, I_{RF} is the current density through the spin current generator, Pt. Since the resistivity of Pt changes with varying applied strain, the magnitude of the charge current

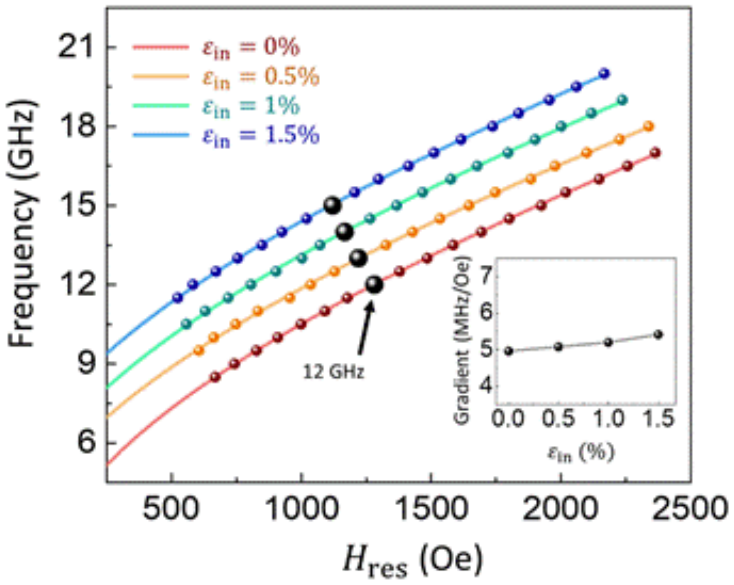

Figure 6-4 Kittel fitting of Pt/Co bilayer when exposed to varying ε_{in} with a y-axis offset. The bold black points are measured at 12 GHz. Inset: $\left(df/dH_{ext}\right)\Big|_{H_{ext}=H_{res}}$ dependence of strain at 12 GHz.

density changes as well resulting in a change in $V_{\text{P-P}}$. Lastly $\left(df/dH_{\text{ext}}\right)\big|_{H_{\text{ext}}=H_{\text{res}}}$, this term is the tangent value of the Kittel fitting at H_{res}. From Figure 6-4 inset, we observe that the change in $\left(df/dH_{\text{ext}}\right)\big|_{H_{\text{ext}}=H_{\text{res}}}$ at 12 GHz shows little change with a slight increase of less than 10% as compared to the change in $V_{\text{P-P}}$, suggesting that its contribution is minute. Therefore, after comparing the three potential contributing factors, the change in Pt resistivity is concluded to be the main contributing factor for the decrease in $V_{\text{P-P}}$. When the tensile strain is employed along the longitudinal direction of the microstrip, the strip elongates and narrows along the direction of strain resulting in an enhancement in resistivity.

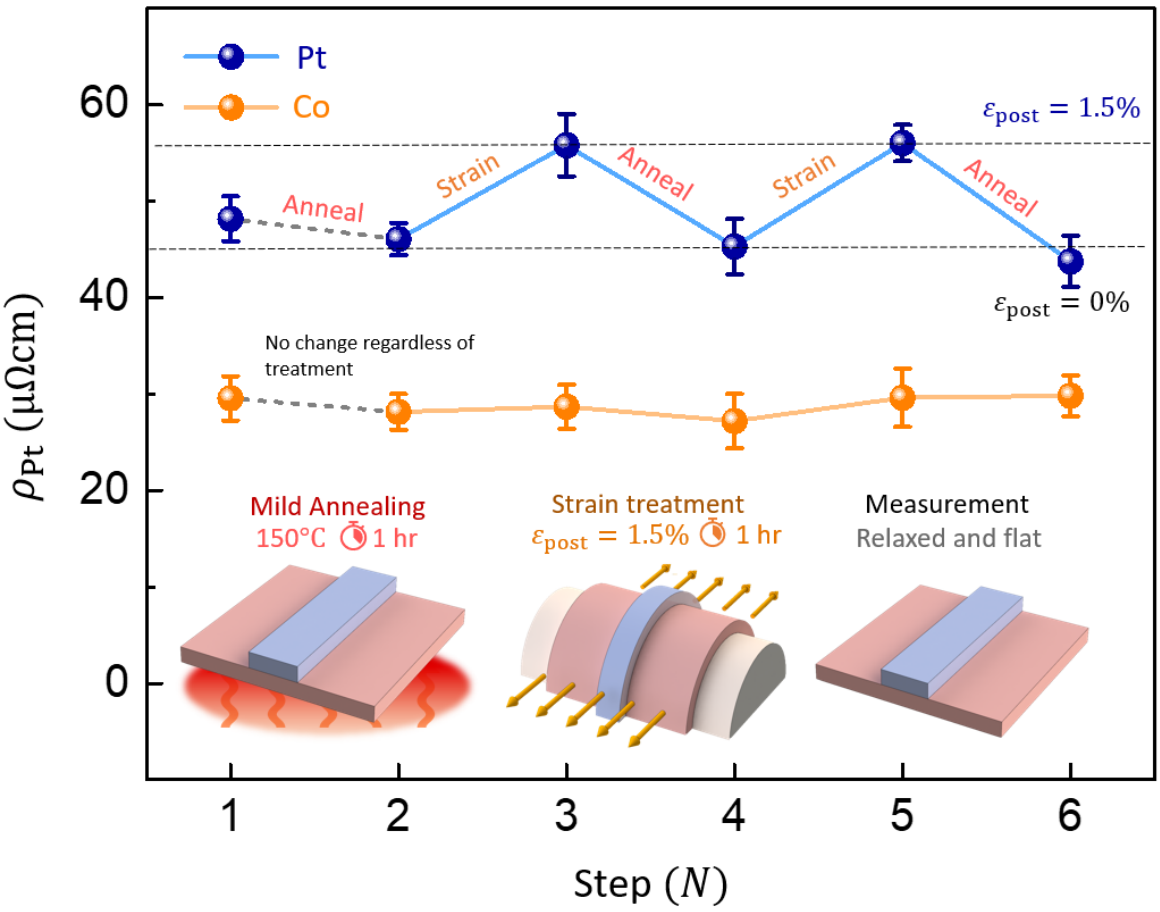

Figure 6-5 Resistivity of single layer Pt (5 nm) microstrip measured at different steps of N with inset illustrating the individual steps: step ① is the pristine film, step ② is the pristine film annealed at 150°C for 1 hr, step ③ is the annealed film treated with a tensile strain of $\varepsilon_{\text{post}}$ = 1.5% for 1 hr and step ④ is the strain-treated film annealed at 150°C for 1 hr, steps ⑤, and ⑥ are repeated treatment procedures that are the same as steps ③ and ④ respectively. The change in resistivity of Co is negligibly small as compared to Pt when strained and annealed.

6.4 Reversible SOT Manipulation

To determine the change in Pt resistivity, a separate set of single layer Pt(5 nm) microstrips were fabricated and characterized determined using a semiconductor analyzer at different steps as shown in Figure 6-5. At step ①, the film is in its pristine state after fabrication. To set the device, the sample is annealed at 150°C for 1 hr in step ②. The resistivity slightly decreased as a result of the improvement in film quality from the mild annealing. Thereafter in step ③, a tensile strain of $\varepsilon_{\text{post}} = 1.5\%$ was applied for 1 hr. During the strain treatment, the resistivity increases as the microstrips are stretched along the longitudinal direction resulting in a narrower cross-sectional area. Relaxing the film after the treatment for measurement, the residual strain within the Pt retains the enhanced resistivity as shown in the plot. For step ④, the sample was annealed at 150°C for 1 hr before characterization and upon mild annealing, the resistivity of Pt decreases as the internal strain caused by the strain treatment is relieved. Finally, step ⑤ and ⑥ are repeated steps that are the same as step ③ and ④ respectively that shows the repeatability of the process.

The coefficient of strain sensitivity of resistance, or gauge factor describes the change in resistance of a material when exposed to strain. *G.C. Kuczynski*[44] studied the effects of strain on the electrical resistance of metals and showed that the coefficient can be rearranged and expressed the strain coefficient of resistivity, which is given by

$$\frac{d\rho}{\rho d\varepsilon} = 1+2\gamma(1-2\mu) \tag{6.4.3}$$

where γ is the and Grüneisen's constant and μ is the Poisson's ratio. From this expression, Co is expected to have a much smaller resistivity change when exposed to strain as compared to Pt due to smaller γ and μ values. To support this, we measured the resistivity of the Co layer as shown in Figure 6-5 and found that the Co resistivity change is negligibly small in contrast to Pt. This finding is coherent with the XRD result as the Co (002) peak remains unchanged and further justifies that the Pt resistivity change is responsible for the reversible SOT manipulation.

Since the Pt layer thickness is much larger than its spin diffusion length, the field-like torque in bilayer Pt/Co can be assumed to be negligibly small as shown in previous work.[17,38,45] Using this approximation, the spin Hall efficiency for Pt/Co bilayer is calculated by using Equation 3.8.8. The M_S of bilayer Pt/Co measured at $\varepsilon_{\text{post}}$ =0% and 1.5% was obtained to be 1220 ± 30 and 1130 ± 40 emu/cc^3, which is within a range consistent with other work and therefore, magnetic proximity effect is assumed to be negligible in this study.[46-49] To obtain the required M_{eff}, the in-plane magnetization Kittel equation as shown in Equation 3.8.6 was used, where γ is the gyromagnetic ratio and H_K is the total magnetic anisotropy field. Having similar behavior as the ρ_{Pt}, the θ_{eff} at various measurement steps is as summarized in Figure 6-7(a). From the proportionality between both the ρ_{Pt} and θ_{eff}, the strain mediated SOT enhancement is a result of the extrinsic SHE in the Pt layer.

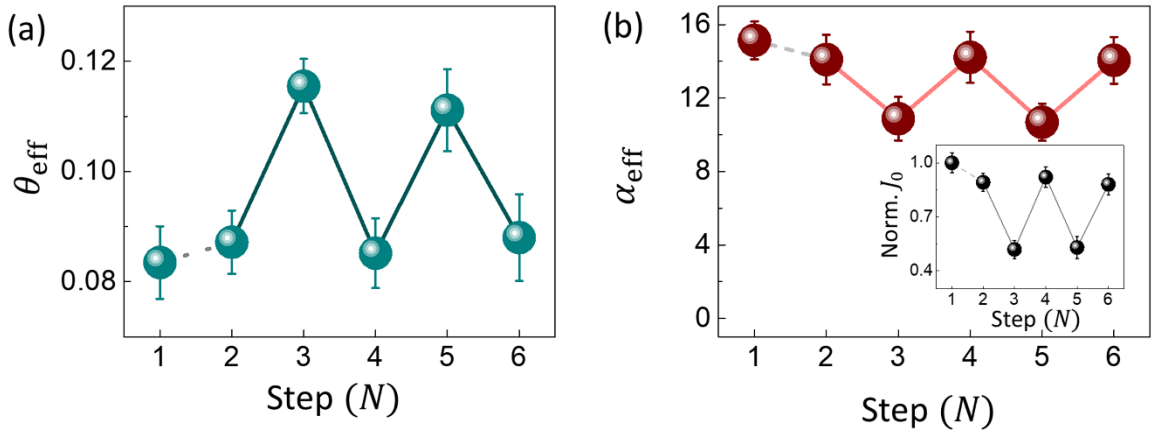

Figure 6-6 (a) Spin Hall efficiency and (b) Gilbert damping parameter with inset showing the normalized switching current density of bilayer Pt/Co measured at different steps of N: step ① is the pristine film, step ② is the pristine film annealed at 150°C for 1 hr, step ③ is the annealed film treated with tensile strain of $\varepsilon_{\text{post}} = 1.5\%$ for 1 hr and step ④ is the strain treated film annealed at 150°C for 1 hr, step ⑤ and ⑥ are repeated steps similar to step ③ and ④.

Predominantly, the ΔH of the ST-FMR spectra is broadened by extrinsic contribution such as the film inhomogeneous broadening term (ΔH) and two magnon scattering. Two magnon scattering results in a nonlinear frequency dependence of the ΔH, which is not observed in the measured samples.[50] The effective Gilbert damping parameter (α_{eff}) was calculated from the ΔH dependences of the frequency expressed as in Equation 3.8.7 and the data is as shown in Figure 6-7(b). The two main α_{eff} contributor of bilayer Pt/Co is the intrinsic Gilbert damping (α_{int}) from Co and the damping introduced by spin pumping effect (α_{SP}) due to the adjacent Pt.[51,52] α_{int} remains unchanged as it is independent of the strain-induced

magnetic anisotropy.[53-55] The α_{SP}, however, is highly dependent on the spin pumping effect at the interface between the Pt and Co layer. An enhancement in the extrinsic SHE will result in a greater spin pumping effect and hence larger α_{SP} contribution. Therefore, α_{eff} has an inverse trend as compared to the ρ_{Pt} and θ_{eff}.

The effects of strain and mild annealing on the critical switching current density J_{C0} of an in-plane magnetization SOT device can be evaluated using Equation 4.6.1. From this equation, J_{C0} is proportional to the ratio $\alpha_{eff}/\theta_{eff}$ and a decrease in this ratio will denote a lower J_{C0}.[46,56] The inset in Figure 6-7(b) shows how the J_{C0} can be controlled using a combination of mechanical strain and mild annealing. This method allows the J_{C0} to alternate between ~90% and ~50% of the pristine J_{C0}, allowing for an additional degree of freedom in inducing magnetization reversal of the SOT device.

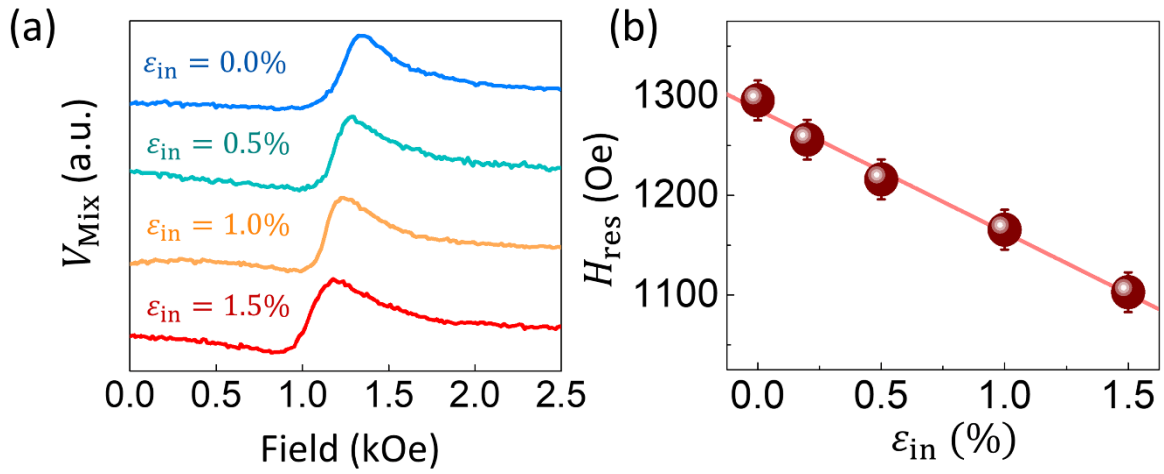

Figure 6-7 (a) Leftward shift of ST-FMR spectra due to tensile strain at varying ε_{in}. The spectra are stacked with vertical offset for ease of comparison. (b) *In-situ* strain dependence of H_{Res}.

6.5 Tunable Microwave Detector

Besides SOT manipulation, mechanical strain can also be used to tune the resonance frequency by shifting the FMR spectrum and from Figure 6-7(a), a left shift motion of the ST-FMR spectra is observed as the *in-situ* tensile strain applied increases.[57] The shift in H_{Res} is attributed by the magnetoelastic anisotropy induced by the mechanical tensile strain. This additional anisotropy has an easy axis perpendicular to the uniaxial anisotropy generated by the external magnetic field which will result in a shift in the magnetic easy axis of Pt/Co bilayer.[39] Figure 6-7(b) shows the H_{Res} dependence of $\varepsilon_{\mathrm{in}}$. The Pt/Co device has a tunable H_{Res} with a magnitude of -123 ± 6 Oe per unit $\varepsilon_{\mathrm{in}}$. Using this tuning capability, the detectable H_{Res} can be adjusted based on the applied strain and then reversed by relaxing the device.

Figure 6-8(a) demonstrates how the Pt/Co device can switch between two states of H_{Res} by applying strain and relaxing it. The first cycle begins with the device in the pristine state measured at the relaxed position. Subsequently, the even cycles refer to the in-situ strain device while the odd cycles are measured when the device is relaxed. With every cycle, a distinct shift in H_{Res} is observed. This cycle of straining and relaxing is performed continuously for a repeatability test as shown in Figure 6-8(b). For consistency of the cycles, the straining and relaxing are performed using a linear actuator attached with a stepper motor. The H_{Res} at both 0% and 1% strain are highly stable for 10^4 cycles demonstrating the device robustness against mechanical strain.

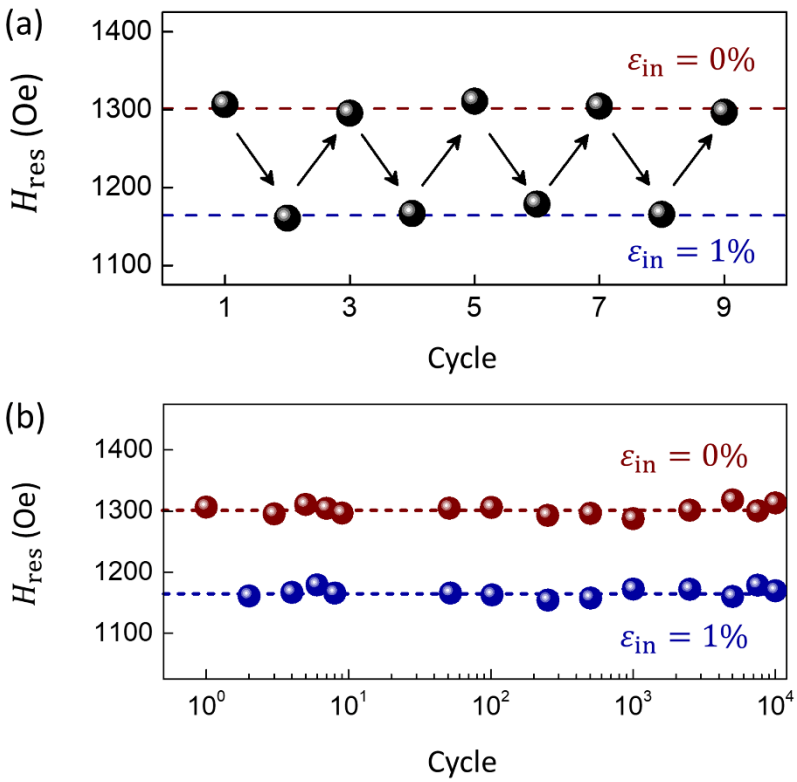

Figure 6-8 (a) H_{Res} of Pt/Co bilayer as a function of the reversible tensile strain $\varepsilon_{in} = 0\%$ and $\varepsilon_{in} = 1\%$ performed using microwave frequency of 12 GHz. (b) H_{Res} over 10,000 cycles of bending and relaxing to demonstrate the robustness of the device. For consistency, an automated linear actuator was employed to exert the required strain onto the device.

In summary, we investigated the use of mild annealing and mechanical strain for reversible manipulation of the SOT. In Pt/Co bilayer, XRD spectra show that the tensile strain induces a residual strain within the Pt layer that can be alleviated by treating the film with mild annealing. Using a combination of these two treatment methods, the spin Hall efficiency and Gilbert damping parameter become versatile and can be tuned with ease even after fabrication. Apart from SOT manipulation, strain can be used to tune the resonance field of Pt/Co bilayer and in the endurance test performed, the tunablility of the device remains highly stable even after 10^4 cycles. These results pave an alternative avenue for manipulating the SOT reversibly that can also be used as a tunable microwave detector.

Reference

1 G.D.H. Wong, C.C.I. Ang, W.L. Gan, W.C. Law, Z. Xu, F. Xu, C.S. Seet & W.S. Lew. Reversible strain-induced spin–orbit torque on flexible substrate. *Applied Physics Letters* **119**, 042402, doi:10.1063/5.0056995 (2021).

2 Y.K. Kato, R.C. Myers, A.C. Gossard & D.D. Awschalom. Observation of the spin Hall effect in semiconductors. *Science* **306**, 1910-1913 (2004).

3 J. Wunderlich, B. Kaestner, J. Sinova & T. Jungwirth. Experimental observation of the spin-Hall effect in a two-dimensional spin-orbit coupled semiconductor system. *Physical Review Letters* **94**, 047204 (2005).

4 G.-Y. Guo, S. Murakami, T.-W. Chen & N. Nagaosa. Intrinsic spin Hall effect in platinum: First-principles calculations. *Physical Review Letters* **100**, 096401 (2008).

5 E. Saitoh, M. Ueda, H. Miyajima & G. Tatara. Conversion of spin current into charge current at room temperature: Inverse spin-Hall effect. *Applied Physics Letters* **88**, 182509 (2006).

6 T. Kimura, Y. Otani, T. Sato, S. Takahashi & S. Maekawa. Room-temperature reversible spin Hall effect. *Physical Review Letters* **98**, 156601 (2007).

7 T. Tanaka, H. Kontani, M. Naito, T. Naito, D.S. Hirashima, K. Yamada & J. Inoue. Intrinsic spin hall effect and orbital Hall effect in 4 d and 5 d transition metals. *Physical Review B* **77**, 165117 (2008).

8 M. Morota, Y. Niimi, K. Ohnishi, D. Wei, T. Tanaka, H. Kontani, T. Kimura & Y. Otani. Indication of intrinsic spin Hall effect in 4 d and 5 d transition metals. *Physical Review B* **83**, 174405 (2011).

9 S. Emori, U. Bauer, S.-M. Ahn, E. Martinez & G.S. Beach. Current-driven dynamics of chiral ferromagnetic domain walls. *Nature Materials* **12**, 611-616 (2013).

10 S. Valenzuela & M. Tinkham. Electrical detection of spin currents: The spin-current induced Hall effect. *Journal of Applied Physics* **101**, 09B103 (2007).

11 J. Hirsch. Spin hall effect. *Physical Review Letters* **83**, 1834 (1999).

12 S. Zhang. Spin Hall effect in the presence of spin diffusion. *Physical Review Letters* **85**, 393 (2000).

13 A. Mellnik, J. Lee, A. Richardella, J. Grab, P. Mintun, M.H. Fischer, A. Vaezi, A. Manchon, E.-A. Kim & N. Samarth. Spin-transfer torque generated by a topological insulator. *Nature* **511**, 449-451 (2014).

14 J. Zhou, X. Wang, Y. Liu, J. Yu, H. Fu, L. Liu, S. Chen, J. Deng, W. Lin & X. Shu. Large spin-orbit torque efficiency enhanced by magnetic structure of collinear antiferromagnet IrMn. *Science Advances* **5**, eaau6696 (2019).

15 W. Zhang, W. Han, S.-H. Yang, Y. Sun, Y. Zhang, B. Yan & S.S. Parkin. Giant facet-dependent spin-orbit torque and spin Hall conductivity in the triangular antiferromagnet IrMn3. *Science Advances* **2**, e1600759 (2016).

16 X. Tao, Q. Liu, B. Miao, R. Yu, Z. Feng, L. Sun, B. You, J. Du, K. Chen & S. Zhang. Self-consistent determination of spin Hall angle and spin diffusion length in Pt and Pd: The role of the interface spin loss. *Science Advances* **4**, eaat1670 (2018).

17 L. Liu, T. Moriyama, D. Ralph & R. Buhrman. Spin-torque ferromagnetic resonance induced by the spin Hall effect. *Physical Review Letters* **106**, 036601 (2011).

18 L. Liu, C.-F. Pai, Y. Li, H. Tseng, D. Ralph & R. Buhrman. Spin-torque switching with the giant spin Hall effect of tantalum. *Science* **336**, 555-558 (2012).

19 C.-F. Pai, L. Liu, Y. Li, H. Tseng, D. Ralph & R. Buhrman. Spin transfer torque devices utilizing the giant spin Hall effect of tungsten. *Applied Physics Letters* **101**, 122404 (2012).

20 Q. Hao, W. Chen & G. Xiao. Beta (β) tungsten thin films: Structure, electron transport, and giant spin Hall effect. *Applied Physics Letters* **106**, 182403 (2015).

21 Y. Wang, P. Deorani, X. Qiu, J.H. Kwon & H. Yang. Determination of intrinsic spin Hall angle in Pt. *Applied Physics Letters* **105**, 152412 (2014).

22 C. Hahn, G. De Loubens, O. Klein, M. Viret, V.V. Naletov & J.B. Youssef. Comparative measurements of inverse spin Hall effects and magnetoresistance in YIG/Pt and YIG/Ta. *Physical Review B* **87**, 174417 (2013).

23 Z. Xu, G.D.H. Wong, J. Tang, E. Liu, W.L. Gan, F. Xu & W.S. Lew. Giant Spin Hall Effect in Cu-Tb Alloy Thin Films. *ACS Applied Materials & Interfaces* (2020).

24 L. Zhu & R. Buhrman. Maximizing Spin-Orbit-Torque Efficiency of Pt/Ti Multilayers: Trade-Off Between Intrinsic Spin Hall Conductivity and Carrier Lifetime. *Physical Review Applied* **12**, 051002 (2019).

25 A. Fert & P.M. Levy. Spin Hall effect induced by resonant scattering on impurities in metals. *Physical Review Letters* **106**, 157208 (2011).

26 R. Ramaswamy, Y. Wang, M. Elyasi, M. Motapothula, T. Venkatesan, X. Qiu & H. Yang. Extrinsic spin Hall effect in $Cu_{1-x}Pt_x$. *Physical Review Applied* **8**, 024034 (2017).

27 G.D.H. Wong, W.L. Law, F.N. Tan, W.L. Gan, C.C.I. Ang, Z. Xu, C.S. Seet & W.S. Lew. Thermal behavior of spin-current generation in Pt_xCu_{1-x} devices characterized through spin-torque ferromagnetic resonance. *Scientific Reports* **10**, 1-8 (2020).

28 J.W. Lee, Y.-W. Oh, S.-Y. Park, A.I. Figueroa, G. Van Der Laan, G. Go, K.-J. Lee & B.-G. Park. Enhanced spin-orbit torque by engineering Pt resistivity in Pt/Co/Al O x structures. *Physical Review B* **96**, 064405 (2017).

29 M.-H. Nguyen, M. Zhao, D. Ralph & R. Buhrman. Enhanced spin Hall torque efficiency in $Pt_{100-x}Al_x$ and $Pt_{100-x}Hf_x$ alloys arising from the intrinsic spin Hall effect. *Applied Physics Letters* **108**, 242407 (2016).

30 P. Laczkowski, H. Jaffrès, W. Savero-Torres, J.-C. Rojas-Sánchez, Y. Fu, N. Reyren, C. Deranlot, L. Notin, C. Beigné & J.-P. Attané. Evaluation of spin diffusion length of AuW alloys using spin absorption experiments in the limit of large spin-orbit interactions. *Physical Review B* **92**, 214405 (2015).

31 T.-Y. Chen, C.-T. Wu, H.-W. Yen & C.-F. Pai. Tunable spin-orbit torque in Cu-Ta binary alloy heterostructures. *Physical Review B* **96**, 104434 (2017).

32 Y. Niimi, Y. Kawanishi, D. Wei, C. Deranlot, H. Yang, M. Chshiev, T. Valet, A. Fert & Y. Otani. Giant spin Hall effect induced by skew scattering from bismuth impurities inside thin film CuBi alloys. *Physical Review Letters* **109**, 156602 (2012).

33 D. Qu, S. Huang, G. Guo & C. Chien. Inverse spin Hall effect in A u x T a 1− x alloy films. *Physical Review B* **97**, 024402 (2018).

34 J. Smit. The spontaneous Hall effect in ferromagnetics II. *Physica* **24**, 39-51 (1958).

35 L. Berger. Side-jump mechanism for the Hall effect of ferromagnets. *Physical Review B* **2**, 4559 (1970).

36 M. Filianina, J.-P. Hanke, K. Lee, D.-S. Han, S. Jaiswal, A. Rajan, G. Jakob, Y. Mokrousov & M. Kläui. Electric-field control of spin-orbit torques in perpendicularly magnetized W/CoFeB/MgO films. *Physical Review Letters* **124**, 217701 (2020).

37 E. Liu, T. Fache, D. Cespedes-Berrocal, Z. Zhang, S. Petit-Watelot, S. Mangin, F. Xu & J.-C. Rojas-Sánchez. Strain-Enhanced Charge-to-Spin Conversion in Ta/Fe/Pt Multilayers Grown on Flexible Mica Substrate. *Physical Review Applied* **12**, 044074 (2019).

38 T. Nan, J.M. Hu, M. Dai, S. Emori, X. Wang, Z. Hu, A. Matyushov, L.Q. Chen & N. Sun. A Strain-Mediated Magnetoelectric-Spin-Torque Hybrid Structure. *Advanced Functional Materials* **29**, 1806371 (2019).

39 Z. Zhang, E. Liu, W. Zhang, P.K.J. Wong, Z. Xu, F. Hu, X. Li, J. Tang, A.T.S. Wee & F. Xu. Mechanical Strain Manipulation of Exchange Bias Field and Spin Dynamics in FeCo/IrMn Multilayers Grown on Flexible Substrates. *ACS applied materials & interfaces* **11**, 8258-8265 (2019).

40 H. An, S. Haku, Y. Kanno, H. Nakayama, H. Maki, J. Shi & K. Ando. Manipulation of Spin-Torque Generation Using Ultrathin Au. *Physical Review Applied* **9**, 064016 (2018).

41 G.D.H. Wong, Z. Xu, W.L. Gan, C.C.I. Ang, W.C. Law, J. Tang, W. Zhang, P.K.J. Wong, X. Yu, F. Xu, A.T.S. Wee, C.S. Seet & W.S. Lew. Strain-Mediated Spin–Orbit Torque Enhancement in Pt/Co on Flexible Substrate. *ACS Nano* **15**, 8319-8327, doi:10.1021/acsnano.0c09404 (2021).

42 M. De Jong, W. Chen, T. Angsten, A. Jain, R. Notestine, A. Gamst, M. Sluiter, C.K. Ande, S. Van Der Zwaag & J.J. Plata. Charting the complete elastic properties of inorganic crystalline compounds. *Scientific data* **2**, 1-13 (2015).

43 C.-F. Pai, Y. Ou, L.H. Vilela-Leão, D. Ralph & R. Buhrman. Dependence of the efficiency of spin Hall torque on the transparency of Pt/ferromagnetic layer interfaces. *Physical Review B* **92**, 064426 (2015).

44 G. Kuczynski. Effect of elastic strain on the electrical resistance of metals. *Physical Review* **94**, 61 (1954).

45 W. Skowroński, Ł. Karwacki, S. Ziętek, J. Kanak, S. Łazarski, K. Grochot, T. Stobiecki, P. Kuświk, F. Stobiecki & J. Barnaś. Determination of Spin Hall Angle in Heavy-Metal/Co− Fe− B-Based Heterostructures with Interfacial Spin-Orbit Fields. *Physical Review Applied* **11**, 024039 (2019).

46 L. Huang, S. He, Q.J. Yap & S.T. Lim. Engineering magnetic heterostructures to obtain large spin Hall efficiency for spin-orbit torque devices. *Applied Physics Letters* **113**, 022402 (2018).

47 H. Bouloussa, R. Ramaswamy, Y. Roussigné, A. Stashkevich, H. Yang, M. Belmeguenai & S. Chérif. Pt concentration dependence of the interfacial Dzyaloshinskii–Moriya interaction, the Gilbert damping parameter and the magnetic anisotropy in Py/Cu1− xPtx systems. *Journal of Physics D: Applied Physics* **52**, 055001 (2018).

48 L. Zhu, D. Ralph & R. Buhrman. Irrelevance of magnetic proximity effect to spin-orbit torques in heavy-metal/ferromagnet bilayers. *Physical Review B* **98**, 134406 (2018).

49 J. Geissler, E. Goering, M. Justen, F. Weigand, G. Schütz, J. Langer, D. Schmitz, H. Maletta & R. Mattheis. Pt magnetization profile in a Pt/Co bilayer studied by resonant magnetic x-ray reflectometry. *Physical Review B* **65**, 020405 (2001).

50 R. Arias & D. Mills. Extrinsic contributions to the ferromagnetic resonance response of ultrathin films. *Physical Review B* **60**, 7395 (1999).

51 O. Mosendz, V. Vlaminck, J. Pearson, F. Fradin, G. Bauer, S. Bader & A. Hoffmann. Detection and quantification of inverse spin Hall effect from spin pumping in permalloy/normal metal bilayers. *Physical Review B* **82**, 214403 (2010).

52 J.M. Shaw, H.T. Nembach & T.J. Silva. Determination of spin pumping as a source of linewidth in sputtered $Co_{90}Fe_{10}$/Pd multilayers by use of broadband ferromagnetic resonance spectroscopy. *Physical Review B* **85**, 054412 (2012).

53 M. Tang, W. Li, Y. Ren, Z. Zhang & Q. Jin. Lack of dependence between intrinsic magnetic damping and perpendicular magnetic anisotropy in $Cu(t_{Cu})/[Ni/Co]_N$ multilayers. *Journal of Magnetism and Magnetic Materials* **428**, 269-273 (2017).

54 M. Tang, W. Li, Y. Ren, Z. Zhang, S. Lou & Q. Jin. Magnetic damping and perpendicular magnetic anisotropy in Pd-buffered $[Co/Ni]_5$ and $[Ni/Co]_5$ multilayers. *RSC Advances* **7**, 5315-5321 (2017).

55 A. Barman, S. Wang, O. Hellwig, A. Berger, E.E. Fullerton & H. Schmidt. Ultrafast magnetization dynamics in high perpendicular anisotropy $[Co/Pt]_n$ multilayers. *Journal of Applied Physics* **101**, 09D102 (2007).

56 K.-S. Lee, S.-W. Lee, B.-C. Min & K.-J. Lee. Threshold current for switching of a perpendicular magnetic layer induced by spin Hall effect. *Applied Physics Letters* **102**, 112410 (2013).

57 W. Liu, M. Liu, R. Ma, R. Zhang, W. Zhang, D. Yu, Q. Wang, J. Wang & H. Wang. Mechanical Strain-Tunable Microwave Magnetism in Flexible CuFe2O4 Epitaxial Thin Film for Wearable Sensors. *Advanced Functional Materials* **28**, 1705928 (2018).

Chapter 7 Conclusion and Future Works

7.1 Summary of the Thesis

Current-induced magnetization switching through SOT is one of the key constituents for SOT applications. These devices entice us with their promising high performance yet low power consumption attributes making them an ideal alternative to the next generation of memory and logic devices. However, in order to for this to be possible, the θ_{eff} of the spin Hall generator has to be well studied and maximized. To date, there have been many techniques used to achieve high θ_{eff} such as using multilayered spin Hall generator, metal oxides and varying deposition conditions of HM. Among the different methods used, a promising and widely adopted technique is by alloying a HM with a lighter and more conductive metal. In Chapter 4, the damping constant and spin Hall efficiency of Pt_xCu_{1-x} alloys are investigated at elevated temperatures and the results demonstrated that these parameters can be modulated by tuning the alloy composition. Another finding is that Pt_xCu_{1-x} alloys with greater Pt content tend to be less temperature sensitive and exhibit larger damping. The minimum $\alpha_{\text{eff}} / \theta_{\text{eff}}$ ratio was fulfilled at $Pt_{47}Cu_{53}$ and since this ratio is directly proportional to the switching current density required, this would translate to this alloy composition having the optimal switching current density. At this composition, the temperature dependence of effective damping is also negligible due to the counteracting relationship between α_{int} and α_{SP}. The spin transparency was also explored revealing that at this composition the spin transparency is at its highest at 0.85 ± 0.09. Therefore, this demonstrates a technique to modulate the θ_{eff} and enhance the thermal robustness for device operations at elevated temperatures.

Next, in Chapter 5, the strain-mediated SOT enhancement is explored in Pt/Co bilayer, and the findings demonstrate that tensile strain can enhance θ_{eff}. Of which, 78% of the enhancement is retained even after the strain is removed. Spin transparency and XMCD measurements rule out the possibility of an improvement in the Pt/Co bilayer interface quality or interfacial spin-orbit interaction, thus leading us to hypothesize that the enhancement is a bulk effect in Pt. With the aid of strain treatment, the spin Hall angle, $\theta_{\text{SH}} = \theta_{\text{eff}} / T_{\text{int}}$, of Pt could potentially be much greater than the previously reported value of ~0.30 after accounting for the spin transparency at $\varepsilon_{\text{post}} = 1.5\%$.[1] Furthermore, the ability to drastically reduce the switching

current density due to the decrease in the $\alpha_{\text{eff}}/\theta_{\text{eff}}$ ratio is especially appealing for the development of power-efficient and flexible spintronics devices.

Building onto the idea of capitalizing the residual strain-mediated SOT enhancement, Chapter 6 investigates how this enhancement could be manipulated. From the findings, it has been demonstrated that by using a combination of mechanical strain and mild annealing, the strain-induced SOT can be controlled reversibly. During the manipulation, besides the spin Hall efficiency, the Gilbert damping and switching current density were also all altered accordingly. Apart from the SOT manipulation, the strain also induces a magnetoelectric anisotropy that shifts the magnetic easy axis of the FM, which allows the resonance field of Pt/Co bilayer to be tuned. In the endurance test performed, the tunability of the device remains highly stable even after 10^4 cycles. These results make strain an attractive candidate for not only SOT enhancement but also as a tunable microwave detector.

7.2 Future Works

The potential of the SOT device as an emerging non-volatile, power-efficient, high-speed, and high endurance memory device relies heavily on the θ_{eff} of the spin current generator. Although there have been many ongoing research revolving about understanding and improving the performance of the spin current generator, there are still many unexplored techniques and materials that could potentially yield high θ_{eff}. In this section, we will be discussing various ideas that build upon the fundamentals of our existing work to push the boundaries of the SOT device capabilities.

7.2.1 Alloying Rare-Earth Metals

Alloying is an attractive technique often used to elevate the θ_{eff} of the HM and modulate it to the specific SOT application needs. Typically alloying is performed between an HM with an already high θ_{eff} and a conductive light metal to enhance the spin Hall conductivity of the material and such examples include Pt_xCu_{1-x},[2-6] $Au_{1-x}Pt_x$,[7] $Cu_{1-x}W_x$,[8] AuW,[9] and Au_xTa_{1-x}[10]. Though this technique has shown remarkable results for HM metals, its application on rare-

earth metals remains unexplored. RE metals have often been often looked upon when searching for potential HM with large θ_{eff} due to their large SOC. Both theoretical and experimental works have been conducted to investigate and demonstrate their promising abilities however, most investigate are limited to its intrinsic spin Hall effect and not its extrinsic.[11-15] In Chapter 4, we explored the θ_{eff} enhancement and the thermal robustness benefits of alloying. This work can be extended further for application on the RE elements to determine their optimal composition.

Apart from alloying, a gradient transition from the FM to the HM can also be considered for improved spin transparency through interfacial alloying. There have been works demonstrating the enhancement and in Chapter 4, the spike in spin transparency at specific alloy composition is a result of this improvement.[16]

7.2.2 Further Investigation of Spin-Orbit Torque Using Flexible Substrate

Strain-mediated SOT enhancement is a relatively new technique of controlling the spin current generation. To date, the materials and the device structure studied on flexible substrates are convention materials that work well using the standard Si substrates.[17-19] Chapter 5 and 6 only scratched the surface of this new realm of study as only Pt/Co bilayer is studied. Other materials with high Poisson ratio such as Au and Pd are potential candidate to induce strain-mediated SOT enhancement. Besides pure HM, alloyed materials are also of interest as mechanical strain may induce additional disordered-ness within material and thus enhancing the extrinsic spin Hall effect. In Chapter 5 and 6, Pt/Co bilayer experiences residual strain resulting in the SOT-enhancement to remain. Investigation on how Poisson ratio with the magnitude of residual strain can help develop a reversible strain-induced SOT device without having the need of mild annealing.

Although there have been several works demonstrating the MTJ switching using STT, experimental SOT-driven magnetization switching on flexible substrate remains elusive and unexplored. With only a handful of experimental demonstration, this leaves plenty of room for SOT investigation on flexible substrate.

7.2.3 Ionic Liquid Gating on Multi-Insertion Layer Structure

In Chapter 6, a combination of mechanical strain and mild annealing was used to reversibly manipulate the θ_{eff} of the HM. Another alterative technique that surfaced recently was the use of ionic liquid gating voltage to control the θ_{eff}. Here, the ionic liquid acts as a gate that switches on and off with the application of a voltage bias and by doing so, the interfacial roughness between the HM and FM can be modified allowing for more significant spin current generation.[20] However, in works by *H. An et al.*, they only attempted to alter an ultrathin single Au layer.[20] His work can be extrapolated onto spin Hall generators structures with multiple insertion layers. As demonstrated by *L. Zhu et al.*, having multiple insertion layers in a HM can help induce considerable amount of interfacial scattering enhancing the extrinsic spin Hall effect.[21,22] By applying an ionic liquid gate voltage to multiple insertion layers, the interfacial scattering can be drastically enhanced.

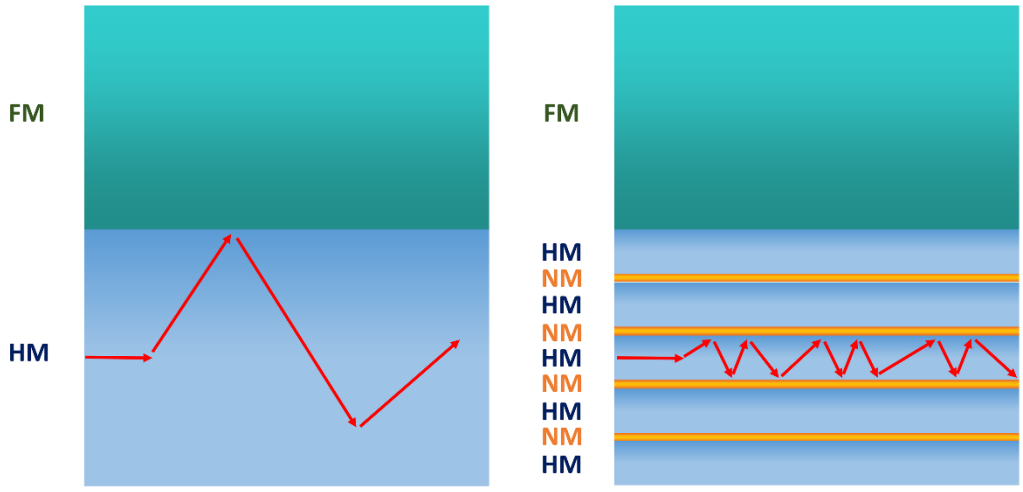

Figure 8-1 Schematic of illustrating the interfacial scattering resulting in the enhancement of resistivity.

Another characteristic of ionic liquid often overlooked is the ability to chemically etch metals even after device fabrication and during measurement. By controlling the intensity of the biased voltage and the duration of bias, thickness dependent measurement of HM or FM is made possible with only a single sample. This allows for more consistent measurement as the measured device is the same and improve the work efficiency by reducing time spent on fabricating multiple samples.

7.2.4 Spin Diode for Microwave Detection & Energy Harvesting

In addition to its memory storage application, the MTJ can be used as spin diodes[23-30] and spin Hall nano-oscillators (SHNOs)[31-35]. Both devices are opposite counterparts of one another. The spin diode takes in high frequency alternating current (AC) and rectifies it to produce a DC current while the SHNO requires a DC current to emit a microwave frequency AC. The operating principles behind then spin diode relies on the coupling between the injected alternating microwave current and the alternating resistance due to the magnetization precession as explained in Chapter 3.8. As such, this makes the ST-FMR technique the perfect measurement tool to characterize the spin diode as it injects AC to detect for rectified DC all while the sample is at its ferromagnetic resonance state.

The current research progression for spin diode remains relatively new and unexplored. Most works require some form of additional energy such as external magnetic field or DC bias on top of the AC microwave current in order to rectify voltage.[23-27] This cripples the spin diode functionality as an energy harvesting device as it is no longer self-sustained. One way to work around this would be the use of MTJ with perpendicular magnetic anisotropy (PMA) as they are able to rectify microwaves even in the absence of external field. Furthermore, such MTJ can potentially harvest energy from more than one band. By tuning the magnetic properties of the free and reference layer, dual band microwave energy harvesting is made possible. One ideal application of this dual band microwave energy harvester can be used to harness the wasted and unused ambient microwave such as 2.4 GHz and 5.8 GHz WiFi signals.

Reference

1 C.-F. Pai, Y. Ou, L.H. Vilela-Leão, D. Ralph & R. Buhrman. Dependence of the efficiency of spin Hall torque on the transparency of Pt/ferromagnetic layer interfaces. *Physical Review B* **92**, 064426 (2015).

2 G.D.H. Wong, W.L. Law, F.N. Tan, W.L. Gan, C.C.I. Ang, Z. Xu, C. Seet & W.S. Lew. Thermal behavior of spin-current generation in Pt_xCu_{1-x} devices characterized through spin-torque ferromagnetic resonance. *Scientific Reports* **10**, 1-8 (2020).

3 R. Ramaswamy, Y. Wang, M. Elyasi, M. Motapothula, T. Venkatesan, X. Qiu & H. Yang. Extrinsic spin Hall effect in $Cu_{1-x}Pt_x$. *Physical Review Applied* **8**, 024034 (2017).

4 H. Bouloussa, R. Ramaswamy, Y. Roussigné, A. Stashkevich, H. Yang, M. Belmeguenai & S. Chérif. Pt concentration dependence of the interfacial Dzyaloshinskii–Moriya interaction, the Gilbert damping parameter and the magnetic anisotropy in $Py/Cu_{1-x}Pt_x$ systems. *Journal of Physics D: Applied Physics* **52**, 055001 (2018).

5 L. Zhu, D.C. Ralph & R.A. Buhrman. Maximizing Spin-Orbit Torque Generated by the Spin Hall Effect of Pt. *arXiv Preprint arXiv:2106.04992* (2021).

6 C.Y. Hu & C.F. Pai. Benchmarking of Spin–Orbit Torque Switching Efficiency in Pt Alloys. *Advanced Quantum Technologies* **3**, 2000024 (2020).

7 L. Zhu, D.C. Ralph & R.A. Buhrman. Highly efficient spin-current generation by the spin Hall effect in $Au_{1-x}Pt_x$. *Physical Review Applied* **10**, 031001 (2018).

8 B. Coester, G.D.H. Wong, Z. Xu, J. Tang, W.L. Gan & W.S. Lew. Enhanced spin Hall conductivity in tungsten-copper alloys. *Journal of Magnetism and Magnetic Materials* **523**, 167545 (2021).

9 P. Laczkowski, J.-C. Rojas-Sánchez, W. Savero-Torres, H. Jaffrès, N. Reyren, C. Deranlot, L. Notin, C. Beigné, A. Marty & J.-P. Attané. Experimental evidences of a large extrinsic spin Hall effect in AuW alloy. *Applied Physics Letters* **104**, 142403 (2014).

10 D. Qu, S. Huang, G. Guo & C. Chien. Inverse spin Hall effect in Au_xTa_{1-x} alloy films. *Physical Review B* **97**, 024402 (2018).

11 T. Tanaka, H. Kontani, M. Naito, T. Naito, D.S. Hirashima, K. Yamada & J. Inoue. Intrinsic spin hall effect and orbital Hall effect in 4d and 5d transition metals. *Physical Review B* **77**, 165117 (2008).

12 T. Tanaka & H. Kontani. Intrinsic spin and orbital Hall effects in heavy-fermion systems. *Physical Review B* **81**, 224401 (2010).

13 C. Du, H. Wang, F. Yang & P.C. Hammel. Systematic variation of spin-orbit coupling with d-orbital filling: Large inverse spin Hall effect in 3d transition metals. *Physical Review B* **90**, 140407 (2014).

14 H. Kontani, T. Tanaka, D. Hirashima, K. Yamada & J. Inoue. Giant orbital Hall effect in transition metals: Origin of large spin and anomalous Hall effects. *Physical Review Letters* **102**, 016601 (2009).

15 C. Du, H. Wang, P.C. Hammel & F. Yang. Y3Fe5O12 spin pumping for quantitative understanding of pure spin transport and spin Hall effect in a broad range of materials. *Journal of Applied Physics* **117**, 172603 (2015).

16 L. Zhu, D.C. Ralph & R.A. Buhrman. Enhancement of spin transparency by interfacial alloying. *Physical Review B* **99**, 180404 (2019).

17 M. Filianina, J.-P. Hanke, K. Lee, D.-S. Han, S. Jaiswal, A. Rajan, G. Jakob, Y. Mokrousov & M. Kläui. Electric-field control of spin-orbit torques in perpendicularly magnetized W/CoFeB/MgO films. *Physical Review Letters* **124**, 217701 (2020).

18 E. Liu, T. Fache, D. Cespedes-Berrocal, Z. Zhang, S. Petit-Watelot, S. Mangin, F. Xu & J.-C. Rojas-Sánchez. Strain-Enhanced Charge-to-Spin Conversion in Ta/Fe/Pt Multilayers Grown on Flexible Mica Substrate. *Physical Review Applied* **12**, 044074 (2019).

19 T. Nan, J.M. Hu, M. Dai, S. Emori, X. Wang, Z. Hu, A. Matyushov, L.Q. Chen & N. Sun. A Strain-Mediated Magnetoelectric-Spin-Torque Hybrid Structure. *Advanced Functional Materials* **29**, 1806371 (2019).

20 H. An, S. Haku, Y. Kanno, H. Nakayama, H. Maki, J. Shi & K. Ando. Manipulation of Spin-Torque Generation Using Ultrathin Au. *Physical Review Applied* **9**, 064016 (2018).

21 L. Zhu, L. Zhu, S. Shi, M. Sui, D. Ralph & R. Buhrman. Enhancing spin-orbit torque by strong interfacial scattering from ultrathin insertion layers. *Physical Review Applied* **11**, 061004 (2019).

22 L. Zhu & R. Buhrman. Maximizing Spin-Orbit-Torque Efficiency of Pt/Ti Multilayers: Trade-Off Between Intrinsic Spin Hall Conductivity and Carrier Lifetime. *Physical Review Applied* **12**, 051002 (2019).

23 A. Tulapurkar, Y. Suzuki, A. Fukushima, H. Kubota, H. Maehara, K. Tsunekawa, D. Djayaprawira, N. Watanabe & S. Yuasa. Spin-torque diode effect in magnetic tunnel junctions. *Nature* **438**, 339-342 (2005).

24 A. Iovan, S. Andersson, Y.G. Naidyuk, A. Vedyaev, B. Dieny & V. Korenivski. Spin diode based on Fe/MgO double tunnel junction. *Nano Letters* **8**, 805-809 (2008).

25 J.C. Sankey, Y.-T. Cui, J.Z. Sun, J.C. Slonczewski, R.A. Buhrman & D.C. Ralph. Measurement of the spin-transfer-torque vector in magnetic tunnel junctions. *Nature Physics* **4**, 67-71 (2008).

26 C. Wang, Y.-T. Cui, J. Sun, J. Katine, R. Buhrman & D. Ralph. Sensitivity of spin-torque diodes for frequency-tunable resonant microwave detection. *Journal of Applied Physics* **106**, 053905 (2009).

27 S. Miwa, S. Ishibashi, H. Tomita, T. Nozaki, E. Tamura, K. Ando, N. Mizuochi, T. Saruya, H. Kubota & K. Yakushiji. Highly sensitive nanoscale spin-torque diode. *Nature Materials* **13**, 50-56 (2014).

28 B. Fang, M. Carpentieri, X. Hao, H. Jiang, J.A. Katine, I.N. Krivorotov, B. Ocker, J. Langer, K.L. Wang & B. Zhang. Giant spin-torque diode sensitivity in the absence of bias magnetic field. *Nature Communications* **7**, 1-7 (2016).

29 P.N. Skirdkov & K.A. Zvezdin. Spin-Torque Diodes: From Fundamental Research to Applications. *Annalen der Physik* **532**, 1900460 (2020).

30 M. Frankowski, J. Chęciński, W. Skowroński & T. Stobiecki. Perpendicular magnetic anisotropy influence on voltage-driven spin-diode effect in magnetic tunnel junctions: A micromagnetic study. *Journal of Magnetism and Magnetic Materials* **429**, 11-15 (2017).

31 P. Dürrenfeld, A.A. Awad, A. Houshang, R.K. Dumas & J. Åkerman. A 20 nm spin Hall nano-oscillator. *Nanoscale* **9**, 1285-1291 (2017).

32 V.E. Demidov, S. Urazhdin, H. Ulrichs, V. Tiberkevich, A. Slavin, D. Baither, G. Schmitz & S.O. Demokritov. Magnetic nano-oscillator driven by pure spin current. *Nature Materials* **11**, 1028-1031 (2012).

33 R. Liu, W. Lim & S. Urazhdin. Spectral characteristics of the microwave emission by the spin Hall nano-oscillator. *Physical Review Letters* **110**, 147601 (2013).

34 M. Ranjbar, P. Drrenfeld, M. Haidar, E. Iacocca, M. Balinskiy, T. Le, M. Fazlali, A. Houshang, A. Awad & R. Dumas. CoFeB-based spin Hall nano-oscillators. *IEEE Magnetics Letters* **5**, 1-4 (2014).

35 Z. Duan, A. Smith, L. Yang, B. Youngblood, J. Lindner, V.E. Demidov, S.O. Demokritov & I.N. Krivorotov. Nanowire spin torque oscillator driven by spin orbit torques. *Nature Communications* **5**, 1-7 (2014).

List of Publications

1 **G.D.H. Wong**, C.C.I. Ang, W.L. Gan, W.C. Law, Z. Xu, F. Xu, C.S. Seet & W.S. Lew. Reversible strain-induced spin–orbit torque on flexible substrate. *Applied Physics Letters* **119**, 042402, doi:10.1063/5.0056995 (2021).

2 **G.D.H. Wong**, Z. Xu, W.L. Gan, C.C.I. Ang, W.C. Law, J. Tang, W. Zhang, P.K.J. Wong, X. Yu, F. Xu, A.T.S. Wee, C.S. Seet & W.S. Lew. Strain-Mediated Spin–Orbit Torque Enhancement in Pt/Co on Flexible Substrate. *ACS Nano*, doi:10.1021/acsnano.0c09404 (2021).

3 C.C.I. Ang, W.L. Gan, **G.D.H. Wong** & W.S. Lew. Temperature-modulated magnetic skyrmion phases and transformations analysis from first-order reversal curve study. *Physical Review B* **103**, 144409 (2021).

4 B. Coester, **G.D.H. Wong**, Z. Xu, J. Tang, W.L. Gan & W.S. Lew. Enhanced spin Hall conductivity in tungsten-copper alloys. *Journal of Magnetism and Magnetic Materials* **523**, 167545 (2021).

5 Z. Xu, **G.D.H. Wong**, J. Tang, E. Liu, W. Gan, F. Xu & W.S. Lew. Large spin Hall angle enhanced by nitrogen incorporation in Pt films. *Applied Physics Letters* **118**, 062406 (2021).

6 **G.D.H. Wong**, W.L. Law, F.N. Tan, W.L. Gan, C.C.I. Ang, Z. Xu, C. Seet & W.S. Lew. Thermal behavior of spin-current generation in Pt_xCu_{1-x} devices characterized through spin-torque ferromagnetic resonance. *Scientific Reports* **10**, 1-8 (2020).

7 Z. Xu, **G.D.H. Wong**, J. Tang, E. Liu, W.L. Gan, F. Xu & W.S. Lew. Giant Spin Hall Effect in Cu-Tb Alloy Thin Films. *ACS Applied Materials & Interfaces* (2020).

8 C.C.I. Ang, W.L. Gan, **G.D.H. Wong** & W.S. Lew. Electrical Control of Skyrmion Density via Skyrmion-Stripe Transformation. *Physical Review Applied* **14**, 054048 (2020).

9 F.N. Tan, W.L. Gan, C.C.I. Ang, **G.D.H. Wong**, H. Liu, F. Poh & W.S. Lew. High velocity domain wall propagation using voltage controlled magnetic anisotropy. *Scientific Reports* **9**, 1-6 (2019).

List of Conference Presentations

1. **G.D.H. Wong**, W.C. Law, F.N. Tan, J.D. Lim, Y. Otani, W.L. Gan, C.C.I. Ang, Z. Xu, C.S. Seet, W.S. Lew. "Thermal behavior of spin-current generation in Pt_xCu_{1-x} devices characterized through spin-torque ferromagnetic resonance". (Poster) *GlobalFoundries Technology Forum 2021, Singapore.*

2. **G.D.H. Wong**, W.C. Law, F.N. Tan, W.L. Gan, C.C.I. Ang, Z. Xu, C.S. Seet, W.S. Lew. "Thermal behavior of spin-current generation in Pt_xCu_{1-x} devices characterized through spin-torque ferromagnetic resonance". *IEEE Magnetic Symposium 2020, Singapore*.

3. F.N. Tan, **G.D.H. Wong**, H. Liu, F. Poh, W.S. Lew, "Electric Field Control on Single and Double Pt/Co Heterostructure for Enhanced Thermal Stability", (Poster) *GlobalFoundries Technology Forum 2019, Singapore*.

4. W.C. Law, T.L. Jin, **G.D.H. Wong**, G.K. Rajan, W.L. Gan, C.S. Seet, A. See, S.N. Piramanayagam, W.S. Lew. "Development strategy for pMTJ free layer with high thermal stability at operating temperatures" (Poster) *The 5th International Conference of Asian Union of Magnetics Societies (ICAUMS 2018). Jeju Island, South Korea*

5. F.N. Tan, **G.D.H. Wong**, Q.Y. Wong, W.S. Lew, "Electric Field Control on Single and Double Pt/Co Heterostructure for Enhanced Thermal Stability", *IEEE Magnetic Symposium 2018, Singapore.*